Comparative study of ρ^0, ω, $K^{*0}(890)$, and $\bar{K}^{*0}(890)$ production by charge-exchange reactions

A. B. Wicklund, D. S. Ayres, R. Diebold, A. F. Greene,* S. L. Kramer, and A. J. Pawlicki
Argonne National Laboratory, Argonne, Illinois 60439
(Received 25 August 1977)

We present cross sections and density-matrix elements from a high-statistics study of the reactions $\pi^- p \to \rho^0 n$, $K^- p \to \bar{K}^{*0}(890) n$, and $K^+ n \to K^{*0}(890) p$, at 3, 4, and 6 GeV/c and four-momentum transfer squared to the recoil nucleon $-t \leq 0.9$ GeV^2. The experiment was carried out at the Argonne Zero Gradient Synchrotron using the effective-mass spectrometer. In the same experiment, we have measured the ρ-ω interference cross sections by comparison of the two reactions $\pi^- p \to \pi^- \pi^+ n$ and $\pi^+ n \to \pi^+ \pi^- p$, to which the interference terms contribute with opposite signs. We examine the systematics of ρ^0 production: In the s channel we find little shrinkage with energy of the helicity-0 cross sections, which are presumably dominated by π exchange; the helicity-1 cross sections exhibit considerable shrinkage for unnatural-parity exchange, and antishrinkage for natural-parity exchange. The K^{*0} and $\bar{K}^{*0}$ production observables exhibit significant differences, especially in the helicity-1 states. These differences are due to interference between even- and odd-G-parity exchange amplitudes and they are related by SU(3) symmetry to ρ-ω interference effects and to the ρ^0 and ω production observables. It is shown that exchange-degeneracy-breaking effects satisfy SU(3) symmetry and can be explained qualitatively in the framework of SU(3)-symmetric, strongly absorbed Regge-pole models. The results of our amplitude analysis are compared with previous phenomenological analyses and model predictions.

I. INTRODUCTION

This paper describes a high-statistics comprehensive study of vector-meson production observed in the reactions

$$\pi^- p \to \pi^- \pi^+ n \quad (\rho^0 + \omega) , \tag{1.1}$$

$$\pi^+ n \to \pi^+ \pi^- p \quad (\rho^0 - \omega) , \tag{1.2}$$

$$K^- p \to K^- \pi^+ n \quad [\bar{K}^{*0}(890)] , \tag{1.3}$$

$$K^+ n \to K^+ \pi^- p \quad [K^{*0}(890)] . \tag{1.4}$$

Differential cross sections and decay angular distributions were measured for all four reactions at incident momenta of 3, 4, and 6 GeV/c in a single experiment with the Argonne effective-mass spectrometer (EMS). The combined data sample included 500 000 $\pi\pi$ events from reactions (1.1) and (1.2) and 45 000 $K\pi$ events from reactions (1.3) and (1.4).

Since the same apparatus was used for all four reactions, it was possible to minimize the systematic uncertainties involved in the comparison of the different processes. Charge symmetry constrains the observables for reactions (1.1) and (1.2) to be equal, except for ρ-ω interference effects associated with the electromagnetic decay $\omega \to \pi^+ \pi^-$, which contribute with opposite signs in the two reactions. Thus, comparison of the experimentally measured observables for reactions (1.1) and (1.2) provides a direct calibration of relative systematic errors both for these channels and for the topologically similar processes (1.3) and (1.4). With this calibration we can make an accurate comparison of the $K^{*0}(890)$ and $\bar{K}^{*0}(890)$ production channels and thereby study exchange-degeneracy (EXD)-violating mechanisms with good sensitivity. In addition, comparison of reactions (1.1) and (1.2) near the ω mass allows us to isolate the ρ-ω interference effects reliably. Some results from our ρ-ω interference study have been reported previously.[1]

High-statistics studies of dipion production in reaction (1.1) at 15 GeV/c (Ref. 2) and 17 GeV/c (Ref. 3) have led to a better understanding of the $\pi\pi$ interaction and of dipion production mechanisms, in particular absorbed one-pion exchange. The ρ-ω interference effects have also been extracted from the 17-GeV/c data by careful study of the dipion mass spectrum.[4] The data from the present experiment, together with the 15- and 17-GeV/c results, allow for the first time a detailed study of the energy dependence of dipion production and ρ-ω interference effects.

Although high-statistics data on $\bar{K}^{*0}$ production in reaction (1.3) have been reported at 13 GeV/c,[5] the available data do not isolate the EXD-violating differences between K^{*0} and $\bar{K}^{*0}$ production with any great precision. This is because most of the data on reactions (1.3) and (1.4) have come from different bubble-chamber experiments[6] performed at different energies and subject to different sys-

tematic biases. Indeed there appear to be serious normalization inconsistencies between some of these experiments.[7]

Our basic physics objective in this paper is to obtain a global picture of the $I=1$, $S=0$ exchange mechanisms responsible for vector-meson production. For completeness, such an analysis requires additional data on the reactions

$$\pi^- p \to \pi^- \pi^+ \pi^0 n \quad (\omega - \rho) , \tag{1.5}$$

$$\pi^+ n \to \pi^+ \pi^- \pi^0 p \quad (\omega + \rho) , \tag{1.6}$$

$$\pi^- p \to K^- K^+ n \quad (\phi) . \tag{1.7}$$

Fortunately adequate data are available on these channels in the 3- to 6-GeV/c momentum range. The ϕ- production observables in reaction (1.7) were measured in other EMS experiments as reported previously.[8] Consistent with the Okubo-Zweig-Iizuka rule, the ϕ-production amplitudes are so small that they can be safely neglected in the present analysis. High-quality ω-production data have been reported for reaction (1.5) at 6 GeV/c (Ref. 9) and for reaction (1.6) at 4 GeV/c.[10] Thus, with the inclusion of the data from the present experiment, a reasonably complete set of data on all of the reactions (1.1) to (1.7) is available in our energy region. Although precise data at high energies is essentially confined to the dipion and $\overline{K}^{*0}$ production channels, these data provide strong constraints on the energy dependence of the production amplitudes. We will explore this energy dependence in detail in the following analysis.

In principle the pion-induced reactions (1.1), (1.2), (1.5), and (1.6) determine not only the magnitude but also, via ρ-ω interference, the relative phases of the ρ and ω production amplitudes. These amplitudes can be most economically described using t-channel exchanges having definite G parity, for example π and A_2 or ρ and B exchanges. These same exchanges occur in the production of K^{*0} and $\overline{K}^{*0}$. Moreover, their relative couplings in all four processes

$$\pi^- p \to \rho^0 n \quad (\pi + A_2 \text{ exchange}) , \tag{1.8}$$

$$\pi^- p \to \omega n \quad (B + \rho \text{ exchange}) , \tag{1.9}$$

$$K^- p \to \overline{K}^{*0} n \quad (\pi + A_2 - B - \rho \text{ exchange}) , \tag{1.10}$$

$$K^+ n \to K^{*0} p \quad (\pi + A_2 + B + \rho \text{ exchange}) \tag{1.11}$$

are related by SU(3) symmetry.[11] Therefore, a major goal of our analysis is to test SU(3) symmetry for these reactions and in particular to investigate the relationship between EXD violation in the K^{*0}, $\overline{K}^{*0}$ channels and the interference phases measured in ρ^0 and ω production. For example, if the $G=\pm 1$ trajectories satisfied exact exchange degeneracy, then the cross sections for reactions (1.10) and (1.11) would be equal, and the ρ^0 and ω production amplitudes would be 90° out of phase with one another. By investigating the deviations from this simple situation, we can gain insight into the mechanisms by which EXD is broken, including evidence as to whether these mechanisms themselves satisfy SU(3). In order to carry out this investigation efficiently and to better explore the features of the vector-meson production amplitudes, we must rely heavily on model-dependent amplitude analysis.

Thus the aims of this paper are (1) to present new data on K^{*0}, $\overline{K}^{*0}$, and ρ^0 production from 3 to 6 GeV/c, (2) to present a final analysis of ρ-ω interference effects in the same energy range, (3) to explore the SU(3) relations between K^{*0}, $\overline{K}^{*0}$, and ρ and ω production, in particular to compare EXD breaking in K^{*0}-$\overline{K}^{*0}$ production with ρ-ω interference cross sections, and (4) to examine energy dependence in ρ^0 and K^{*0} production. These topics are organized as follows: In Sec. II we summarize the experimental techniques and analysis methods used to obtain these data. The analysis of the $\pi\pi$ and $K\pi$ mass spectra, needed to separate vector-meson production from nonresonant backgrounds, is described in Sec. III, together with a brief summary of the phenomenology of pion-exchange processes. In Sec. IV we examine the main features of the process $\pi^- p \to \rho^0 n$ from 3 to 17 GeV/c, and in Sec. V we present the results of our analysis of ρ-ω interference effects between 3 and 6 GeV/c. The features of ω, K^{*0}, and $\overline{K}^{*0}$ production are explored in Sec. VI, where the relationships between the vector-meson production reactions are examined in a phenomenological framework. Conclusions and summary are given in Sec. VII.

II. EXPERIMENTAL METHOD

The Argonne effective-mass spectrometer (EMS) has been described in previous publications.[12,13] For the sake of completeness we review here the aspects of data taking and analysis relevant to this experiment. The EMS was located in Beam 21 at the Argonne zero gradient synchrotron (ZGS); Fig. 1 shows a plan view of the apparatus with a two-prong event schematically superposed. Beam particles interacted in a 2-in. diameter, 20-in.-long liquid-hydrogen- or deuterium-filled target. Secondary charged particles traversed the spectrometer magnet; their trajectories were recorded by magnetostrictive-readout wire spark chambers surrounding the magnet volume. Recoil-particle trajectories were not measured, although some information was provided by a system of veto counters around the target and along the magnet pole faces. Event information was recorded on

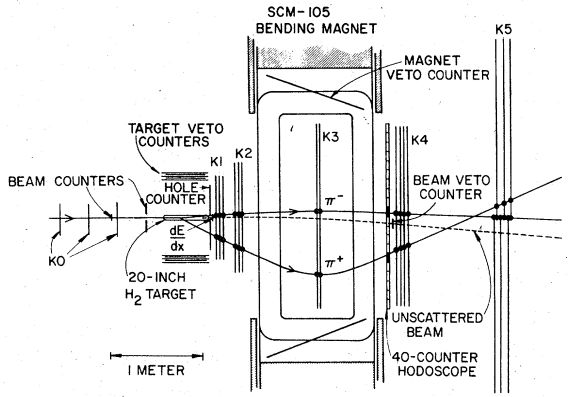

FIG. 1. Plan view of the effective-mass spectrometer. The SCM-105 spectrometer magnet provided 11.4 kG m of bending. $K0$ through $K5$ were sets of magnetostrictive-readout wire spark chambers; $K3$ had only vertical wires, which were read out outside the magnetic field, $K1$ and $K2$ had vertical and $\pm 30°$ diagonal wires, while other chamber sets had horizontal and vertical wires.

magnetic tape, and included coordinates from the 40 wire-spark-chamber readouts, the beam-particle momentum measured by the momentum hodoscope, Čerenkov-counter incident-particle identification, and tagging data from 60 scintillation counters used in the trigger logic. Identification of final states of interest depended on kinematic constraints, and no direct identification of the produced particles was made. Data with π and K beam particles were taken simultaneously; hydrogen and deuterium targets were used for both positive and negative beams. We now discuss more detailed aspects of the experiment and the analysis.

A. Beam

Particles in the unseparated beam were tagged by four threshold Čerenkov counters which provided a clean separation of π's, K's, p's, and $\bar{p}$'s; the "π" signature contained typically a 2% contamination of e's and μ's, which was measured separately. The momentum of each incident particle was measured to $\pm 0.2\%$ with a counter hodoscope at the first focus, and beam track directions were measured to ± 1 mrad with magnetostrictive-readout wire spark chambers. Typically 35% of the incident beam was rejected as "halo" by a series of beam-defining counters. Spark-chamber memory time limited the maximum total beam intensity to 3×10^5 particles in a 750-msec ZGS spill. Computer capability limited the data rate to 45 triggers per spill. Events with random beam tracks present during the spark-chamber sensitive time were tagged by the scintillation counter logic and rejected in subsequent analysis (~5 to 20% of the triggers). The beam flux was counted for each incident beam type, along with appropriate rate-dependent accidental coincidences (~2%); flux uncertainties were $\pm 2\%$ for each particle type.

B. Trigger logic and veto biases

The basic event trigger required the following:

(1) two or more counts in the 40-element scintillator hodoscope located immediately downstream of the spectrometer magnet;

(2) no signal from the $3''\times 3''$ beam veto counter located just downstream of the hodoscope; this eliminated triggers from noninteracting beam particles.

(3) a signal from the "hole" counter immediately following the target, signifying a large-angle scatter in the target, *or* a twice-minimum-ionizing signal from the "dE/dx" counter that covered the 2-in. square hole in the "hole" counter; this reduced unwanted triggers from beam particles interacting downstream of the target.

A system of veto counters was used to improve the trigger efficiency for the recoil-neutron reactions. Eight scintillation counters lining the upstream half of the magnet interior were used to veto forward ($\lesssim 45°$ production angle) charged tracks which struck the magnet poles or yoke. In addition, a box of scintillators interleaved with lead converter and Lucite δ-ray absorber surrounded the hydrogen target on four sides and vetoed wide-angle γ rays and charged particles. Altogether these "magnet" and "target" veto counters reduced the trigger rates by a factor of about 6; they also introduced a bias in the good event rate by vetoing recoil neutrons that happened to interact in the veto counters (~8%) or by detecting δ rays (~7%).

For reactions with recoil protons, these veto counters introduced significant biases for four-momentum transfers to the recoil of $-t > 0.2$ GeV^2; less energetic recoil protons generally ranged out before reaching any veto counters. For both recoil-proton and recoil-neutron reactions these biases were calibrated by taking substantial amounts of data with no magnet or target veto requirement in the trigger, but with the counters tagged for subsequent study. The target veto counters were used in hardware anticoincidence only for $\pi^\pm$ incident; for $K^\pm$-induced reactions the target veto counters were employed only in the analysis to select a clean data sample. The effects of each component of the veto system were studied with actual events and the results were used to construct a model that described the vetoing probability associated with recoil protons, neutrons, and δ rays.

This model was used to make appropriate corrections to the geometric efficiency for each sample of data; the corrections averaged ~15% for recoil-neutron reactions and 10 to 15% for $K^+n \to K^+\pi^-p$. The vetoing corrections for $\pi^+n \to \pi^+\pi^-p$ at large $-t$ ($-t > 0.3$ GeV^2) were as large as 50%, but the corrected cross sections and density-matrix elements agreed with those from the charge-symmetric reaction (1.1) within 5%. For the $K^\pm$-induced reactions, the relative uncertainties at large $-t$ due to veto corrections were conservatively taken to be ±7%.

Deuterium spectator protons ranged out before reaching any veto counters. This was established by the absence (<1%) of any signal from the reaction $\pi^+d \to \pi^+\pi^-pp_s$ in the vetoed event sample for $-t < 0.02$ GeV^2 (small $-t$ was chosen for this test to avoid confusion with recoil-proton vetoes).

With all vetoes in the trigger, the lowest trigger rate for π^- incident corresponded to an effective production cross section of 1.2 mb, of which about 7% were genuine $\pi^-p \to \pi^-\pi^+n$. Since $\pi^\pm$ triggers were abundant and since $K^\pm$ constituted only 1% of the incident beam, we were able to electronically enhance the $K^\pm$ flux by randomly suppressing 90% of the incident $\pi^\pm$ triggers. This resulted in an effective ratio of K to π flux of ≈1 : 10 while still giving the maximum data-taking rate allowed by the spark-chamber dead time and the computer system.

C. Event reconstruction and resolution

Event reconstruction was straightforward. Of the 40 spark-chamber planes, 38 were outside the magnetic-field volume where particle trajectories were straight lines. Because of high chamber efficiency and the redundancy of position information, losses due to spark chamber inefficiency were small; overall reconstruction losses were estimated by Monte Carlo and by beam-track measurements to be ~3% per track. Precise momentum analysis was made possible by detailed measurements of the spectrometer magnetic field.[14] The momentum calibration of both the spectrometer and beam-line dipole magnets was kept constant to ±0.1% through the use of nuclear magnetic resonance probes mounted on the magnet pole faces.

The relevant rms kinematic resolutions were essentially the same for $\pi^\pm$- and $K^\pm$-induced reactions and can be summarized as follows:

$$\sigma(\theta_x) \approx 0.4 + 1.5/p \ , \tag{2.1a}$$

$$\sigma(\theta_z) \approx 0.1 + 1.5/p \ , \tag{2.1b}$$

$$\sigma(p)/p \approx 0.004 + 0.001p \ , \tag{2.1c}$$

$$\sigma(m_{\pi\pi}) \approx 0.004 \text{ GeV} \ , \tag{2.1d}$$

$$\sigma[M_X(\mathrm{H}_2)] \approx [(0.002p_B)^2 + \sigma(p_-)^2 + \sigma(p_+)^2]^{1/2} \ , \tag{2.1e}$$

$$\sigma[M_X(\mathrm{D}_2)] \approx \{\sigma[M_X(\mathrm{H}_2)]^2 + 0.0016|t\ (\mathrm{GeV}^2)|\}^{1/2} \ . \tag{2.1f}$$

Here θ_x (θ_z) are production angles in mrad measured in the spectrometer, in the horizontal (vertical) plane, p, p_+, p_- are secondary charged-particle momenta in GeV/c, p_B is the incident beam momentum in GeV/c, $m_{\pi\pi}$ denotes the unfitted effective mass of a $\pi^+\pi^-$ pair at $m_{\pi\pi} = m_\rho$, M_X denotes the missing mass for $\pi^-p \to \pi^-\pi^+X$, where M_X ≈ nucleon mass. Typically $\sigma[M_x(\mathrm{H}_2)] = 0.020$, 0.028, and 0.040 GeV at 3, 4, and 6 GeV/c, respectively. The resolution on M_X was slightly worse with the deuterium target because of the unobserved spectator momentum, but the effect was not serious for momentum transfers accessible to this experiment ($-t \leq 1$ GeV^2). The $\pi\pi$ and $K\pi$ effective-mass calibration was checked by measuring the K_S^0 mass in the reaction $K^-p \to K_S^0(\to\pi^+\pi^-)n$. Extrapolating to larger-opening-angle pairs, we estimate the mass calibration uncertainty to be ±1.5 MeV in the $\rho^0(770)$ and $K^{*0}(890)$ mass regions.

A one-constraint fit was applied to events having missing mass close to the nucleon mass. This improved the resolution on secondary momenta and angles and in particular improved the effective-mass resolution somewhat. The fit also allowed an accurate reconstruction of the momentum and direction of the recoil nucleon which was essential for understanding the veto counter biases discussed above.

D. Event identification and backgrounds

The final states $\pi\pi N$ and $K\pi N$ were selected on the basis of the missing mass recoiling against the $\pi\pi$ and $K\pi$ systems. Figure 2 shows distributions for the quantity $M_X^2 - M_N^2$ (M_X = missing mass, M_N = nucleon mass) for K^-p and K^+n reactions for each beam momentum. As expected the M_X^2 resolutions are similar for K^- and K^+ incident at small momentum transfers [Figs. 2(a)–2(f)]. For larger momentum transfers ($0.2 < -t < 0.5$ GeV^2) the K^+n missing-mass distribution is somewhat broader than the K^-p because of the deuterium spectator motion [Figs. 2(g) and 2(h)]. Nevertheless, even at 6 GeV/c the missing-mass resolution (~±0.04 GeV) is good enough to separate nucleon-recoil events from the inelastic recoil reactions such as $KN \to K\pi\Delta$.

This is not to say that the M_X^2-selected events are free of background. Close to $K\pi$ threshold ($m_{K\pi} < 0.74$ GeV) there is a substantial tail of events having $M_X^2 < M_N^2$ which appears to violate energy conservation. These events occur only in $K^-p \to K^-\pi^+X$ [Fig. 2(i)] and not in $K^+n \to K^+\pi^-X$ [Fig.

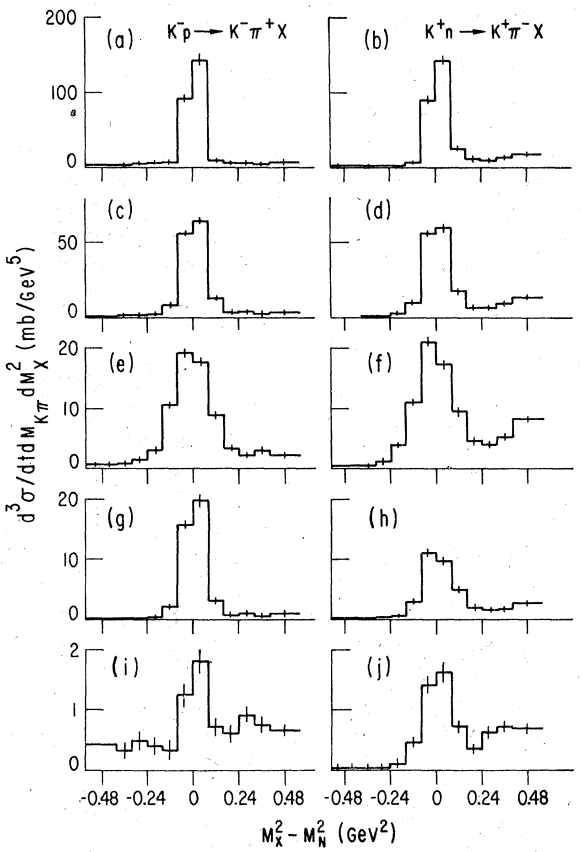

FIG. 2. Typical missing-mass distributions, $M_X^2 - M_N^2$, for $K^-p \to K^-\pi^+X$ (left-hand figures) and $K^+n \to K^+\pi^-X$ (right-hand figures), where M_N is the appropriate nucleon mass. Parts (a) through (f) are for $-t < 0.2$ GeV^2 and $0.84 \leq m_{K\pi} \leq 0.94$ GeV at 3 GeV/c [parts (a) and (b)], 4 GeV/c [parts (c) and (d)], and 6 GeV/c [parts (e) and (f)]. Parts (g) and (h) are for $0.2 \leq -t \leq 0.5$ GeV^2 and $0.84 \leq m_{K\pi} \leq 0.94$ GeV. Parts (i) and (j) are for $-t < 0.2$ GeV^2 at 4 GeV/c, with $m_{K\pi} < 0.74$ GeV (close to $K\pi$ threshold).

2(j)]. Moreover, if we select events with $M_X^2 < 0.64$ GeV^2, there is no $K^*(890)$ signal in the $K^-\pi^+$ mass spectrum; the low-M_X^2 tail is produced with roughly the same cross section in the $K^*(890)$ region [Fig. 2(c)] as near $K\pi$ threshold [Fig. 2(i)]. The most likely explanation for these events is that the positive track seen in the spectrometer was a slow proton rather than a π^+, and that the events come from the reaction $K^-p \to K^-p(X^0)$, where X^0 denotes a neutral meson system not seen by the target and magnet veto counters. This reaction can proceed by, among other mechanisms, the diffractive process $K^-p \to K^-N^*$, where a slow proton from the N^* breakup is observed in the spectrometer. For K^+ incident the analogous background would come from $K^+n \to p\pi^-(X^+)$, which cannot proceed diffractively. Thus the diffractive contribution may account for the bulk of the $K^-p \to K^-p(X^0)$ background, and the lack of a diffractive contribution may account for the absence of background of the type $K^+n \to p\pi^-(X^+)$.

Similar backgrounds with $M_X^2 < M_N^2$ are seen in dipion production with $\pi^\pm$ incident, again because slow protons that traverse the spectrometer are misidentified as π^+'s. The resulting contamination in the selected events clearly depends on the decay angles of the $\pi\pi$ and $K\pi$ systems; contamination is largest for asymmetric decays that result in a slow positive π^+ or K^+ track in the spectrometer. To correct for this contamination we have measured the $\pi\pi$ and $K\pi$ angular distribution coefficients as functions of not only momentum transfer and effective mass, but also M_X^2. From the M_X^2 dependence (presence or absence of low-M_X^2 tails), we have estimated the background correction for each density-matrix element as a function of $m_{\pi\pi}$ ($m_{K\pi}$) and t.

Specifically, we have fitted the M_X^2 distributions with three components: (1) a Gaussian signal to describe the missing nucleon, (2) phase space to describe final states of the type $\pi\pi\Delta$, $K\pi\Delta$, and (3) linear or quadratic functions of M_X^2 to describe misidentified proton events. Near $\pi\pi$ and $K\pi$ thresholds the latter contamination is substantial as shown above. In the mass regions of interest ($m_{\pi\pi} > 0.65$ GeV, $m_{K\pi} > 0.80$ GeV) the corrections were found to be small, however, and the missing-mass cuts resulted in ~2% contamination from $\pi\pi\Delta$ and $K\pi\Delta$ final states, with ~2% loss of $\pi\pi N$ and $K\pi N$ events. The corrections for misidentified protons were significant only for the (s-channel) helicity-0 cross sections, where they averaged 5% for π^-p, 10% for π^-d, 2% for π^+d, 3% for K^-p, 6% for K^-d, and 0% for K^+d.

Production of K^0's and Λ's constituted another kind of background which was trivially removed by kinematic cuts. Events were rejected if the two tracks measured in the spectrometer could have come from a K_S^0 (±12 MeV) or a Λ (±6 MeV) decay. The same cuts were applied in the acceptance calculation.

One remaining source of background is the reaction $\pi^\pm N \to K^+K^-N$, which populates the region $M_X^2 > M_N^2 + \epsilon$; the separation $\epsilon \approx 0.3$ GeV^2 for 4-GeV/c incident and $\epsilon \approx 0.15$ GeV^2 for 6-GeV/c incident. For incident K^-, the analogous background reaction $K^-N \to K^+K^-(\Lambda, \Sigma \ldots)$ lies well above our M_X^2 cuts and can be ignored. The K^+K^-N final state is important only for symmetric decay configurations. Figure 3 shows the M_X^2 distributions for the reaction $\pi^-p \to \pi^-\pi^+X$, where we have projected out the helicity-1 density-matrix element $\rho_{11} - \rho_{1-1}$. Close to $\pi\pi$ threshold [Figs. 3(a) and

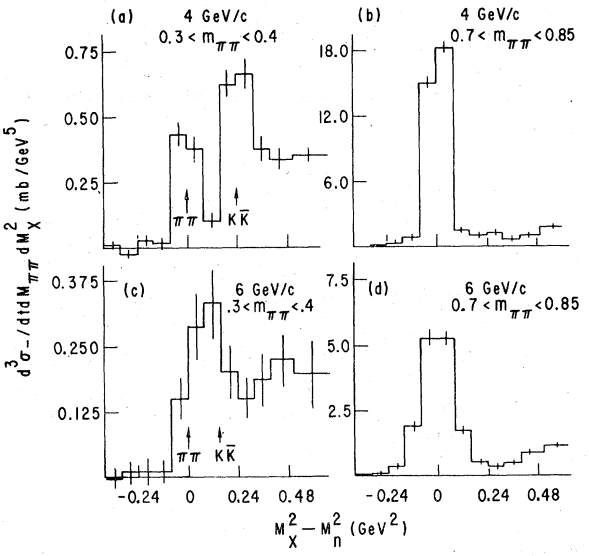

FIG. 3. Missing-mass distributions, $M_X^2 - M_n^2$, for the ρ_{11}-ρ_{1-1} projected cross section for $\pi^- p \to \pi^+ \pi^- X$. The incident momenta and $\pi\pi$ effective-mass ranges (in GeV) are given in the figure. The signal from $\pi^- p \to K^+ K^- N$ contamination is clearly evident in the low-effective-mass data.

3(c)] there is clear evidence for a K^+K^-N signal; in the ρ^0 region [Figs. 3(b) and 3(d)] the K^+K^-N signal appears to be negligible. We have not added an explicit K^+K^-N contamination to the M_X^2 fits described above. Instead we have lumped the K^+K^-N contamination in with the misidentified proton contribution in the M_X^2 fits, allowing a quadratic parametrization for the combined effect. This procedure is certainly adequate for the region of interest in this paper, $m_{\pi\pi} > 0.64$ GeV, where the possible K^+K^-N contamination is known to be small.[15]

E. Spectrometer-acceptance corrections

The central problem in the analysis is to correct the data for spectrometer acceptance in order to extract physical cross sections and density-matrix elements. The following factors determine the acceptance:

(1) Geometric acceptance: The secondary particles were required to pass through geometric apertures which were defined in software to be slightly smaller than the physical apertures present in the spectrometer. In addition, a momentum cutoff, $p > 0.28$ GeV/c, was imposed and track angles with respect to the beam line were required to be less than 45°, both upstream and downstream of the spectrometer magnet.

(2) The two tracks had to strike different hodoscope counters in order to satisfy the trigger. The resulting overall inefficiency was around 3%, but depended rather critically on the kinematic variables.

(3) Both tracks had to miss the beam veto counter. This gave an overall inefficiency of about 3%, which again depended critically on the two-particle decay configuration.

The inefficiencies associated with items (1) to (3) above are "geometrical" in the following sense. With an unpolarized target the physical cross sections are independent of the production azimuth (azimuthal orientation of the production plane about the beam direction). Once we have specified the kinematic variables for the $\pi\pi N$ or $K\pi N$ final state (the effective mass $m_{\pi\pi}$ or $m_{K\pi}$, the four-momentum transfer t to the recoil nucleon, and the decay angles, θ and ϕ, referred to the s- or t-channel reference frames[16]) and also the production vertex coordinates, the efficiency is either 0 or 100% depending on the production azimuth. In other words, the efficiency can be defined by specifying a discrete set of production azimuths $\Psi_1, \bar{\Psi}_1, \Psi_2, \bar{\Psi}_2, \ldots, \Psi_N, \bar{\Psi}_N$ such that each interval $\Psi_i < \Psi < \bar{\Psi}_i$ defines an allowed region, where all events can be accepted by the apparatus. In the data analysis, each event was required to be within the regions of azimuth allowed for its m, t, θ, and ϕ values; the same regions were used to calculate analytically the geometric acceptance for any choice of kinematic variables.

Additional factors reduced the efficiency within each geometrically allowed ψ interval. These were:

(4) Attenuation of the incident beam and secondary particles due to interactions in the target (~7% in H_2, ~15% in D_2) and in the spectrometer materials (~5%).

(5) Decays in flight of the incident beam kaons (~3%) and of secondary π's and K's. The latter losses depended on beam momentum and $\pi\pi$ ($K\pi$) decay angles; typical decay-in-flight corrections averaged ~3% for $\pi^\pm$ incident and ~20% for $K^\pm$ incident at 4 GeV/c.

(6) Vetoing of recoil nucleons by the target and magnet veto counters, as discussed above in Sec. II B. These corrections depended strongly on the production azimuth ψ because of the geometry of the veto counters. In turn, because the geometrically allowed ψ regions depended on the $\pi\pi$ and $K\pi$ kinematics, the veto corrections were quite different for the different density-matrix elements.

The acceptance at each point in phase space was defined analytically by integrating the corrections (4) through (6) over the allowed ψ intervals; an additional integration was required over the vertex location in the 20-in.-long hydrogen target. A maximum-likelihood technique[17] was then used to

deduce acceptance-corrected angular distribution coefficients from the data, after binning the data in the variables $m_{\pi\pi}$ ($m_{K\pi}$), t, and $M_X{}^2$. The fits were done separately in both s- and t-channel frames. The equations needed can be summarized as follows. We express the physical angular distribution in a single mass and t bin by the expansion in terms of spherical harmonics,

$$\frac{d^2\sigma(m,t)}{d\cos\theta d\phi}=\frac{1}{\sqrt{4\pi}}\sum_{l,m}t_{lm}\mathrm{Re}[Y_l^m(\theta,\phi)] \ . \qquad (2.2)$$

The coefficients t_{lm} are to be determined. We define starting values $\hat{t}_{lm}$ that give a good approximation to the angular distributions (i.e., by previous trial and error); these $\hat{t}_{lm}$ define a first-guess angular distribution:

$$\hat{\sigma}(m,t,\theta,\phi)=\frac{1}{\sqrt{4\pi}}\sum_{l,m}\hat{t}_{lm}\mathrm{Re}[Y_l^m(\theta,\phi)] \ . \qquad (2.3)$$

We sum over the N events in the bin to obtain the arrays

$$R_{lm}=\frac{1}{\sqrt{4\pi}}\sum_{i=1}^{N}\frac{\mathrm{Re}[Y_l^m(\theta_i,\phi_i)]}{\hat{\sigma}(m_i,t_i,\theta_i,\phi_i)} \ . \qquad (2.4)$$

We integrate numerically over the efficiency $E(m,t,\theta,\phi)$ to form the following arrays:

$$\epsilon_{lm}=\frac{1}{\sqrt{4\pi}}\int\int E(m,t,\theta,\phi)\mathrm{Re}[Y_l^m(\theta,\phi)]d\cos\theta\, d\phi \qquad (2.5)$$

and

$$V_{lm}^{l'm'}=\frac{1}{4\pi}\int\int\frac{E(m,t,\theta,\phi)\mathrm{Re}[Y_l^m(\theta,\phi)]\mathrm{Re}[Y_{l'}^{m'}(\theta,\phi)]d\cos\theta\, d\phi}{\hat{\sigma}(m,t,\theta,\phi)} \ . \qquad (2.6)$$

Then we can solve for the desired angular coefficients

$$t_{lm}-\hat{t}_{lm}=\frac{1}{f}\sum_{l'm'}[V^{-1}]_{lm}^{l'm'}(R_{l'm'}-f\epsilon_{l'm'}) \ , \qquad (2.7)$$

where f is the incident beam flux (expressed in events/mb) and V is understood to be a two-dimensional matrix with indices specified by the list (l,m). The matrix V^{-1}/f is now the error matrix for the t_{lm}'s.

This procedure differs from the conventional maximum-likelihood technique in that the matrix "V" has been determined by numerical integration rather than by a summation over events (only the array R_{lm} is obtained from events). Monte Carlo studies showed that this numerical evaluation of V in fact leads to far more satisfactory results in terms of convergence and reliability. Of course, there are a variety of fitting procedures which are equivalent to our maximum-likelihood technique in the sense that they give unbiased estimates of the parameters. For example, a least-squares fit, binning the data in θ and ϕ, leads to the same equations as our technique in the limit of infinitely small bins. As another example, the "method of moments," employed in Ref. 3, is equivalent to our technique with the substitution of an isotropic distribution for $\hat{\sigma}(m,t,\theta,\phi)$ (i.e., $\hat{t}_{00}=1$; $\hat{t}_{lm}=0$ otherwise). If the physical distributions deviate from isotropy, then this method in principle gives larger statistical errors because the events are not optimally weighted; however, the incorrect choice of $\hat{\sigma}$ does not bias the answers. Our procedure was tested with Monte Carlo events and was shown to converge in one or two iterations (i.e., further

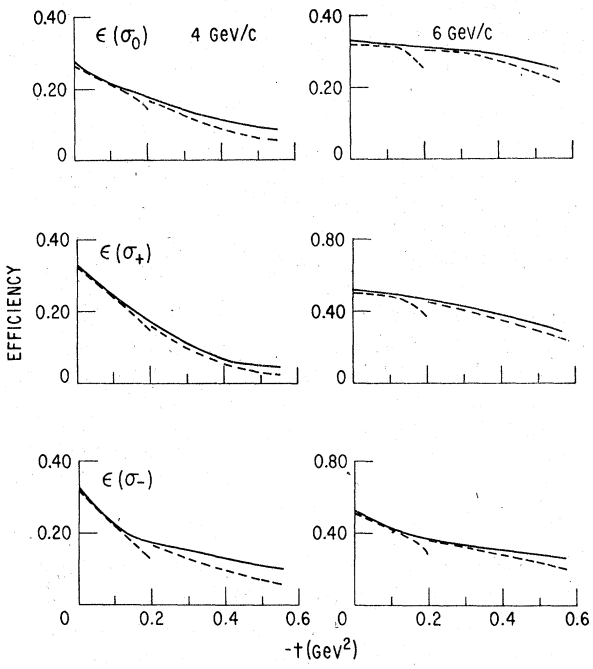

FIG. 4. Spectrometer efficiency ϵ_{lm} [defined by Eq. (2.5)] for $K^*(890)$ production as a function of momentum transfer t, integrated over the decay angles θ and ϕ in the s-channel helicity frame. The acceptance for 4 GeV/c is shown in the left-hand figures, and for 6 GeV/c in the right-hand figures. The efficiencies $\epsilon(\sigma_0)$, $\epsilon(\sigma_+)$, and $\epsilon(\sigma_-)$ give the acceptance for the final-state configurations described by the pure density-matrix elements ρ_{00}, $\rho_{11}+\rho_{1-1}$, and $\rho_{11}-\rho_{1-1}$, respectively. The solid curves show the efficiency for the K^-p reaction and the dashed curves for the K^+n reaction, where target and magnet veto counter biases can be important.

iterations with refined estimates of $\hat{\sigma}$ did not change the answers significantly). In our fits, $\hat{\sigma}$ was always parametrized in such a way as to ensure positive cross sections for all θ and ϕ.

For illustration Fig. 4 shows some of the efficiency integrals defined by Eq. (2.5) for $K^*(890)$ production; these are for the linear combinations of the spherical harmonics Y_0^0, Y_2^0, and $\mathrm{Re}Y_2^2$ which give the density-matrix elements ρ_{00}("σ_0"), $\rho_{11}+\rho_{1-1}$("σ_+"), and $\rho_{11}-\rho_{1-1}$("σ_-"). The efficiencies are rather similar for the three density-matrix elements, and there are only modest differences between efficiencies for initial states K^+n and K^-p. The breaks in the K^+n efficiency at $-t=0.2$ GeV^2 arise because of the use of the target veto counters; these were employed in software veto for small $-t$ to simplify the event selection, whereas for $-t>0.2$ GeV^2 only the magnet vetoes were used for K^+n events. For K^-p the target and magnet veto requirements were imposed in software for all t. Note that at larger $-t$ the efficiencies improve dramatically in going from 4 to 6 GeV/c.

Acceptance integrals as illustrated in Fig. 4 are the relevant quantities for unfolding the physical distributions. Figure 5 offers a more detailed look at efficiencies for $\pi\pi$ and $K\pi$ final states plotted as functions of the helicity-frame decay angles θ_H and ϕ_H. The efficiencies vanish near $\cos\theta_H=+1$ ($\pi\pi$ and $K\pi$) and $\cos\theta_H=-1$ ($\pi\pi$) because of the 280 MeV/c lower momentum cutoff. Most of the wiggles seen in Fig. 5 are caused by the beam veto counter and the trigger hodoscope constraints. Despite their complexity, the efficiency curves do not vanish over large angular domains, and it is straightforward to unfold the angular distributions which are encountered in vector-meson production.

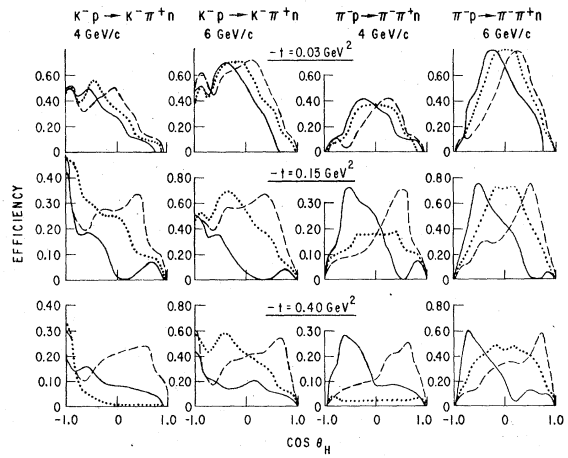

FIG. 5. Spectrometer efficiencies for the reactions, incident momenta, and t values shown, as functions of the decay angles θ and ϕ in s-channel helicity frame. The efficiencies shown are for $m_{\pi\pi}=0.770$ GeV and $m_{K\pi}=0.890$ GeV. The acceptance for $\phi=0°$ is shown by the dashed curves, for $\phi=90°$ by the dotted curves, and for $\phi=180°$ by the solid curves.

F. Deuterium corrections

In addition to correcting for the experimental differences between hydrogen and deuterium target reactions, we must also take into account the reduction of the deuterium cross sections both by Glauber screening and by the Pauli exclusion principle at small $-t$.[18] We found the screening effect to be consistent with zero empirically, although 5% might have been expected; we have therefore made no correction for screening. The exclusion principle relates deuteron (d) to free-nucleon (N) cross sections by

$$\frac{d\sigma}{dt}(d)=\frac{d\sigma}{dt}(N)\left[1-\frac{S(-t)}{3}\right]. \tag{2.8}$$

We have parametrized the deuteron form factor from electron scattering data[19] as

$$S(-t)\approx e^{43t+110t^2}\quad(-t<0.2\ \mathrm{GeV}^2)\,. \tag{2.9}$$

The correction in Eq. (2.8), with the factor of $\frac{1}{3}$, is valid for nucleon spin-flip amplitudes. Fortunately this is the only relevant correction for $\pi\pi$ and $K\pi$ production because (1) all unnatural-parity-exchange amplitudes are spin flip[20] due to parity conservation, and (2) the natural-parity-exchange density matrix projection, $\rho_{11}+\rho_{1-1}$, is pure spin flip near $t=0$ because of angular momentum conservation.

The corrections that are in principle different for hydrogen and deuterium data include (1) screening and exclusion principle effects, (2) attenuation in the target, (3) background subtractions, and (4) veto biases which depend on the charge of the recoil nucleon. We have measured the effects (1), (2), and (3) by comparing the negative-incident-beam reactions, $K^-p\to K^-\pi^+n$ with $K^-d\to K^-\pi^+nn_s$ and $\pi^-p\to\pi^-\pi^+n$ with $\pi^-d\to\pi^-\pi^+nn_s$. The corrected angular distributions were consistent and the normalizations agreed to better than ±5% in the K^* and ρ regions. We have combined K^-p and K^-d events for the physics analysis but have made no further use of the π^-d data. In addition, comparison of the charge-symmetric reactions $\pi^-p\to\pi^-\pi^+n$ and $\pi^+d\to\pi^+\pi^-pp_s$ (away from the ρ-ω interference region, 775 to 795 MeV) checks all four deuterium corrections and serves as a calibration for the K^-p and K^+d reactions (which are not related by charge symmetry). Figure 6 shows the ratio of differential cross sections in the ρ region plotted against t at 4 GeV/c. Integrated over the ρ mass (excluding the ρ-ω inter-

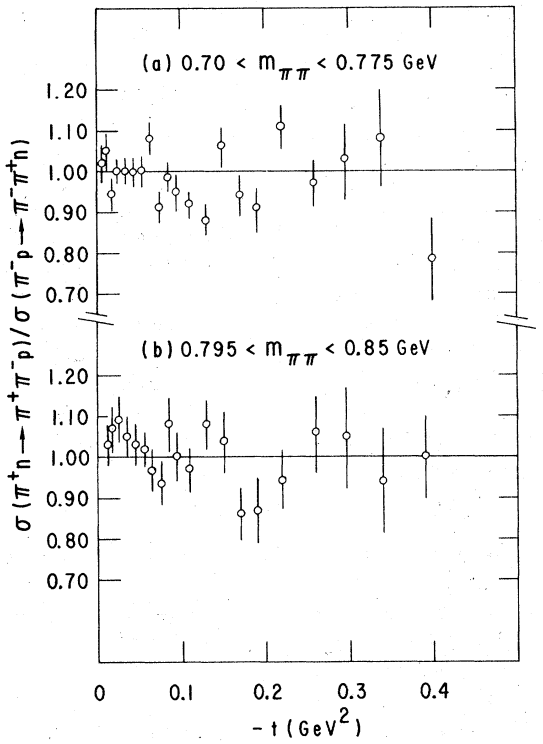

FIG. 6. The ratio of π^+n and π^-p differential cross sections for $\pi^+\pi^-N$ production as a function of t after correction for deuterium effects, at 4 GeV/c. The ρ-ω interference region, $0.775 < m_{\pi\pi} < 0.795$ GeV, has been excluded from this comparison.

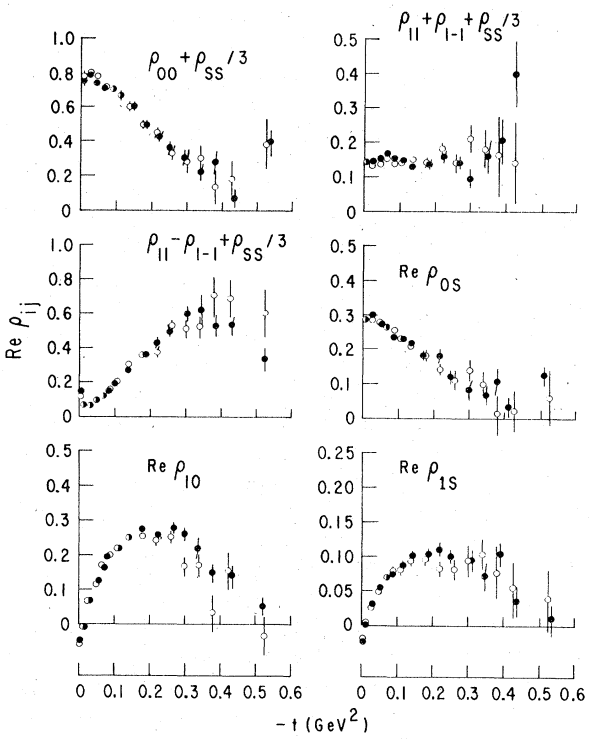

FIG. 7. Comparison of the six density-matrix elements in the s-channel helicity frame for $\pi^-p \to \pi^+\pi^-n$ (solid points) and $\pi^+n \to \pi^-\pi^+p$ (open points), after correction for deuterium effects. The mass range used was $0.70 \leq m_{\pi\pi} \leq 0.85$ GeV, excluding the ρ-ω interference region.

ference region), the cross sections for reactions (1.1) and (1.2) at 4 GeV/c agree to within ±2% for $-t < 0.4$ GeV^2. In Fig. 7 the six density-matrix elements for the S- and P-wave contributions are compared for the initial states π^-p and π^+d. From a comparison of integrated projections, $\rho_{ij}d\sigma/dt$, we find empirically that systematic differences between hydrogen- and deuterium-target observables in reactions (1.1) and (1.2) are less than ±6% for $-t < 0.4$ GeV^2.

G. Systematic uncertainties

We expect the following systematic uncertainties in the differences between K^-p and K^+d reaction cross sections in the $K^*(890)$ region: (1) relative flux errors are ±2%, (2) uncertainties in background corrections are ±3%, (3) recoil veto biases are ±3 to ±7%, depending on t, and (4) deuterium corrections are ±3%. From these we would expect relative uncertainties of ±6% for $-t < 0.25$ GeV^2 and ±9% at larger $-t$. Since many of the systematic uncertainties are independent of whether a $K\pi$ or $\pi\pi$ system is produced, an alternate method of estimating the relative $K\pi$ errors would be to use the agreement found for the $\pi\pi$ results for the two beam polarities. The level of confidence from this method is about the same as given above. The physics differences between K^-p and K^+n reactions turn out to be generally larger than these uncertainties, as we shall show below.

The uncertainty in absolute normalization contains additional contributions from spectrometer acceptance (±2%), reconstruction program inefficiency (±4%), and incident-beam-kaon decays (±3%). Thus the total systematic uncertainty in our quoted cross sections is ±6% for $\pi^-p \to \rho^0n$, ±8% for $K^-p \to \bar{K}^*n$, and ±8% for $K^+n \to K^*p$ with $-t < 0.25$ GeV^2 (±11% with $-t > 0.25$ GeV^2). No corrections have been made for radiative effects.[21] Such systematic effects will be, to first order, common to the K^-p and K^+d reactions.

III. MASS-SPECTRUM FITS

Our data consist of corrected angular distribution coefficients for reactions (1.1), (1.2), (1.3), and (1.4) which have been determined as functions of $\pi\pi$ and $K\pi$ mass in coarse t bins, and as functions of t in coarse mass bins. Our main objective

is to obtain pure P-wave vector-meson-production observables as functions of t. However, the mass dependence of the observables gives important information on (1) the nature of the S wave, D wave, or other "backgrounds" that accompany the P wave, (2) explicit mass dependence associated with absorptive or off-shell effects, and (3) ρ-ω interference parameters. In this section we examine the first two issues and give parametrizations for the mass spectra in terms of the elastic $\pi\pi$ and $K\pi$ phase shifts; ρ-ω interference is discussed in Sec. V. The phase-shift parametrization of this section will be used in conjunction with the t-dependent fits of Sec. IV to perform the separation of the S-, P-, and D-wave contributions.

We start by expressing the angular distribution in the ρ and K^* regions in terms of the usual density-matrix expansion:

$$p_{\rm lab}{}^2\,\frac{d^4\sigma}{dmdtd\cos\theta d\phi}=\frac{1}{4\pi}\,p_{\rm lab}{}^2\,\frac{d^2\sigma}{dmdt}\left[\left(\rho_{00}+\frac{\rho_{SS}}{3}\right)3\cos^2\theta+\left(\rho_{+}+\frac{\rho_{SS}}{3}\right)3\sin^2\theta\cos^2\phi+\left(\rho_{-}+\frac{\rho_{SS}}{3}\right)3\sin^2\theta\sin^2\phi\right.$$
$$-(\mathrm{Re}\rho_{10})6\sqrt{2}\,\sin\theta\cos\theta\cos\phi+(\mathrm{Re}\rho_{0S})2\sqrt{3}\,\cos\theta-(\mathrm{Re}\rho_{1S})2\sqrt{6}\,\sin\theta\cos\phi$$
$$\left.+\sum_{m=0}^{2}t_{3m}\sqrt{4\pi}\,\mathrm{Re}Y_3^m(\theta,\phi)\right]. \qquad (3.1)$$

The decay angles θ and ϕ are given in either the s- or t-channel helicity frames; m and t denote the $\pi\pi$ or $K\pi$ effective mass and the four-momentum transfer to the recoil nucleon, respectively. The density-matrix elements (dme's) ρ_{00}, ρ_{+}, ρ_{-}, and ρ_{10} describe P-wave production; ρ_{0S} and ρ_{1S} measure S-P interference and ρ_{SS} gives the S-wave intensity. The D waves are expected to be very small in the mass regions of interest and so we have truncated the expansion of Eq. (3.1) with Y_3^m terms, which measure P-D interference. For convenience we have defined the helicity-1 combinations

$$\rho_{+}=\rho_{11}+\rho_{1-1}, \qquad (3.2a)$$

and

$$\rho_{-}=\rho_{11}-\rho_{1-1}. \qquad (3.2b)$$

Asymptotically ρ_{+} and ρ_{-} project out natural- and unnatural-parity exchanges, respectively. We have scaled the cross sections by the flux factor $p_{\rm lab}{}^2$ to better expose the energy dependence of the dynamical amplitudes.[22]

Our principal objective is to extract the pure P-wave dme's ρ_{00}, ρ_{+}, ρ_{-} and $\mathrm{Re}\rho_{10}$ by subtracting the S-wave background, ρ_{SS}, together with D-wave interference contributions. The simplest technique would be to fit the $\pi\pi$ and $K\pi$ mass spectra to sums of P-wave Breit-Wigner forms and background polynomials. This procedure suffers from the inherent arbitrariness involved in defining background polynomials and also from the difficulty of determining subsequently the t dependence of ρ_{SS} with limited statistics. A more highly constrained, but model-dependent approach is to obtain independent information on the S wave from the S-P interference terms ρ_{0S} and ρ_{1S} in order to predict ρ_{SS}. We will show that this procedure describes the background as well as would a polynomial and that it allows us to determine the t dependence of ρ_{SS} from the measured quantity ρ_{0S}.

In the remainder of this section we attack the problem of separating S, P, and D waves as follows: (1) We establish a general formalism to describe the observables, which we will then use throughout this article. (2) We summarize the essential predictions of absorption models for π-exchange amplitudes. (3) From these models we abstract assumptions which are sufficient to accomplish the desired partial-wave separation. (4) We summarize the results of the fits to the data, extracting at the same time some physics conclusions on vector-meson production from the mass dependence of the observables.

A. Partial-wave-amplitude expansion

In order to parametrize the exchange-model description of vector-meson production, we first expand the observables in Eq. (3.1) in terms of production amplitudes which correspond to states of definite $\pi\pi$ or $K\pi$ orbital angular momentum L and helicity M. We use linear combinations of the $M=\pm1$ amplitudes $\tilde{L}_M$:

$$\tilde{L}_{\pm}=(\tilde{L}_{+1}\pm\tilde{L}_{-1})/\sqrt{2}\,, \qquad (3.3)$$

where $\tilde{L}_{+}$ and $\tilde{L}_{-}$ asymptotically project out natural- and unnatural-parity exchanges, respectively. For simplicity, the notation $\tilde{S}\equiv\tilde{S}_0$ is used throughout. Dropping small terms which contain $M=2$ D wave or are quadratic in $M\leq1$ D-wave amplitudes, we obtain the expansions

$$p_{\rm lab}{}^2\left(\rho_{00}+\frac{1}{3}\rho_{SS}\right)\frac{d^2\sigma}{dmdt}=|\tilde{P}_0|^2+\tfrac{1}{3}|\tilde{S}|^2$$
$$+\tfrac{2}{3}\sqrt{5}\,\mathrm{Re}(\tilde{D}_0^*\tilde{S}), \qquad (3.4a)$$

$$p_{\rm lab}^2\left(\rho_{\pm}+\frac{1}{3}\rho_{ss}\right)\frac{d^2\sigma}{dmdt}=|\tilde{P}_{\pm}|^2+\tfrac{1}{3}|\tilde{S}|^2 - \tfrac{1}{3}\sqrt{5}\ \mathrm{Re}(\tilde{D}_0^*\tilde{S}), \quad (3.4b)$$

$$p_{\rm lab}^2\,\mathrm{Re}\rho_{10}\frac{d^2\sigma}{dmdt}=\frac{1}{\sqrt{2}}\ \mathrm{Re}[\tilde{P}_-^*\tilde{P}_0+(\tfrac{5}{3})^{1/2}\tilde{D}_-^*\tilde{S}], \quad (3.4c)$$

$$p_{\rm lab}^2\,\mathrm{Re}\rho_{0s}\frac{d^2\sigma}{dmdt}=\mathrm{Re}\left[\tilde{P}_0^*\tilde{S}+\frac{2}{\sqrt{5}}\tilde{D}_0^*\tilde{P}_0 + (\tfrac{3}{5})^{1/2}(\tilde{D}_-^*\tilde{P}_-+\tilde{D}_+^*\tilde{P}_+)\right], \quad (3.4d)$$

$$p_{\rm lab}^2\,\mathrm{Re}\rho_{1s}\frac{d^2\sigma}{dmdt}=\frac{1}{\sqrt{2}}\ \mathrm{Re}\left[\tilde{P}_-^*\tilde{S}-\frac{1}{\sqrt{5}}\tilde{D}_0^*\tilde{P}_- + (\tfrac{3}{5})^{1/2}\tilde{D}_-^*\tilde{P}_0\right], \quad (3.4e)$$

$$p_{\rm lab}^2 t_{30}\frac{d^2\sigma}{dmdt}=\frac{6}{\sqrt{35}}\ \mathrm{Re}(\sqrt{3}\,\tilde{D}_0^*\tilde{P}_0-\tilde{D}_-^*\tilde{P}_--\tilde{D}_+^*\tilde{P}_+), \quad (3.4f)$$

$$p_{\rm lab}^2 t_{31}\frac{d^2\sigma}{dmdt}=\frac{1}{\sqrt{35}}\ \mathrm{Re}(8\sqrt{3}\,\tilde{D}_-^*\tilde{P}_0+12\tilde{D}_0^*\tilde{P}_-), \quad (3.4g)$$

$$p_{\rm lab}^2 t_{32}\frac{d^2\sigma}{dmdt}=2(\tfrac{6}{7})^{1/2}\mathrm{Re}(\tilde{D}_-^*\tilde{P}_--\tilde{D}_+^*\tilde{P}_+). \quad (3.4h)$$

For simplicity the sums over nucleon-flip and nucleon-nonflip amplitudes are not shown explicitly in Eq. (3.4). Instead, the amplitudes $\tilde{L}_M$ are used to represent the full helicity amplitudes $\tilde{L}^M_{\lambda\lambda'}$, where λ and λ' refer to the recoil- and target-nucleon helicities, respectively. The notation of Eq. (3.4) thus implies incoherent sums over the flip and nonflip contributions:

$$|\tilde{L}_M|^2=|\tilde{L}^M_{++}|^2+|\tilde{L}^M_{+-}|^2, \quad (3.5a)$$

$$\mathrm{Re}(\tilde{L}_M^*\tilde{L}_{M'})=\mathrm{Re}(\tilde{L}^{M*}_{++}\tilde{L}^{M'}_{++}+\tilde{L}^{M*}_{+-}\tilde{L}^{M'}_{+-}). \quad (3.5b)$$

In practice, it should be a good first approximation to ignore nucleon helicities, since the π-exchange contributions to $\tilde{L}_0$ and $\tilde{L}_-$ are expected to be highly spin coherent. In the following discussion we will exhibit the nucleon-helicity structure only when necessary for clarity.

In principle the amplitudes $\tilde{L}_M$ can be arbitrary functions of m and t. In practice it is useful to factorize each $\tilde{L}_M$ into a product of a "production" amplitude which depends mainly on t and a "decay" amplitude which depends mainly on mass. It was first pointed out by Schlein[23] that this factorizability property holds for conventional particle-exchange models even in the presence of absorption. Thus we can write

$$\tilde{L}_M(m,t)=L_M(m,t)f_L(m)/N. \quad (3.6)$$

The "decay" amplitudes $f_L(m)$ are defined explicitly in Table I; they contain the $\pi\pi$ ($K\pi$) elastic amplitudes $(2L+1)^{1/2}\sin\delta e^{i\delta}$ and also isospin and phase-space ($m/\sqrt{q}$) factors. Possible off-shell corrections to the $\pi\pi$ ($K\pi$) scattering amplitudes, which depend on both m and t,[24] can be lumped into the "production" amplitudes $L_M(m,t)$. Additional m dependence in $L_M(m,t)$ can also arise from absorptive corrections.

The factor N in Eq. (3.6) is introduced to simplify the normalization of the production amplitudes; we choose

$$N^2=f_I\int_0^\infty |f_P(m)|^2dm \quad [\text{where } f_I(\pi\pi)=1,\ f_I(K\pi)=\tfrac{3}{2}], \quad (3.7)$$

thus fixing the vector-meson production cross sections to be

$$p_{\rm lab}^2\frac{d\sigma}{dt}(\rho,K^*,\bar{K}^*)\approx|P_0|^2+|P_+|^2+|P_-|^2. \quad (3.8)$$

With this normalization the production amplitudes, P_M, are corrected for the K^* decay branching ratio, while the amplitudes $\tilde{P}_M$ give the cross sections for the observed final states $K^\pm\pi^\mp$. Equation (3.8) is a good approximation because experimentally $P_M(m,t)$ varies much more slowly with m than does $f_P(m)$.

It will be useful for subsequent discussion to clarify the relationships between s- and t-channel production amplitudes. The crossing is accomplished by two independent orthogonal transformations, one acting on the meson and the other on the nucleon-helicity indices; these transformations are different for the natural- and unnatural-parity exchange amplitudes. Consider first the unnatural-parity S- and P-wave production amplitudes. At the meson vertex we obtain

$$S(s\text{ chan})=S(t\text{ chan}) \quad (3.9a)$$

$$\begin{pmatrix}P_0\\P_-\end{pmatrix}_{s\text{ chan}}=\begin{pmatrix}\cos\chi & -\sin\chi\\ \sin\chi & \cos\chi\end{pmatrix}\begin{pmatrix}P_0\\P_-\end{pmatrix}_{t\text{ chan}}. \quad (3.9b)$$

The crossing angle χ, which is the angle between the z axes in the s-channel and t-channel frames, is approximately given by

$$\sin\chi\approx 2m(-t')^{1/2}/(m^2-t'), \quad (3.10a)$$

$$\cos\chi\approx(m^2+t')/(m^2-t'), \quad (3.10b)$$

where $t'=t-t_{\rm min}$. For example, at $-t=0.1\ \mathrm{GeV}^2$, $\chi=45°$; at $0.5\ \mathrm{GeV}^2$ this becomes 90°.

The crossing relations at the nucleon vertex are[25]

TABLE I. Parametrization of the $\pi\pi$ and $K\pi$ elastic scattering amplitudes. Notation: $m=\pi\pi$ or $K\pi$ effective mass, m_R=resonance mass, q=center-of-mass momentum of the π in the $\pi\pi(K\pi)$ rest frame, q_R=value of q at $m=m_R$, $\Gamma(m)=\Gamma_R(q/q_R)^3[1+(q_R R_P)^2]/[1+(qR_P)^2]$. The quantities m_R, Γ_R, R_S, R_P, and a_S^0 are parameters in the fits; the D-wave phase shift δ_D^0 and the $I=\frac{3}{2}$ and $I=2$ phase-shift parameters are fixed (see Ref. 40).

(a) The elastic L-wave decay amplitudes $f_L(m)$

$$f_S(\pi\pi)=(\tfrac{2}{3}\sin\delta_S^0 e^{i\delta_S^0}+\tfrac{1}{3}\sin\delta_S{}^2 e^{i\delta_S{}^2})m/\sqrt{q}$$

$$f_P(\pi\pi)=\sqrt{3}\,(\sin\delta_P{}^1 e^{i\delta_P{}^1})m/\sqrt{q}$$

$$f_D(\pi\pi)=\sqrt{5}\,(\tfrac{2}{3}\sin\delta_D^0 e^{i\delta_D^0})m/\sqrt{q}$$

$$f_S(K\pi)=(\tfrac{2}{3}\sin\delta_S{}^{1/2} e^{i\delta_S{}^{1/2}}+\tfrac{1}{3}\sin\delta_S{}^{3/2} e^{i\delta_S{}^{3/2}})m/\sqrt{q}$$

$$f_P(K\pi)=\sqrt{3}\,(\tfrac{2}{3}\sin\delta_P{}^{1/2} e^{i\delta_P{}^{1/2}})m/\sqrt{q}$$

$$f_D(K\pi)=0$$

(b) The phase shifts δ_L^I (L=orbital angular momentum, I=isospin)

$$\delta_S{}^{1/2} \text{ and } \delta_S^0=\tan^{-1}[q/(1/a_S^0+R_S q^2/2)]$$

$$\delta_S{}^{3/2} \text{ and } \delta_S{}^2=\tan^{-1}(qa_S{}^2)$$

$$\delta_P{}^{1/2} \text{ and } \delta_P{}^1=\tan^{-1}[m_R\Gamma(m)/(m_R{}^2-m^2]$$

$$\delta_D^0=\sin^{-1}[0.0629m^5/(1.6-m^2)], \text{ e.g., } \delta_D^0=6^\circ \text{ at } m_{\pi\pi}=1 \text{ GeV}$$

$$a_S{}^2=-0.85 \text{ GeV}^{-1}, \quad a_S{}^{3/2}=-0.60 \text{ GeV}^{-1}$$

$$\begin{pmatrix} L_{++}^{0,-} \\ L_{+-}^{0,-} \end{pmatrix}_{s \text{ chan}} = \begin{pmatrix} \cos\theta & -\sin\theta \\ \sin\theta & \cos\theta \end{pmatrix} \begin{pmatrix} L_{++}^{0,-} \\ L_{+-}^{0,-} \end{pmatrix}_{t \text{ chan}} , \tag{3.11}$$

where

$$\cos\theta \approx (t_{\min}/t)^{1/2} \tag{3.12a}$$

and

$$\sin\theta \approx (t'/t)^{1/2} . \tag{3.12b}$$

Note that at high energies $t_{\min}/t$ is small, and $\sin\theta \approx 1$; thus, the crossing at the nucleon vertex is essentially antidiagonal for unnatural-parity-exchange amplitudes. CP invariance requires that the unnatural-parity Regge poles couple to definite t-channel $N\bar{N}$ helicity states. For example π and B ($CP=-1$) exchanges must be nucleon-helicity nonflip in the t channel, while A_1-type exchanges ($CP=+1$) must be helicity flip. Because of the antidiagonal nature of the crossing relations, π and B exchanges are mainly helicity flip in the s channel, while A_1 exchange is nonflip. This fact has important consequences for absorption models since absorptive corrections are expected to depend strongly on s-channel helicity structure.[26] The transformation given by Eq. (3.11) also affects the interpretation of $P_0 P_-$ interference terms when $t_{\min}/t$ is not small, as will be shown in Sec. IV.

The natural-parity-exchange amplitude P_+ is invariant at the meson vertex:

$$P_+(s \text{ chan}) = P_+(t \text{ chan}) . \tag{3.13}$$

Thus the spin-averaged observable $|P_+|^2$ is the same in both s and t channels. Since there are no interference terms between P_+ and $P_{0,-}$, there is no need to specify in detail the crossing relations for P_+ at the nucleon vertex. It is sufficient to note that the transformations are essentially diagonal in the nucleon-helicity indices at small $-t$.

B. Lessons from absorption models

In order to obtain useful constraints on the separation of S, P, and D waves, it is convenient to review the basic features of the production amplitudes, $L_M(m,t)$, in the framework of absorbed π-exchange descriptions. In Born approximation, π exchange couples only to the t-channel amplitude L_{++}^0.[25] The crossing relations given by Eqs. (3.9) to (3.13) imply the following structure for the s-channel Born amplitudes at high energies, in the limit $t_{\min}=0$:

$$S_{+-}(m,t) = F_S(m,t)\frac{\sqrt{-t}}{\mu^2 - t}\,, \tag{3.14a}$$

$$P^0_{+-}(m,t) = F_P(m,t)\frac{\sqrt{-t}}{\mu^2 - t}\cos\chi(m,t)\,, \tag{3.14b}$$

$$P^-_{+-}(m,t) = F_P(m,t)\frac{\sqrt{-t}}{\mu^2 - t}\sin\chi(m,t)\,, \tag{3.14c}$$

$$P^+_{+-}(m,t) = 0\,, \tag{3.14d}$$

$$L^M_{++}(m,t) = 0\,, \tag{3.14e}$$

where μ = the pion mass and the $F_L(m,t)$ include form factors and off-shell corrections to the $\pi\pi$ or $K\pi$ scattering amplitudes. Note that all of the Born terms vanish at $t=0$. This is a general consequence of factorizability of residues in both elementary and Reggeized π exchange.[27] The dipion production data at 15 GeV/c^2 and 17 GeV/c^3 are incompatible with the above structure in three respects: (1) P_+ does not vanish; (2) P_- does not appear to vanish as $t \to 0$; and (3) the ratio $|S|/|P_0|$, as derived from the ratio $\mathrm{Re}\rho_{0S}/\rho_{00}$, appears to be nearly constant in t, whereas in Born approximation this ratio should increase with t due to the rapidly varying $\cos\chi$ factor in Eq. (3.14b).

The simplest absorption recipe that remedies these defects and gives a reasonable description of the high-energy data at small $-t$ is the Williams model.[28,29] In this model three physical mechanisms completely determine the t dependence, namely the pion propagator, angular momentum conservation, and absorption. Absorption is incorporated with two corrections to the Born amplitudes: (1) A common exponential collimating factor is applied to all amplitudes L_M; (2) all functions of t are evaluated at $t=\mu^2$, except for the propagator and those factors $(-t)^n$ that are required by angular momentum conservation. Here n is the net s-channel helicity flip given by

$$n = |M - \lambda + \lambda'| \tag{3.15}$$

for amplitudes $L^M_{\lambda\lambda'}$. From the definition, Eq. (3.3), $P^{\pm}_{+,-}$ are superpositions of $n=0$ and $n=2$ double-flip amplitudes:

$$P^-_{+-}(m,t) = [P^{+1}_{+-}(n=0) - P^{-1}_{+-}(n=2)]/\sqrt{2}\,, \tag{3.16a}$$

$$P^+_{+-}(m,t) = [P^{+1}_{+-}(n=0) + P^{-1}_{+-}(n=2)]/\sqrt{2}\,. \tag{3.16b}$$

The Born amplitude P^+_{+-} vanishes because the $n=0$ and $n=2$ π-exchange contributions cancel in Eq. (3.16b). However, in the Williams model (WM) these contributions have different t dependences, and do not cancel. At high energies the WM s-channel amplitudes take the form

$$S_{+-}(m,t) = F(t)\frac{\sqrt{-t}}{\mu^2 - t}\,, \tag{3.17a}$$

$$P^0_{+-}(m,t) = F(t)\frac{\sqrt{-t}}{\mu^2 - t}\cos\chi(t=\mu^2)\,, \tag{3.17b}$$

$$P^-_{+-}(m,t) \approx \frac{-F(t)}{m}\,\frac{\mu^2 + t}{\mu^2 - t}\,, \tag{3.17c}$$

$$P^+_{+-}(m,t) \approx \frac{-F(t)}{m}\,, \tag{3.17d}$$

$$L^M_{++}(m,t) = 0\,, \tag{3.17e}$$

where $F(t)$ includes the exponential collimation due to absorption and where we have used Eq. (3.10a) to approximate $\sin\chi \approx 2\sqrt{-t}/m$.

In order to better expose the effects of absorption, we can decompose the WM amplitudes into contributions from the Born terms and absorptive cuts. The most dramatic effects occur in the amplitudes $P^{\pm}_{+-}$ at small $-t$, which have the form

$$P^-_{+-}(m,t) \approx \frac{-2tF(t)}{m(\mu^2 - t)} - C(m,t)\,, \tag{3.18a}$$

$$P^+_{+-}(m,t) \approx -C(m,t)\,, \tag{3.18b}$$

where $C(m,t) = F(t)/m$. The Born term contributes only to P^-_{+-}, while the cut $C(m,t)$ in the $n=0$ amplitude contributes equally to P^+_{+-} and P^-_{+-}, and does not have to vanish at $t=0$.

Thus the effects of absorption in the WM are (1) the presence of a large nonfactorizing cut, $C(m,t)$, in the $n=0$ amplitude, and (2) additional exponential collimation of equal strength in the $n=0$, 1, and 2 amplitudes. The cut $C(m,t)$ induces a zero in $P^-_{+-}(m,t)$ at $t=-\mu^2$, as shown in Eq. (3.17c). It is a general feature of absorption models that the $n=0$ amplitudes are more strongly absorbed than the $n=1,2$ amplitudes. This is because the $n=0$ terms are more central in impact-parameter space; the helicity amplitudes behave like b^n for small impact distances b.

For subsequent applications, it is convenient to note that the WM amplitudes take on a particularly simple form in the t-channel frame:

$$S_{++}(m,t) = F(t)\sqrt{-t}/(\mu^2 - t)\,, \tag{3.19a}$$

$$P^0_{++}(m,t) \approx F(t)\sqrt{-t}/(\mu^2 - t)\,, \tag{3.19b}$$

$$P^-_{++}(m,t) \approx -C(m,t)\,, \tag{3.19c}$$

$$P^+_{+-}(m,t) \approx -C(m,t)\,, \tag{3.19d}$$

where

$$C(m,t) = F(t)/m\,. \tag{3.19e}$$

Although the WM appears to describe the high-energy dipion data fairly well, a number of modifications suggested by more sophisticated absorption models may be necessary. First, there is no provision for zeros at larger $-t$ in the $n=1,2$ amplitudes; these could be introduced by means of a more complicated $F(t)$ factor. In general, as dis-

cussed by Kimel and Reya,[30] the small $-t$ collimation can vary with n, requiring different factors $F_n(t)$ in Eq. (3.17). Second, there is evidence that the cut contribution, $C(m,t)$ in Eq. (3.18), falls off faster than $1/m$ with increasing dipion mass.[31] Third, nontrivial phases should be present both in the Born terms due to the Regge signature factor and in the absorptive cuts as emphasized by Kane and Seidl.[32] The analysis of ρ^0 production by Estabrooks and Martin[33] indicates a high degree of phase coherence, but phase differences of $\sim 15°$ between P_0 and P_- are not ruled out.[34] Finally, other exchanges besides the π are likely to play some role, especially those exchanges that can interfere with the π-exchange WM amplitudes in ρ and K^* production; these include ρ and A_2 in P^+_{+-} and B in $P^{0,-}_{+-}$. The neglect of A_1-type exchanges in L^M_{++} is only a simplifying assumption based on the fact that these contributions cannot interfere with the WM amplitudes. Recent polarization measurements on reaction (1.1) at 17 GeV/c (Ref. 35) suggest that $|P^{0,-}_{++}|^2$ accounts for at least $\sim 3\%$ of the ρ^0 production cross section.

We have discussed the WM in some detail because many authors, including Estabrooks and Martin,[33] Froggatt and Morgan,[36] Kimel and Reya,[30] and Irving and Michael[37] have used modified versions of the WM description for phenomenological amplitude analyses. We will use the WM parametrization throughout this article in the same spirit, not as a theory to be tested, but as a first-order phenomenological description and as a basis for discussion. The refinements listed above can be incorporated as the data require.

C. Model-dependent separation of the partial-wave amplitudes

One method of obtaining pure P-wave production observables is to first solve Eqs. (3.4) directly for the amplitudes $\tilde{L}_M$ as functions of m and t. The vector-meson cross sections and dme's can then be reconstructed and averaged over mass using the amplitudes $\tilde{P}_M$. In addition, the phase-shift parameters can be extracted from the $\tilde{L}_M$ by using the factorization assumption, Eq. (3.6), in conjunction with a model that specifies the production amplitudes L_M. This is in essence the procedure pioneered by Estabrooks and Martin.[33] In order to solve Eqs. (3.4) it is first necessary to reduce the number of independent amplitudes. Estabrooks and Martin accomplished this for reaction (1.1) by specifying the nucleon-helicity structure of the $\tilde{L}^M_{\lambda\lambda'}$, to be dominantly s-channel helicity flip as suggested by absorbed π exchange; A_1-type exchange contributions were assumed to be small and hence ignorable in the observables of Eq. (3.4), where they appear quadratically.

One difficulty with the Estabrooks-Martin technique is that the data must be binned very finely in both m and t since the amplitudes $\tilde{L}_M(m,t)$, unlike $L_M(m,t)$ or $f_L(m)$ in Eq. (3.6), depend strongly on both kinematic variables; this requires very high statistics. A second problem, which is not unique to their approach, is the existence of discrete ambiguities in the solutions for $\tilde{S}$ and $\tilde{P}$. These can be resolved with further physical requirements, namely that $\tilde{S}(m,t)$ be continuous and that, for reaction (1.1), the resulting $\pi\pi$ S-wave phase shifts correspond to the broad ϵ solution favored by Protopopescu *et al.*[38] from their analysis of the $S^*(980)$ effect.

For our purposes, we can regard the Estabrooks-Martin analysis as having established the fact that a fairly simple amplitude structure is consistent with the main features of the 17-GeV/c dipion production data. In particular, the amplitudes $\tilde{L}_M$ are compatible with the factorization assumption, Eq. (3.6); the $f_L(m)$ are consistent with broad S-wave and resonant P-wave $\pi\pi$ phase shifts, provided that the production amplitudes $L_M(m,t)$ vary only slowly with m and exhibit the structures anticipated by absorbed π-exchange models.

Accordingly, we adopt an iterative procedure which examines the m and t dependence separately. From the beginning we impose the constraint that the $\pi\pi$ and $K\pi$ phase shifts should be continuous and allow no narrow S-wave resonances under the ρ or K^*; this is implicit in our parametrization of $f_L(m)$ (see Table I). We first determine the parameters that describe $f_L(m)$ using some simplifying assumptions about the structure of the production amplitudes $L_M(m,t)$. Subsequently in Sec. IV, we fix $f_L(m)$ using the parametrization of this section, and extract the t dependence of $L_M(m,t)$ from the data.

The simplifying assumptions which we apply to the production amplitudes are based largely on the apparent success of the WM in describing small $-t$ data and on the conclusions from the Estabrooks-Martin analysis. They are as follows:

(1) S and P_0 are spin coherent and have the same production phase, resulting in the constraint

$$\mathrm{Re}(P_0^* S) = (|P_0|^2 |S|^2)^{1/2}. \tag{3.20}$$

(2) S and P_0 have no explicit mass dependence, so that the helicity-0 amplitudes take the simple form

$$\tilde{S}(m,t) = S(t) f_S(m)/N, \tag{3.21a}$$

$$\tilde{P}_0(m,t) = P_0(t) f_P(m)/N. \tag{3.21b}$$

Thus the mass dependence of the helicity-0 observables determines the S- and P-wave phase shifts.

(3) $P_\pm$ are allowed some explicit mass depen-

dence, which we parametrize by

$$|P_\pm|^2 \propto [1 + a_\pm(m_R - m)/m], \tag{3.22}$$

where m_R denotes the ρ or K^* mass. The Williams model predicts $a_\pm \approx 2$, but as noted above the 17-GeV/c dipion data seem to require a stronger mass dependence.

(4) Assumptions (1) and (2) cannot be simultaneously valid in both s- and t-channel frames unless P_- is also phase coherent with P_0, since P_- and P_0 mix under crossing. Empirically we obtain essentially the same S- and P-wave phase shifts whether we fit the mass spectra in the s or t channels, indicating that $P_- - P_0$ phase differences must be fairly small. Our parametrization allows P_- to have a (small) t-dependent phase relative to P_0; the most sensitive way of detecting this phase is by comparison of the mass dependence of the S-P interference terms ρ_{0s} and ρ_{1s}, as discussed below. For the mass-spectrum fits, our parametrization does not require spin coherence between P_- and P_0 or P_- and S.

(5) Finally, we dispose of the small D-wave contributions to the production observables by invoking the Williams-model prescription[33]

$$\tilde{D}_0(m,t) \approx \tilde{P}_0(m,t)[f_D(m)/f_P(m)], \tag{3.23a}$$

$$\tilde{D}_\pm(m,t) \approx \sqrt{3}\,\tilde{P}_\pm(m,t)[f_D(m)/f_P(m)]. \tag{3.23b}$$

Thus all of the D-wave terms in Eq. (3.4) can be replaced by corresponding expressions involving only S and P amplitudes modified by the correction factor $f_D(m)/f_P(m)$. The $\pi\pi$ D-wave phase shift given in Table I corresponds to the tail of the $f(1270)$, normalized to 6° at $m_{\pi\pi} = 1$ GeV. This phase is consistent with our poorly determined t_{3m} moments, and somewhat smaller than the low-mass D wave from the 17-GeV/c phase-shift analysis.[39] The vector-meson production observables are empirically insensitive to these small D-wave contributions, although the S-wave phase shift does depend slightly on the choice of D wave. Consistent with the absence of significant t_{3m} moments in the $K\pi$ data, we have ignored $K\pi$ D-wave corrections altogether.

D. Results of the mass-spectrum fits

Using the assumptions discussed above, we arrive at the parametrization for the mass dependence of the observables given in Table II. For each t interval the mass spectra for the six dme's depend on eight intensity parameters defined in Table II: $\tilde{\sigma}_0$, $\tilde{\sigma}_+$, $\tilde{\sigma}_-$, $\mathrm{Re}\tilde{\sigma}_{10}$ (pure P wave), $\tilde{\sigma}_{ss}$ (pure S wave), $\tilde{\sigma}_{0s}$, $\mathrm{Re}\tilde{\sigma}_{1s}$, and $\mathrm{Im}\tilde{\sigma}_{1s}$ (S-P interference). The parameters $\tilde{\sigma}_0$, $\tilde{\sigma}_{ss}$, and $\tilde{\sigma}_{0s}$ are related by Eq. (3.20), $\tilde{\sigma}_{0s} = (\tilde{\sigma}_0\tilde{\sigma}_{ss})^{1/2}$. The explicit mass dependence of $P_\pm(m,t)$ is expressed by the parameters a_+, a_-, and a_{10}. For simplicity, Table II does not show the small D-wave corrections which were actually used in fitting the mass spectra. The D wave and also the $I = \frac{3}{2}$ and $I = 2$ phase shifts were fixed in the fits,[40] while the five S- and P-wave parameters a_S, R_S, m_R, Γ_R, and R_P (see Table I) were fitted in broad t intervals, at each energy, in both s and t channels.

TABLE II. Parametrization used to fit the $\pi\pi$ and $K\pi$ mass dependence of the six independent S-wave and P-wave observables. The eight intensity parameters $\tilde{\sigma}_i$ and the three production-amplitude mass-dependence coefficients a_i are parameters in the fits. The L-wave decay amplitudes $f_L(m)$ are defined in Table I. The small D-wave corrections used in the fits are not shown.

$$p_{\mathrm{lab}}{}^2\left(\rho_{00} + \frac{\rho_{SS}}{3}\right)\frac{d\sigma}{dm} = \tilde{\sigma}_0|f_P(m)|^2 + \frac{\tilde{\sigma}_{SS}|f_S(m)|^2}{3}$$

$$p_{\mathrm{lab}}{}^2\left(\rho_{+} + \frac{\rho_{SS}}{3}\right)\frac{d\sigma}{dm} = \tilde{\sigma}_+|f_P(m)|^2\left[1 + a_+\frac{(m_R - m)}{m}\right] + \frac{\tilde{\sigma}_{SS}|f_S(m)|^2}{3}$$

$$p_{\mathrm{lab}}{}^2\left(\rho_{-} + \frac{\rho_{SS}}{3}\right)\frac{d\sigma}{dm} = \tilde{\sigma}_-|f_P(m)|^2\left[1 + a_-\frac{(m_R - m)}{m}\right] + \frac{\tilde{\sigma}_{SS}|f_S(m)|^2}{3}$$

$$p_{\mathrm{lab}}{}^2\,\mathrm{Re}(\rho_{0S})\frac{d\sigma}{dm} = \tilde{\sigma}_{0S}\,\mathrm{Re}[f_S^*(m)f_P(m)], \text{ where } \tilde{\sigma}_{0S} = (\tilde{\sigma}_0\tilde{\sigma}_{SS})^{1/2}$$

$$p_{\mathrm{lab}}{}^2\,\mathrm{Re}(\rho_{10})\frac{d\sigma}{dm} = \frac{1}{\sqrt{2}}\,\mathrm{Re}(\tilde{\sigma}_{10})|f_P(m)|^2\left[1 + a_{10}\frac{(m_R - m)}{m}\right]$$

$$p_{\mathrm{lab}}{}^2\,\mathrm{Re}(\rho_{1S})\frac{d\sigma}{dm} = \frac{1}{\sqrt{2}}\{\mathrm{Re}(\tilde{\sigma}_{1S})\,\mathrm{Re}[f_S^*(m)f_P(m)] - \mathrm{Im}(\tilde{\sigma}_{1S})\,\mathrm{Im}[f_S^*(m)f_P(m)]\}\left[1 + a_{10}\frac{(m_R - m)}{m}\right]$$

TABLE III. Results of the $\pi\pi$ mass-spectrum fits in the interval $0.64 < m_{\pi\pi} < 0.94$ GeV. The parameters are defined in Tables I and II, and their values are an average of the results obtained from $\pi^- p \to \pi^-\pi^+ n$ and $\pi^+ n \to \pi^+\pi^- p$ data. The ρ-ω interference region, $0.77 < m_{\pi\pi} < 0.80$ GeV, has been excluded from the fits; the errors shown are from the $\pi^- p$ fits. The values of δ_S^0 are calculated from the fitted values of the phase-shift parameters for $m_{\pi\pi} = 775$ MeV. Results are given for fits in both the s- and t-channel helicity frames. The absolute mass-scale uncertainty is estimated to be ±1.5 MeV.

p_{lab} (GeV/c)	Frame	$-t$ range (GeV^2)	m_R (MeV)	Γ_R (MeV)	R_P (GeV^{-1})	a_S^0 (GeV^{-1})	R_S (GeV^{-1})	δ_S^0 (deg)	a_-	a_+	a_{10}
3	s	0–0.08	762±1	144±4	5.9±1.3	3.0±0.2	−4.4±0.2	83	0.5±0.7	1.5±0.6	−0.4±0.6
4	s	0–0.08	766±1	145±3	4.5±0.4	2.5±0.1	−4.3±0.1	72	1.4±0.6	2.9±0.4	−1.1±0.4
6	s	0–0.08	765±1	138±3	4.9±0.6	2.6±0.1	−4.3±0.1	74	0.7±0.9	2.1±0.5	−1.4±0.5
3	t	0–0.08	765±1	142±4	5.6±1.0	3.1±0.2	−4.2±0.2	82	3.1±0.6	2.5±0.7	2.6±0.4
4	t	0–0.08	768±1	153±3	4.6±0.4	2.4±0.1	−4.3±0.1	68	4.0±0.5	3.2±0.5	2.3±0.2
6	t	0–0.08	767±1	143±3	4.2±0.4	2.3±0.1	−4.3±0.1	67	4.0±0.5	3.1±0.5	2.1±0.2
3	s	0.08–0.2	764±2	160±5	4.2±0.8	2.9±0.2	−4.4±0.2	81	−0.1±0.5	0.6±0.8	−0.1±0.4
4	s	0.08–0.2	770±1	144±3	4.3±0.5	2.7±0.2	−4.3±0.1	77	0.2±0.3	1.7±0.5	0.3±0.3
6	s	0.08–0.2	768±2	148±4	4.5±0.6	2.5±0.2	−4.3±0.1	73	0.1±0.4	1.2±0.5	0.1±0.3
3	t	0.08–0.2	769±2	166±6	3.8±0.7	2.6±0.2	−4.2±0.3	74	3.0±0.6	0.7±0.8	2.3±0.5
4	t	0.08–0.2	774±1	152±4	4.0±0.6	2.6±0.2	−4.3±0.1	72	2.6±0.5	1.9±0.5	2.1±0.3
6	t	0.08–0.2	769±1	154±4	4.1±0.6	2.2±0.2	−4.3±0.1	65	3.8±0.6	1.9±0.6	1.8±0.3

Representative numerical values of the fitted phase-shift parameters, together with $a_\pm$ and a_{10} are given in Table III for $\pi\pi$ and in Table IV for $K\pi$. The $\pi\pi$ parameters represent an average of the results for π^+ and π^- incident; this eliminates ρ-ω interference effects. We remark that the fits were done iteratively, first fixing R_S and R_P at reasonable values, then varying R_S and R_P with all other parameters fixed. Thus the errors in Tables III and IV essentially ignore correlations between R_S and R_P and the other parameters.

The results of the fits are partially illustrated in Figs. 8 to 12, which are labeled with an abbreviated notation in which σ_{ij} stands for the observable $P_{\text{lab}}{}^2\rho_{ij}d\sigma/dm$ (not to be confused with the intensity parameter $\bar{\sigma}_{ij}$). Figure 8 shows the 4-GeV/c $\pi\pi$ mass spectra for small $-t$. The results of the fits, including contributions from σ_{SS} and P-D interference, are also plotted. The fits were made over the interval $0.64 < m_{\pi\pi} < 0.94$ GeV and did not take

TABLE IV. Results of the $K\pi$ mass-spectrum fits in the interval $0.74 < m_{K\pi} < 1.04$ GeV and $-t < 0.2$ GeV^2. The parameters are defined in Tables I and II; fits were performed in both the s- and t-channel helicity frames. The sign of p_{lab} indicates the beam polarity ($K^- p$ or $K^+ n$). The values of $\delta_S{}^{1/2}$ are calculated from the fitted phase-shift parameters at $m_{K\pi} = 900$ MeV. The absolute mass-scale uncertainty is estimated to be ±1.5 MeV.

p_{lab} (GeV/c)	Frame	m_R (MeV)	Γ_R (MeV)	R_P (GeV^{-1})	$a_S{}^{1/2}$ (GeV^{-1})	R_S (GeV^{-1})	$\delta_S{}^{1/2}$ (deg)	a_-	a_+	a_{10}
−3	s	893±1	51±3	12±4	1.7±0.1	−4.3±0.5	35.1	2±2	6±2	1±1
−4	s	895±1	49±2	8±1	1.6±0.1	−4.7±0.3	33.8	3±1	6±1	−1±1
−6	s	893±1	49±3	7±2	1.6±0.1	−4.8±0.4	34.9	0±2	3±2	−1±2
+3	s	897±1	52±3	7±2	1.7±0.1	−4.6±0.4	36.5	5±2	6±2	−1±2
+4	s	896±1	54±2	9±2	1.6±0.1	−4.6±0.2	34.8	0±2	6±2	−2±1
+6	s	894±1	50±2	8±2	1.5±0.1	−4.6±0.3	32.4	1±2	5±2	−2±2
−3	t	893±1	52±3	12±4	1.6±0.1	−4.2±0.5	34.2	6±3	6±2	7±2
−4	t	895±1	49±2	7±1	1.6±0.1	−4.6±0.2	35.5	8±2	6±1	4±1
−6	t	894±1	51±3	7±2	1.7±0.1	−4.8±0.4	36.3	5±3	4±2	4±2
+3	t	897±1	54±2	6±1	1.6±0.1	−4.7±0.3	35.8	6±2	6±2	1±1
+4	t	897±1	52±2	6±1	1.6±0.1	−4.7±0.2	33.8	6±1	6±2	3±1
+6	t	895±1	51±2	7±1	1.4±0.1	−4.7±0.3	29.5	8±2	5±2	3±1

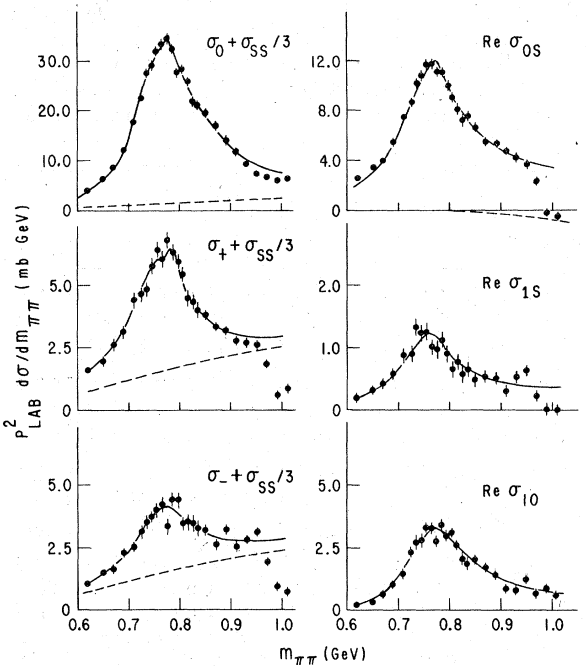

FIG. 8. Mass dependence of the $\pi N \to \pi^+\pi^- N$ observables $\sigma_{ij} \equiv p_{1ab}{}^2 \rho_{ij} d\sigma/dm$, obtained by integrating the parameters defined by Eq. (3.1) over the interval $-t < 0.08$ GeV^2 at 4 GeV/c in the s-channel helicity frame. The data points represent an average of the $\pi^- p$ and $\pi^+ n$ reactions (1.1) and (1.2); the solid curves result from the mass-spectrum fit described in the text. The dashed curve in Reσ_{0S} shows the contribution from P-D interference, while the dashed curves in σ_0, σ_+, and σ_- show the S-wave contribution, $\sigma_{SS}/3$.

into account the $S^*(980)$ effect, which is evident in all observables except Reσ_{10} (no S-wave contribution) and $\sigma_0 + \sigma_{SS}/3$ (where σ_{SS} is relatively small). The $K\pi$ spectra at 4 GeV/c were fitted over the range $0.74 < m_{K\pi} < 1.04$ GeV and are shown in Figs. 9 and 10 for small $-t$ and in Figs. 11 and 12 for larger $-t$. The dashed curves in Figs. 8, 9, and 11 depict the $\sigma_{SS}/3$ background, which is important only for small $-t$.

The S- and P-wave phase-shift parameters a_S, R_S, m_R, Γ_R, and R_P in Tables III and IV do not appear to vary systematically with energy, momentum transfer, or choice of reference frame. Our results for $-t < 0.2$ GeV^2, averaged over incident momenta, may be compared with previous experimental determinations as follows:

(1) ρ^0 mass and width. A simple average of the t-channel parameters in Table III gives $m_\rho = 769 \pm 3$ MeV and $\Gamma_\rho = 152 \pm 9$ MeV, where the errors denote rms spreads. The particle data group[41] averages from previous experiments on neutral ρ's are $m_\rho = 770.2 \pm 0.9$ MeV and $\Gamma_\rho = 150.3 \pm 2.7$ MeV. Our values are also consistent with those obtained from various fits to the 17-GeV/c data reported by Grayer *et al.*,[3] namely m_ρ in the range 771 to 778 MeV and $\Gamma_\rho = 152$ to 163 MeV.

(2) K^{*0} mass and width. A simple average of all the K^{*0} and $\overline{K}^{*0}$ parameters in Table IV gives $m_{K^*} = 894.9 \pm 1.6$ MeV and $\Gamma_{K^*} = 51.2 \pm 1.7$ MeV, where the errors denote rms spreads. The Particle Data Group compilation[41] gives $m_{K^{*0}} = 896.2 \pm 0.4$ MeV and $\Gamma_{K^{*0}} = 50.0 \pm 1.0$ MeV.

(3) $\pi\pi$ S-wave phase shifts. A simple average of the s-channel S-wave parameters in Table III gives $a_S^0 = 2.7 \pm 0.2$ GeV^{-1} and $R_S = -4.3 \pm 0.1$ GeV^{-1}. Over the mass range $0.64 < m_{\pi\pi} < 0.94$ GeV, the values of δ_S^0 derived from these parameters agree with previous determinations within the considerable statistical and systematic uncertainties. Values of δ_S^0 evaluated at $m_{\pi\pi} = 0.775$ GeV are found to be $76^\circ \pm 6^\circ$ (this experiment); $70^\circ < \delta_S^0 < 80^\circ$ (Protopopescu *et al.*[38] solutions "*a*" and "*c*"); $73^\circ \pm 7^\circ$ (Baton *et al.*[42]); and $70^\circ < \delta_S^0 < 90^\circ$ (Männer,[39] solutions A, B, C, D, and E). All of these "down" solutions exhibit the same slow variation with mass in the ρ region, with δ_S^0 increasing nearly linearly by 15° every 100 MeV. The value of δ_S^0 is of course mildly correlated with the behavior assumed for

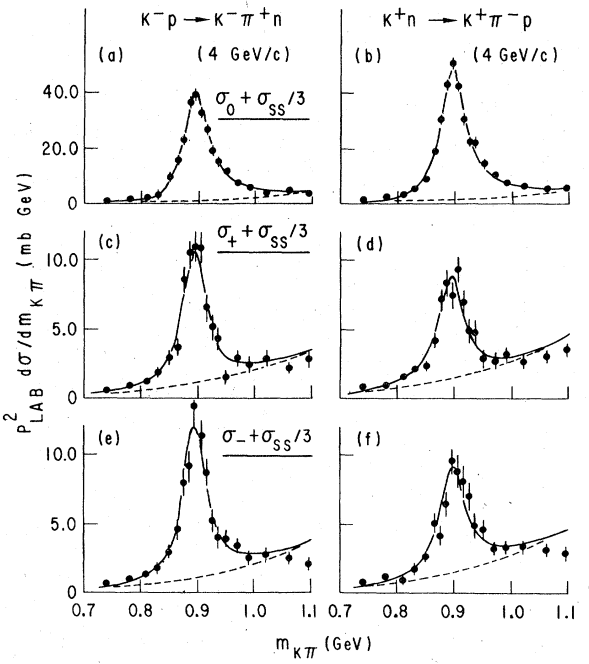

FIG. 9. Mass dependence of the $KN \to K\pi N$ observables $\sigma_{ij} \equiv p_{1ab}{}^2 \rho_{ij} d\sigma/dm$, obtained by integrating the parameters defined by Eq. (3.1) over the interval $-t < 0.2$ GeV^2 at 4 GeV/c in the s-channel helicity frame. The solid curves result from the mass-spectrum fit described in the text; the dashed curves show the S-wave contribution, $\sigma_{SS}/3$.

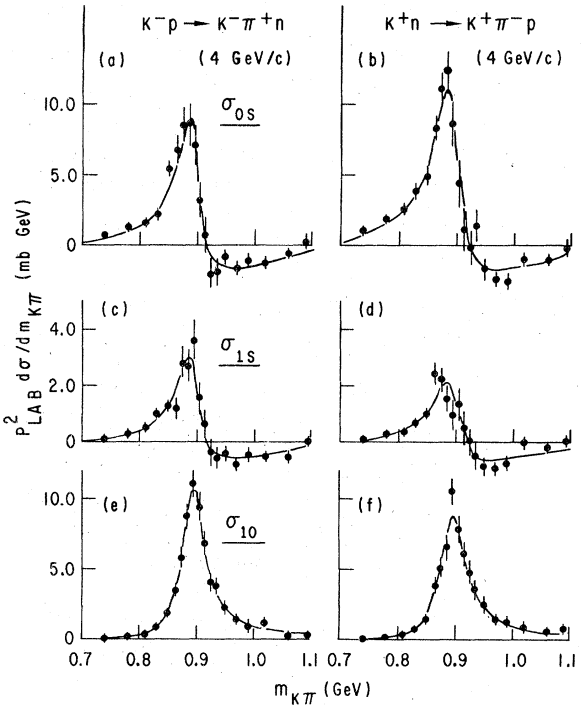

FIG. 10. Mass dependence of the interference terms in $KN \to K\pi N$ for $-t < 0.2$ GeV^2 at 4 GeV/c in the s-channel helicity frame. The notation is the same as that used in Fig. 9.

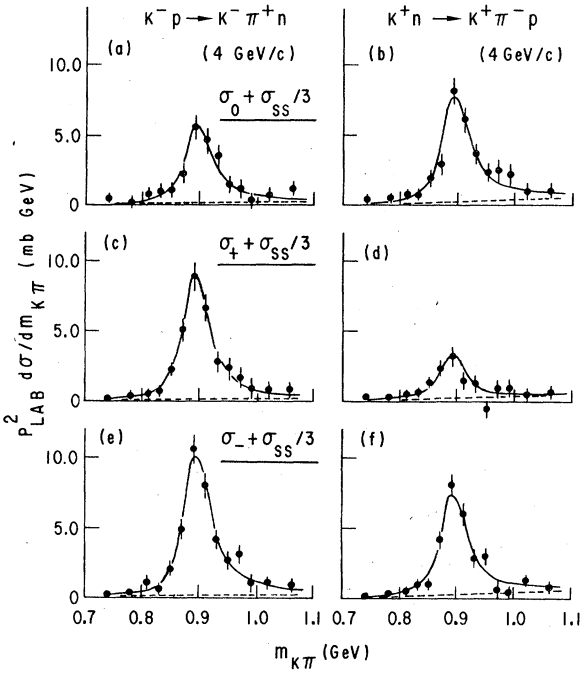

FIG. 11. Mass dependence of the $KN \to K\pi N$ observables for $0.2 < -t < 0.5$ GeV^2 at 4 GeV/c in the s-channel helicity frame. The notation is the same as that used in Fig. 9.

$\delta_S{}^2$; the parametrization of $\delta_S{}^2$ in Table I was chosen to agree with the phase shifts determined by Höogland *et al.*[40]

(4) $K\pi$ S-wave phase shifts. A straight average of the $K\pi$ S-wave parameters from Table IV gives $a_S{}^{1/2} = 1.6 \pm 0.1$ GeV^{-1} and $R_S = -4.6 \pm 0.2$ GeV^{-1}. Evaluated at $m_{K\pi} = 0.9$ GeV, the corresponding S-wave $K\pi$ phase shift has an average value $\delta_S{}^{1/2} = 35^\circ \pm 2^\circ$. Effective-range parametrizations of previous $K\pi$ phase-shift analyses are provided by Griss and Fox.[43] Their analysis of data at 2 and 3.6 GeV/c on reactions (1.3) and (1.4) give $\delta_S{}^{1/2} = 36^\circ \pm 4^\circ$ at $m_{K\pi} = 0.9$ GeV. Analyses of the reaction $K^+p \to K^+\pi^-\Delta^{++}$ give comparable values for this quantity, namely $\delta_S{}^{1/2} = 37^\circ \pm 4^\circ$ (Bingham *et al.*[40]) and $\delta_S{}^{1/2} = 41^\circ \pm 5^\circ$ (Matison *et al.*[44]). The value of $\delta_S{}^{1/2}$ is weakly correlated with the choice of $\delta_S{}^{3/2}$, for which we have adopted essentially the same parametrization used by Bingham *et al.*[40]

The $S^*(980)$ effect, which is not included in our parametrization, is evident around 1 GeV in the $\pi\pi$ mass spectra. Near $K\bar{K}$ threshold the $\pi\pi$ S-wave scattering amplitude becomes highly inelastic, causing the S-P interference terms and σ_{ss} to become very small.[38] In particular, around 1 GeV, the observables σ_0, σ_+, and σ_- should receive

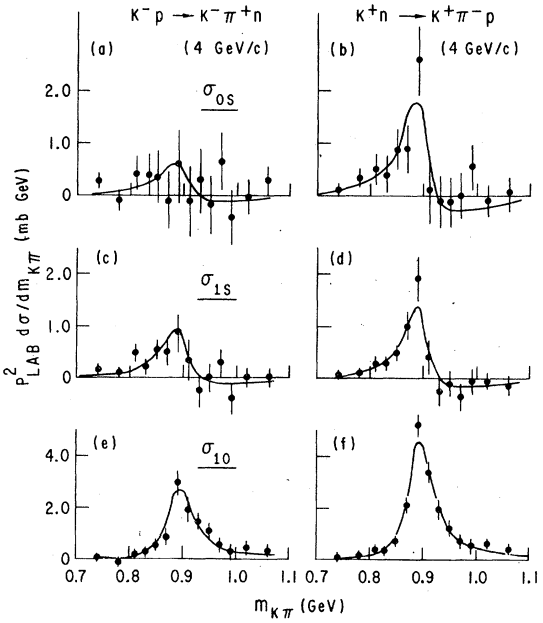

FIG. 12. Mass dependence of the interference terms in $KN \to K\pi N$ for $0.2 < -t < 0.5$ GeV^2 at 4 GeV/c in the s-channel helicity frame. The notation is the same as that used in Fig. 9.

only P-wave contributions and they should become equal to the differences between the dashed and solid curves in Fig. 8, since these differences are meant to describe the tail of the ρ meson. That this is in fact the case lends support to our parametrization of the S-wave below the S^* region.

It is apparent that the dashed curves (showing the $\sigma_{ss}/3$ contribution) in Figs. 8, 9, and 11 describe backgrounds as well as would empirical polynomial fits, while at the same time the parametrization is able to account for the behavior of σ_{0s} and σ_{1s}. We emphasize that at small $-t$ the S wave is important as a source of background only in the observables $\sigma_\pm$. A rough estimate for both $\pi\pi$ and $K\pi$ is that in the s channel $\rho_{ss} \approx 0.18\rho_{00}$.

The mass-spectrum fits also give information on the mass dependence of the production amplitudes $P_\pm$ and on the relative phases of P_- and P_0. For the $K\pi$ data the mass-dependence parameters $a_\pm$ and a_{10} are poorly determined owing to the smallness of the K^* width. For dipion production $P_\pm$ appear to fall faster with m than predicted by the WM; for $-t < 0.08$ GeV^2, the t-channel $\pi\pi$ parameters averaged over incident momenta are $a_+ = 2.9 \pm 0.4$ and $a_- = 3.7 \pm 0.5$, to be compared with the WM prediction $a_\pm \approx 2$. Similar behavior is found in the 17-GeV/c dipion production data.[31] Since t-channel $P_\pm$ correspond to pure absorptive cuts in the WM [see Eq. (3.19)], the fact that $a_\pm > 2$ suggests the existence of some dynamical mechanism for reducing absorption at higher masses.[45] In the s channel, a_- tends to be smaller than the value $a_- = 2$ predicted by the WM; this is consistent with high-mass damping of the absorptive cuts, since in the s channel the absorptive cuts contribute destructively to P_-. Since P_0 is assumed to have no explicit mass dependence we expect $a_{10} \approx a_-/2$, consistent with the data. In subsequent analysis of the production amplitudes we will ignore this explicit mass dependence of $P_\pm$ and work with mass-averaged observables.

We have omitted the intensity parameters $\tilde{\sigma}_{ij}$ from Tables III and IV because the production amplitudes will be examined in more detail in Sec. IV. However, the parameters $\mathrm{Im}\tilde{\sigma}_{1s}$ and $\mathrm{Re}\tilde{\sigma}_{1S}$ can give unique constraints on the relative phases of P_- and P_0. By comparing the mass dependence of σ_{1S} and σ_{0S}, we can use the S wave as a reference for the phases of P_- and P_0, denoted by Δ_- and Δ_0, respectively. This idea can be illustrated with the s-channel S-P interference spectra in Fig. 10. For $K\pi$ final states, σ_{0S} has a zero around 920 MeV; this is observed in other $K\pi$ experiments[6,44] and fixes the phase-shift difference, $\delta_S - \delta_P$, to be 90° at this mass. If P_- had a substantially different production phase from P_0, then σ_{1S} would have a zero displaced in mass from 920 MeV; the zero in σ_{1S} would occur at a mass m_c, defined by

$$\delta_P(m_c) - \delta_S(m_c) - (\Delta_- - \Delta_0) = 90°. \tag{3.24}$$

Numerically, a 1-MeV shift in m_c implies a change in $(\Delta_- - \Delta_0)$ of about 1.4°. Figure 10 shows that the zeros in σ_{1s} and σ_{0s} coincide within a few MeV for small $-t$, while from Fig. 12 we can conclude very little about $(\Delta_- - \Delta_0)$ at large $-t$.

From our parametrization in Table II we can derive the relation

$$\tan(\Delta_- - \Delta_0) = \frac{\mathrm{Im}\tilde{\sigma}_{1s}}{\mathrm{Re}\tilde{\sigma}_{1s}}. \tag{3.25}$$

This equality does not require perfect spin coherence between P_- and P_0; Δ_- should be regarded as the phase of the (presumably dominant) component of $P^-_{\lambda\lambda'}$ which is spin coherent with S and P_0. A straight average of the fitted results from 3.4 and 6 GeV/c gives s-channel $(\Delta_- - \Delta_0) = 3° + 8°$ for $\bar{K}^{*0}$ and $14° \pm 10°$ for K^{*0} production ($-t < 0.2$ GeV^2).

For ρ^0 production the same technique is much more uncertain because the S and P waves are nearly in phase at the ρ mass. The parameter of interest, $\mathrm{Im}\tilde{\sigma}_{1s}$, is determined by the shapes of σ_{0s} and σ_{1s} in the wings of the ρ Breit-Wigner rather than by the locations of clearcut zeros, and is therefore subject to worse systematic errors such as uncertainties in the treatment of the $\pi\pi$ D wave. On the average we obtain s-channel ρ-production phases $(\Delta_- - \Delta_0) \approx 0°$ to 20°.

E. Summary

To summarize this section: (1) We have parametrized the S- and P-wave phase shifts and have verified that the S-wave amplitude derived from the S-P interference terms gives a consistent description of the background, σ_{ss}, under the ρ and K^* peaks. (2) As a by-product of the mass-spectrum fits we find that the mass dependence of $P_\pm$ for ρ production deviates from the WM predictions, suggesting a falloff of absorption with increasing mass. (3) Using the S wave as an analyzer, we find that at small $-t$, P_- and P_0 are approximately coherent in phase (within ~ 20°), consistent with π-exchange dominance.

IV. MOMENTUM-TRANSFER DEPENDENCE

In this section we extract the pure P-wave observables as functions of t for ρ^0, K^{*0}, and $\bar{K}^{*0}$ production using the S- and P-wave phase-shift parameters obtained in Sec. III. Since π-exchange dominance at small $-t$ is the basis for the assumptions that are needed to separate S- and P-wave production we examine the reaction $\pi^- p \to \pi^- \pi^+ n$ in more detail; this reaction should give a relatively

clean and statistically precise picture of the π-exchange mechanism, including shrinkage and absorptive effects. The K^* production reactions allow B and ρ as well as the π and A_2 exchanges that contribute to $\pi^- p \to \pi^-\pi^+ n$, and we defer detailed analysis of the K^* reactions to Sec. VI. We proceed in the following order: We first separate the S- and P-wave observables as functions of t and so obtain the t dependence of pure vector-meson production; we then use the parameters obtained from this analysis to study the energy dependence of helicity-0 dipion production; finally we examine the helicity-1 ρ^0 production observables for information on absorptive effects and natural-parity exchange. For convenience and brevity the shorthand notation

$$\sigma_{ij}(t) \equiv p_{\rm lab}{}^2 \rho_{ij}\, d\sigma/dt \equiv p_{\rm lab}{}^2 d\sigma_{ij}/dt \tag{4.1}$$

will be used throughout this section.

A. Separation of S- and P-wave differential cross sections

In order to study t dependence we have binned the data in coarse mass intervals centered at the K^* and ρ^0 masses: $0.84 < m_{K\pi} < 0.94$ GeV and $0.70 < m_{\pi\pi} < 0.85$ GeV, excluding the ρ-ω interference band $0.775 < m_{\pi\pi} < 0.795$ GeV.[46] The assumptions discussed in Sec. III C suggest that the helicity-0 production amplitudes be expressed as

$$P_0(t) = cN \frac{\sqrt{-t}}{\mu^2 - t}\, e^{B_P(t-\mu^2)}\,, \tag{4.2a}$$

$$S(t) = r_s\, cN \frac{\sqrt{-t}}{\mu^2 - t}\, e^{B_S(t-\mu^2)}\,, \tag{4.2b}$$

where N is defined by Eq. (3.7) and r_s, c, B_S, and B_P are free parameters. P_0 and S are assumed to be spin coherent and to have the same phase. The WM prescription given by Eqs. (3.17) and (3.19) would impose the following constraints[47]:

$$B_S = B_P, \tag{4.3a}$$

$$r_s\, c = (G_{\pi NN}{}^2/2\pi m_N{}^2)^{1/2} = 3.6\ \text{mb}^{1/2}\,, \tag{4.3b}$$

$$r_s(t \text{ chan}) = 1\,, \tag{4.3c}$$

$$r_s(s \text{ chan}) = [\cos\chi(t=\mu^2)]^{-1} \approx 0.94\,. \tag{4.3d}$$

We have fitted the helicity-0 observables in the t interval $t_{\rm min} < -t < 0.28$ GeV^2 to determine the parameters r_s, c, B_S, and B_P for each energy and reaction. The expressions used for the fits are based on Eqs. (3.4) and (3.6), namely

$$p_{\rm lab}{}^2\left(\rho_{00} + \frac{\rho_{ss}}{3}\right)\frac{d\sigma}{dt} = \left[\, P_0(t)^2 \int_{m_1}^{m_2} |f_P(m)|^2\, dm + \frac{S(t)^2}{3}\int_{m_1}^{m_2} |f_S(m)|^2\, dm\right]\frac{1}{N^2} \tag{4.4a}$$

$$p_{\rm lab}{}^2 \,\mathrm{Re}(\rho_{0s})\frac{d\sigma}{dt} = P_0(t)S(t) \times \int_{m_1}^{m_2} \mathrm{Re}[f_S^*(m) f_P(m)]\, dm/N^2, \tag{4.4b}$$

where $f_S(m)$ and $f_P(m)$ have been fixed by the mass-dependent fits of Sec. III, and m_1 and m_2 correspond to the mass intervals defined at the beginning of this section. These fits gave a total χ^2/degree of freedom of $\frac{58}{56}$ for $K\pi$ data and $\frac{254}{196}$ for $\pi\pi$ in the t channel. We have applied the same parametrization to the 13-GeV/c $K^-\pi^+$ data[5] and the 17-GeV/c $\pi\pi$ data.[3] Although the fits to the 17-GeV/c data indicate a systematic discrepancy at very small $-t$ ($-t < 0.02$ GeV^2), the parametrization describes the bulk of the data quite well and allows us to separate the S- and P-wave cross sections. The S-wave "background" cross section can be computed from the fits using the relation

$$I_s(t) = S(t)^2 \int_{m_1}^{m_2} |f_S(m)^2 dm/N^2. \tag{4.5}$$

Empirically, the S-wave cross sections obtained from the fits are equal in the s and t channels within errors, as required physically; we have arbitrarily used the t-channel fits to perform S-wave background subtractions.

Table V lists the P-wave observables for ρ and K^* production corrected for S-wave backgrounds, for the $K^* \to K^\pm\pi^\mp$ branching ratio, and the Breit-Wigner tails excluded by our mass cuts. Explicitly Table V gives the quantities

$$\sigma_{0,+,-} = f_I A\left[\, p_{\rm lab}{}^2(\rho_{0,+,-})\frac{d\sigma}{dt} - \tfrac{1}{3} I_s(t)\right]\,, \tag{4.6a}$$

$$\sigma_{10} = f_I A\, p_{\rm lab}{}^2\, \mathrm{Re}(\rho_{10})\frac{d\sigma}{dt}\,, \tag{4.6b}$$

$$\sigma_{ss} = f_I A\, I_s(t)\,, \tag{4.6c}$$

where $f_I(\pi\pi) = 1$ and $f_I(K\pi) = \frac{3}{2}$; the factor A corrects for the finite mass interval and is given numerically by $A(\pi\pi) = 2.194$, $A(K\pi) = 1.301$; the S-wave background correction $I_s(t)$ is given by Eq. (4.5). The correction for Breit-Wigner tails given by A is somewhat arbitrary; we have defined the total vector-meson cross section as an integral of $|f_P(m)|^2$ from threshold to a mass

TABLE V. Differential cross sections and density-matrix-element projections as functions of t. The differential cross sections are abbreviated $\sigma_{ij} \equiv p_{\rm lab}{}^2 \rho_{ij} d\sigma/dt$ and are given in units of mb; σ_+, σ_0, σ_-, and σ_{10} describe pure P-wave $K\pi$ and $\pi\pi$ production, corrected for decay branching ratios and Breit-Wigner tails. The total P-wave cross section is $\sigma_P = \sigma_0 + \sigma_+ + \sigma_-$; the S-wave background σ_{SS} is normalized such that σ_{SS}/σ_P is equal to the ratio of S- to-P-wave production in the $\pi\pi$ or $K\pi$ mass interval used, namely $0.84 < m_{K\pi} < 0.94$ GeV and $0.70 < m_{\pi\pi} < 0.85$ GeV, excluding the ω band $0.775 < m_{\pi\pi} < 0.795$ GeV. To recover the raw cross sections for $\pi^+\pi^-$ or $K^\pm\pi^\mp$ production in these mass intervals, the quantities given in the table should be divided by 1.95 for $K\pi$ or by 2.19 for $\pi\pi$. The overall normalization uncertainty of ±6% is not included in the errors quoted; however, a ±15% systematic uncertainty has been added in quadrature for σ_{SS}, and thus also contributes to uncertainties in the subtracted P-wave cross sections.

				t-channel frame			s-channel frame		
$-t$ (GeV^2)	σ_P	σ_{SS}	σ_+	σ_0	σ_-	σ_{10}	σ_0	σ_-	σ_{10}
				(a) $K^-p \to \overline{K}^{*0}n$ at 3 GeV/c					
0.01–0.02	41.5 ±5.2	5.9 ±2.2	3.5 ±2.1	33.7 ±4.2	4.2 ±2.1	−3.7 ±1.6	34.3 ±4.2	3.8 ±2.1	1.3 ±1.6
0.02–0.04	51.0 ±4.1	5.4 ±2.0	6.9 ±1.6	39.6 ±3.2	4.4 ±1.6	−6.3 ±1.1	40.0 ±3.2	4.1 ±1.5	5.9 ±1.2
0.04–0.08	41.9 ±2.7	3.7 ±1.4	5.9 ±1.1	31.5 ±2.2	4.4 ±1.1	−5.81±0.75	27.8 ±2.0	8.0 ±1.2	8.20±0.82
0.08–0.12	26.6 ±2.2	2.28±0.94	5.1 ±1.2	18.8 ±1.8	2.8 ±1.1	−2.68±0.70	12.5 ±1.6	9.0 ±1.2	6.01±0.75
0.12–0.16	25.9 ±2.3	1.49±0.66	5.3 ±1.4	17.2 ±1.8	3.4 ±1.1	−3.18±0.73	10.7 ±1.7	10.0 ±1.3	5.79±0.76
0.16–0.20	14.9 ±2.2	1.03±0.50	3.8 ±1.9	8.0 ±1.5	2.8 ±1.3	−0.22±0.72	3.7 ±1.6	7.3 ±1.3	1.48±0.68
0.20–0.28	14.8 ±1.8	0.63±0.35	5.3 ±1.8	5.8 ±1.0	3.63±0.97	−1.62±0.52	4.7 ±1.2	4.69±0.88	1.83±0.48
0.28–0.36	7.1 ±2.5	0.34±0.24	3.0 ±2.6	4.2 ±1.1	0.2 ±1.1	0.46±0.59	−0.1 ±1.3	4.2 ±1.0	−0.16±0.55
				(b) $K^+n \to K^{*0}p$ at 3 GeV/c					
0.01–0.02	76.4 ±7.0	9.2 ±2.9	13.7 ±2.8	55.5 ±5.6	7.9 ±2.6	−10.3 ±2.0	57.7 ±5.7	4.1 ±2.3	−1.2 ±2.0
0.02–0.04	68.4 ±5.0	8.4 ±2.6	11.3 ±2.0	48.6 ±3.8	8.7 ±2.0	−11.4 ±1.4	53.0 ±3.9	4.0 ±1.7	4.0 ±1.4
0.04–0.08	46.1 ±3.1	5.7 ±1.9	5.9 ±1.2	33.7 ±2.2	6.8 ±1.3	−9.00±0.81	33.9 ±2.2	5.7 ±1.2	7.23±0.85
0.08–0.12	34.3 ±2.6	3.5 ±1.2	4.2 ±1.1	21.6 ±2.0	8.6 ±1.3	−7.58±0.77	24.0 ±2.0	5.9 ±1.2	6.00±0.80
0.12–0.16	16.3 ±2.0	2.24±0.86	1.4 ±1.1	11.1 ±1.6	3.9 ±1.1	−4.29±0.68	10.8 ±1.5	4.0 ±1.1	4.05±0.70
0.16–0.20	17.6 ±2.3	1.52±0.65	2.2 ±1.7	12.0 ±1.9	3.3 ±1.3	−3.87±0.82	8.8 ±1.8	6.7 ±1.5	5.04±0.83
0.20–0.28	9.4 ±1.7	0.91±0.45	−0.5 ±1.6	5.3 ±1.1	4.41±0.99	−1.89±0.55	5.6 ±1.2	4.18±0.95	1.76±0.52
0.28–0.36	7.4 ±2.6	0.48±0.29	0.6 ±3.0	4.4 ±1.4	2.7 ±1.4	−2.14±0.73	3.4 ±1.6	3.3 ±1.3	2.13±0.71
				(c) $K^-p \to \overline{K}^{*0}n$ at 4 GeV/c					
0.005–0.01	46.1 ±5.8	8.1 ±2.1	5.2 ±2.0	35.3 ±4.9	5.2 ±2.0	−6.1 ±1.7	38.2 ±5.1	3.2 ±1.9	−2.2 ±1.6
0.01–0.02	53.8 ±4.7	9.5 ±2.5	3.5 ±1.5	44.2 ±3.6	6.2 ±1.6	−10.7 ±1.2	49.4 ±3.8	0.8 ±1.4	−0.4 ±1.1
0.02–0.04	58.4 ±3.7	8.6 ±2.3	5.8 ±1.2	45.2 ±2.6	7.1 ±1.3	−11.15±0.90	50.0 ±2.8	2.7 ±1.2	5.45±0.86
0.04–0.08	39.1 ±2.4	5.7 ±1.6	4.27±0.79	31.5 ±1.6	3.31±0.82	−6.21±0.54	28.1 ±1.6	6.73±0.89	8.72±0.57
0.08–0.12	27.1 ±1.7	3.4 ±1.0	6.06±0.72	19.4 ±1.3	1.74±0.70	−3.71±0.48	13.1 ±1.2	7.81±0.83	6.73±0.50
0.12–0.16	22.6 ±1.5	2.12±0.74	6.43±0.70	12.6 ±1.1	3.25±0.69	−3.80±0.45	10.5 ±1.1	5.92±0.77	4.85±0.46
0.16–0.20	17.2 ±1.3	1.39±0.57	5.18±0.68	10.41±0.97	1.45±0.67	−2.26±0.41	5.30±0.91	6.88±0.77	3.95±0.43
0.20–0.28	13.54±0.84	0.80±0.42	3.99±0.50	7.17±0.59	2.27±0.48	−1.46±0.28	3.81±0.58	5.86±0.52	2.22±0.27
0.28–0.36	9.29±0.77	0.40±0.30	4.18±0.62	3.63±0.48	1.58±0.51	−0.39±0.25	1.75±0.55	3.41±0.45	0.60±0.24
0.36–0.45	6.20±0.74	0.20±0.22	2.52±0.62	2.37±0.39	1.31±0.48	−0.62±0.21	1.34±0.49	2.31±0.38	0.66±0.20
0.45–0.60	4.97±0.67	0.08±0.15	2.40±0.65	1.66±0.31	0.93±0.41	−0.01±0.16	0.78±0.40	1.72±0.32	0.01±0.16
0.60–0.90	2.11±0.52	0.02±0.15	0.61±0.50	0.93±0.21	0.55±0.29	−0.09±0.11	0.47±0.26	0.98±0.23	0.02±0.12

TABLE V. (*Continued*)

$-t$ (GeV^2)	σ_P	σ_{SS}	σ_+	t-channel frame σ_0	σ_-	σ_{10}	s-channel frame σ_0	σ_-	σ_{10}
				(d) $K^+n \to K^{*0}p$ at 4 GeV/c					
0.005–0.01	66.0 ±6.9	8.5 ±2.3	9.2 ±2.6	47.3 ±6.0	8.5 ±2.6	−6.5 ±2.1	50.9 ±6.2	6.6 ±2.5	−2.0 ±2.1
0.01–0.02	81.5 ±5.7	10.1 ±2.7	9.7 ±2.0	56.0 ±4.5	15.7 ±2.3	−13.9 ±1.7	63.7 ±4.8	8.1 ±2.0	−2.4 ±1.6
0.02–0.04	64.2 ±4.0	9.3 ±2.5	5.8 ±1.3	47.2 ±2.9	10.9 ±1.5	−12.5 ±1.0	54.1 ±3.1	4.6 ±1.3	4.04±0.97
0.04–0.08	44.8 ±2.6	6.5 ±1.8	5.49±0.89	31.4 ±1.7	7.9 ±1.0	−10.10±0.60	35.5 ±1.8	3.81±0.89	6.53±0.59
0.08–0.12	30.6 ±2.0	4.1 ±1.2	2.83±0.66	21.1 ±1.3	6.85±0.88	−7.37±0.53	22.5 ±1.4	5.20±0.76	6.48±0.52
0.12–0.16	21.8 ±1.6	2.70±0.88	3.34±0.62	12.6 ±1.1	5.67±0.79	−5.59±0.45	14.6 ±1.2	4.04±0.70	4.98±0.46
0.16–0.20	14.9 ±1.4	1.89±0.67	3.06±0.60	9.3 ±1.0	2.55±0.68	−3.80±0.42	7.71±0.96	4.27±0.73	4.37±0.44
0.20–0.28	10.52±0.85	1.18±0.48	1.37±0.37	5.71±0.54	3.38±0.49	−2.66±0.26	5.46±0.60	3.59±0.44	2.70±0.26
0.28–0.36	6.56±0.72	0.66±0.32	0.99±0.46	4.33±0.49	1.29±0.45	−1.92±0.23	2.18±0.50	3.45±0.44	2.14±0.23
0.36–0.45	5.22±0.72	0.38±0.22	1.63±0.60	1.98±0.40	1.63±0.47	−1.14±0.21	1.76±0.49	1.80±0.38	1.14±0.21
0.45–0.60	2.23±0.57	0.19±0.13	0.44±0.59	1.25±0.31	0.61±0.37	−0.38±0.15	0.39±0.35	1.32±0.32	0.28±0.15
0.60–0.90	1.92±0.78	0.06±0.05	0.53±0.88	0.51±0.33	0.73±0.42	−0.19±0.17	0.60±0.36	0.70±0.37	0.22±0.17
				(e) $K^-p \to \bar{K}^{*0}n$ at 6 GeV/c					
0.002–0.01	47.2 ±7.0	5.2 ±1.9	2.2 ±2.4	38.6 ±6.8	6.1 ±2.7	−5.3 ±2.3	41.0 ±6.9	4.3 ±2.6	−0.2 ±2.3
0.01–0.02	68.0 ±7.3	7.0 ±2.6	8.5 ±2.5	53.1 ±6.7	6.8 ±2.6	−11.1 ±2.2	56.7 ±6.8	2.6 ±2.3	2.4 ±2.1
0.02–0.04	50.1 ±4.9	6.3 ±2.4	6.4 ±1.7	40.7 ±4.1	3.5 ±1.8	−8.6 ±1.4	40.9 ±4.2	2.5 ±1.7	7.1 ±1.3
0.04–0.08	39.1 ±3.1	4.2 ±1.6	6.6 ±1.1	28.4 ±2.5	4.4 ±1.2	−6.50±0.92	26.5 ±2.5	5.8 ±1.2	7.30±0.91
0.08–0.12	22.4 ±2.3	2.5 ±1.0	6.61±0.98	15.0 ±1.9	0.7 ±1.1	−1.94±0.79	8.7 ±1.9	7.2 ±1.2	5.45±0.79
0.12–0.16	20.9 ±2.2	1.54±0.67	5.28±0.89	11.3 ±1.7	4.6 ±1.2	−2.31±0.80	8.9 ±1.8	6.8 ±1.2	3.20±0.76
0.16–0.20	17.3 ±1.9	1.01±0.48	6.81±0.92	8.1 ±1.5	2.4 ±1.2	−2.09±0.75	5.7 ±1.6	4.8 ±1.2	2.94±0.70
0.20–0.28	13.1 ±1.1	0.57±0.32	6.18±0.59	5.65±0.85	1.27±0.68	−1.47±0.41	2.83±0.85	4.11±0.70	2.13±0.40
0.28–0.36	9.5 ±1.0	0.28±0.20	4.79±0.55	3.85±0.74	0.75±0.69	−0.63±0.40	1.03±0.79	3.77±0.69	1.00±0.39
0.36–0.45	6.04±0.84	0.14±0.13	3.11±0.45	2.17±0.60	0.78±0.64	−0.43±0.36	0.73±0.69	2.13±0.57	0.47±0.35
0.45–0.60	4.55±0.65	0.06±0.07	3.01±0.43	0.64±0.40	0.93±0.51	−0.11±0.26	0.85±0.50	0.68±0.40	0.12±0.26
0.60–0.90	2.40±0.44	0.01±0.03	1.62±0.30	0.38±0.24	0.36±0.37	0.05±0.16	0.40±0.33	0.40±0.26	−0.04±0.17
				(f) $K^+n \to K^{*0}p$ at 6 GeV/c					
0.002–0.01	90.0 ±9.0	5.9 ±2.0	11.0 ±3.4	65.1 ±8.8	13.6 ±3.5	−7.7 ±3.0	67.5 ±8.9	11.4 ±3.4	0.0 ±3.0
0.01–0.02	86.8 ±7.9	7.9 ±2.7	11.4 ±2.9	65.3 ±7.1	10.4 ±2.8	−15.6 ±2.5	72.7 ±7.5	2.5 ±2.3	1.5 ±2.3
0.02–0.04	69.4 ±5.2	7.0 ±2.4	9.4 ±1.8	48.9 ±4.3	11.7 ±2.0	−15.6 ±1.6	57.6 ±4.6	1.8 ±1.6	3.4 ±1.4
0.04–0.08	50.5 ±3.1	4.4 ±1.6	5.8 ±1.1	34.1 ±2.5	11.0 ±1.4	−9.9 ±1.0	37.7 ±2.7	6.8 ±1.2	6.64±0.93
0.08–0.12	27.9 ±2.2	2.45±0.92	2.23±0.72	20.0 ±1.8	5.8 ±1.1	−6.55±0.77	20.2 ±1.9	5.30±0.94	6.53±0.71
0.12–0.16	21.2 ±1.9	1.44±0.59	4.07±0.74	10.7 ±1.4	6.9 ±1.1	−4.77±0.68	13.3 ±1.6	3.69±0.93	3.49±0.64
0.16–0.20	15.3 ±1.7	0.89±0.40	1.76±0.58	9.5 ±1.4	4.2 ±1.0	−3.77±0.65	9.1 ±1.4	4.30±0.97	3.79±0.62
0.20–0.28	9.83±0.88	0.46±0.25	1.34±0.33	4.64±0.64	3.87±0.59	−2.52±0.35	5.83±0.74	2.59±0.50	2.25±0.33
0.28–0.36	7.37±0.77	0.20±0.14	1.35±0.32	3.74±0.58	2.34±0.54	−1.67±0.32	3.18±0.62	2.84±0.51	1.73±0.31
0.36–0.45	4.93±0.61	0.09±0.08	0.94±0.28	2.04±0.44	1.99±0.47	−0.94±0.26	2.07±0.50	1.91±0.42	0.95±0.26
0.45–0.60	3.19±0.42	0.03±0.04	1.07±0.24	1.37±0.29	0.72±0.33	−0.72±0.18	0.70±0.33	1.44±0.30	0.73±0.18
0.60–0.90	1.22±0.28	0.01±0.01	0.68±0.19	0.22±0.17	0.37±0.24	0.02±0.11	0.32±0.21	0.21±0.19	−0.01±0.11

TABLE V. (*Continued*)

$-t$ (GeV^2)	σ_P	σ_{SS}	σ_+	t-channel frame σ_0	σ_-	σ_{10}	s-channel frame σ_0	σ_-	σ_{10}
				(g) $\pi^-p\to\rho^0n$ at 3 GeV/c					
0.015–0.02	150.3 ±6.6	22.6 ±3.1	18.2 ±2.2	115.6 ±6.2	16.5 ±2.1	−16.9 ±2.0	121.9 ±6.3	10.2 ±2.0	−0.3 ±1.9
0.02–0.03	140.0 ±4.9	21.0 ±2.9	16.6 ±1.7	107.7 ±4.1	15.8 ±1.6	−20.7 ±1.3	116.2 ±4.3	7.2 ±1.5	4.2 ±1.3
0.03–0.04	126.4 ±4.5	18.1 ±2.5	15.0 ±1.6	96.9 ±3.8	14.5 ±1.5	−21.3 ±1.3	105.5 ±4.0	5.9 ±1.4	8.7 ±1.2
0.04–0.06	101.8 ±3.1	14.2 ±2.0	12.4 ±1.1	77.3 ±2.5	12.1 ±1.1	−17.25±0.84	81.3 ±2.6	8.1 ±1.0	12.59±0.80
0.06–0.08	82.7 ±2.7	10.2 ±1.5	10.27±0.99	61.6 ±2.2	10.87±0.95	−16.15±0.77	64.3 ±2.3	8.10±0.89	13.81±0.73
0.08–0.10	61.9 ±2.3	7.5 ±1.1	9.32±0.94	44.3 ±1.9	8.25±0.85	−11.64±0.71	43.7 ±2.0	8.90±0.84	12.28±0.67
0.10–0.12	50.5 ±2.0	5.55±0.90	7.99±0.92	35.0 ±1.8	7.48±0.83	−9.97±0.68	33.6 ±1.8	8.87±0.81	10.91±0.66
0.12–0.16	34.8 ±1.3	3.69±0.67	3.58±0.57	25.3 ±1.1	5.93±0.56	−7.38±0.44	22.3 ±1.1	8.87±0.56	8.93±0.42
0.16–0.20	23.9 ±1.2	2.19±0.47	2.37±0.57	17.54±0.94	4.02±0.52	−5.11±0.42	13.39±0.95	8.17±0.54	6.77±0.40
0.20–0.24	17.2 ±1.1	1.34±0.34	3.93±0.77	11.88±0.89	1.38±0.43	−2.65±0.39	5.73±0.80	7.52±0.56	4.50±0.40
0.24–0.28	11.7 ±1.1	0.85±0.26	2.05±0.92	8.06±0.83	1.56±0.48	−1.64±0.42	3.53±0.78	6.09±0.56	2.71±0.41
0.28–0.32	10.1 ±1.4	0.54±0.20	1.0 ±1.2	7.07±0.90	2.01±0.62	−1.52±0.50	3.41±0.91	5.67±0.64	2.18±0.49
0.32–0.36	4.6 ±1.5	0.35±0.16	0.2 ±1.5	4.46±0.90	−0.02±0.52	−0.02±0.49	0.03±0.76	4.41±0.69	0.59±0.49
				(h) $\pi^-p\to\rho^0n$ at 4 GeV/c					
0.005–0.01	125.8 ±5.5	20.5 ±2.5	17.6 ±1.8	90.8 ±5.4	17.5 ±1.7	−12.0 ±1.6	94.3 ±5.4	14.0 ±1.7	−5.1 ±1.6
0.01–0.015	143.8 ±5.0	22.7 ±2.8	17.2 ±1.6	109.8 ±4.5	16.7 ±1.5	−20.7 ±1.3	118.2 ±4.6	8.3 ±1.4	−4.0 ±1.2
0.015–0.02	147.7 ±5.0	22.8 ±2.8	14.7 ±1.5	117.9 ±4.4	15.1 ±1.5	−22.6 ±1.3	127.0 ±4.5	6.0 ±1.4	2.0 ±1.2
0.02–0.03	131.9 ±3.8	21.0 ±2.6	15.1 ±1.2	102.0 ±2.9	14.9 ±1.2	−23.08±0.89	112.4 ±3.0	4.4 ±1.1	4.83±0.81
0.03–0.04	115.7 ±3.4	18.0 ±2.2	13.2 ±1.1	89.8 ±2.6	12.8 ±1.1	−20.16±0.84	96.9 ±2.8	5.6 ±1.0	10.11±0.78
0.04–0.06	93.2 ±2.4	13.9 ±1.7	11.26±0.78	72.1 ±1.7	9.82±0.79	−16.24±0.54	74.9 ±1.7	7.00±0.75	13.18±0.51
0.06–0.08	73.0 ±1.9	9.8 ±1.2	9.34±0.64	55.8 ±1.4	7.90±0.65	−13.75±0.49	56.0 ±1.5	7.72±0.62	13.73±0.46
0.08–0.10	57.5 ±1.6	7.06±0.93	7.64±0.55	42.9 ±1.2	6.93±0.57	−12.08±0.46	42.5 ±1.3	7.30±0.53	12.37±0.42
0.10–0.12	47.5 ±1.4	5.16±0.71	5.91±0.49	35.2 ±1.1	6.38±0.53	−10.01±0.43	33.0 ±1.2	8.64±0.51	11.49±0.40
0.12–0.16	33.53±0.87	3.34±0.50	3.95±0.31	24.79±0.65	4.79±0.35	−7.08±0.26	21.09±0.67	8.50±0.35	8.94±0.25
0.16–0.20	23.27±0.68	1.92±0.34	2.93±0.27	17.17±0.53	3.16±0.30	−4.74±0.23	12.27±0.53	8.07±0.32	6.68±0.22
0.20–0.24	15.20±0.55	1.13±0.24	2.19±0.26	10.73±0.43	2.27±0.28	−2.76±0.20	6.51±0.43	6.50±0.29	4.09±0.19
0.24–0.28	12.11±0.48	0.69±0.19	1.51±0.25	9.04±0.38	1.56±0.26	−2.36±0.18	4.42±0.37	6.18±0.28	3.51±0.18
0.28–0.32	7.85±0.40	0.43±0.15	0.72±0.23	6.20±0.32	0.93±0.24	−1.18±0.16	2.07±0.31	5.06±0.26	1.98±0.16
0.32–0.36	6.70±0.39	0.27±0.13	1.03±0.28	4.55±0.29	1.12±0.26	−1.24±0.15	1.94±0.31	3.73±0.24	1.58±0.15
0.36–0.40	5.35±0.38	0.17±0.12	1.48±0.34	2.80±0.25	1.07±0.27	−0.66±0.13	1.35±0.30	2.52±0.22	0.80±0.13
0.40–0.45	4.26±0.36	0.10±0.12	1.32±0.36	2.69±0.22	0.24±0.22	−0.33±0.11	0.29±0.23	2.65±0.21	0.47±0.11
0.45–0.60	2.73±0.28	0.04±0.17	0.64±0.25	1.22±0.11	0.87±0.16	0.01±0.06	0.84±0.16	1.25±0.12	0.04±0.06
0.60–0.90	−4.75±0.19	0.00±0.00	−5.11±0.19	0.37±0.07	−0.01±0.15	0.34±0.04	0.23±0.13	0.13±0.08	−0.36±0.05

TABLE V. (*Continued*)

$-t$ (GeV^2)	σ_P	σ_{SS}	σ_+	σ_0	t-channel frame σ_-	σ_{10}	σ_0	s-channel frame σ_-	σ_{10}
				(i) $\pi^- p \to \rho^0 n$ at 6 GeV/c					
0.002–0.005	109.0 ± 7.4	17.3 ± 2.2	18.1 ± 2.3	72.6 ± 7.9	18.3 ± 2.3	−11.7 ± 2.2	75.4 ± 8.0	15.5 ± 2.3	−7.8 ± 2.1
0.005–0.01	138.9 ± 6.0	24.6 ± 3.1	20.3 ± 1.9	100.5 ± 5.6	18.0 ± 1.8	−22.0 ± 1.5	109.4 ± 5.8	9.1 ± 1.7	−9.3 ± 1.4
0.01–0.015	146.5 ± 6.2	27.9 ± 3.5	16.5 ± 1.9	111.9 ± 5.5	18.1 ± 1.9	−25.5 ± 1.6	123.8 ± 5.7	6.1 ± 1.7	−4.4 ± 1.4
0.015–0.02	134.9 ± 6.0	27.7 ± 3.5	18.3 ± 1.9	100.0 ± 5.2	16.6 ± 1.9	−23.2 ± 1.5	111.6 ± 5.4	5.0 ± 1.7	0.2 ± 1.3
0.02–0.03	132.3 ± 4.7	25.3 ± 3.2	14.2 ± 1.5	104.6 ± 3.7	13.5 ± 1.5	−23.8 ± 1.1	114.9 ± 3.9	3.2 ± 1.4	7.14 ± 0.97
0.03–0.04	113.7 ± 4.2	21.3 ± 2.7	10.4 ± 1.3	91.2 ± 3.3	12.1 ± 1.3	−20.5 ± 1.0	98.2 ± 3.5	5.2 ± 1.2	11.61 ± 0.91
0.04–0.06	93.6 ± 2.9	16.0 ± 2.1	11.41 ± 0.92	72.3 ± 2.1	9.92 ± 0.94	−18.14 ± 0.67	77.1 ± 2.2	5.15 ± 0.87	12.98 ± 0.59
0.06–0.08	69.7 ± 2.3	10.9 ± 1.4	7.57 ± 0.71	54.9 ± 1.7	7.29 ± 0.76	−13.46 ± 0.60	54.4 ± 1.8	7.75 ± 0.72	13.97 ± 0.54
0.08–0.10	52.1 ± 1.8	7.6 ± 1.1	7.74 ± 0.61	38.9 ± 1.4	5.54 ± 0.65	−10.64 ± 0.53	37.7 ± 1.5	6.70 ± 0.60	11.48 ± 0.47
0.10–0.12	43.2 ± 1.6	5.33 ± 0.79	5.36 ± 0.51	32.0 ± 1.2	5.84 ± 0.61	−8.87 ± 0.51	29.7 ± 1.3	8.17 ± 0.58	10.44 ± 0.46
0.12–0.16	31.03 ± 0.98	3.28 ± 0.55	4.09 ± 0.32	23.21 ± 0.74	3.74 ± 0.37	−6.41 ± 0.30	19.14 ± 0.77	7.81 ± 0.39	8.60 ± 0.28
0.16–0.20	20.56 ± 0.76	1.76 ± 0.37	3.22 ± 0.26	14.65 ± 0.58	2.68 ± 0.33	−4.35 ± 0.26	11.00 ± 0.61	6.33 ± 0.34	5.87 ± 0.24
0.20–0.24	15.07 ± 0.63	0.96 ± 0.27	2.20 ± 0.22	10.61 ± 0.49	2.26 ± 0.31	−3.29 ± 0.24	7.17 ± 0.52	5.70 ± 0.32	4.41 ± 0.22
0.24–0.28	10.33 ± 0.52	0.55 ± 0.21	1.99 ± 0.20	6.86 ± 0.40	1.48 ± 0.28	−1.95 ± 0.20	3.89 ± 0.42	4.45 ± 0.29	2.75 ± 0.18
0.28–0.32	8.55 ± 0.47	0.32 ± 0.19	1.78 ± 0.19	5.49 ± 0.35	1.28 ± 0.27	−1.73 ± 0.18	2.89 ± 0.37	3.88 ± 0.27	2.26 ± 0.17
0.32–0.36	5.33 ± 0.38	0.18 ± 0.18	1.69 ± 0.18	3.17 ± 0.28	0.47 ± 0.23	−0.57 ± 0.14	0.92 ± 0.29	2.72 ± 0.24	0.95 ± 0.14
0.36–0.40	4.94 ± 0.42	0.11 ± 0.28	1.76 ± 0.20	2.66 ± 0.27	0.52 ± 0.24	−0.81 ± 0.14	0.96 ± 0.28	2.22 ± 0.24	1.02 ± 0.13
0.40–0.45	4.29 ± 0.42	0.06 ± 0.33	1.84 ± 0.20	2.03 ± 0.23	0.41 ± 0.23	−0.28 ± 0.11	0.52 ± 0.25	1.92 ± 0.22	0.40 ± 0.11
0.45–0.60	2.75 ± 0.13	0.02 ± 0.02	1.40 ± 0.09	0.89 ± 0.09	0.46 ± 0.12	0.05 ± 0.05	0.52 ± 0.12	0.83 ± 0.08	−0.07 ± 0.05
0.60–0.90	0.58 ± 0.07	0.00 ± 0.00	0.50 ± 0.06	0.08 ± 0.04	−0.00 ± 0.08	0.28 ± 0.03	0.13 ± 0.07	−0.05 ± 0.04	−0.25 ± 0.03

$m_R + 3\Gamma_R$. In Table V we have added a 15% systematic uncertainty to the statistical errors in $\sigma_{ss}(t)$; the uncertainties in the S-wave subtraction are included in the quoted errors for the corrected P-wave cross sections. Overall normalization uncertainties of ±6% have not been included in Table V. We have followed the same procedure to derive corrected cross sections for the 17-GeV ρ and the 13-GeV/c K^* data, although the mass cuts for these data are slightly different.[48]

B. Properties of helicity-0 dipion production

Most of the interesting features of helicity-0 dipion production are expressed in the parameters r_s, c, B_S, and B_P derived from the fits described above. The quantities c and cr_s give the residues of the production amplitudes at the pion pole, while the energy dependence of B_S and B_P bears on the question of Regge shrinkage.

First, a simple average of our 3-, 4-, and 6-GeV/c measurements gives $r_s(t \text{ chan}) = 1.11 \pm 0.07$ and $r_s(s \text{ chan}) = 1.00 \pm 0.06$, where the errors represent the rms spread of the fitted parameters. These values are consistent with those obtained in our fits to the 17-GeV/c data, where $r_s(t \text{ chan}) = 1.12 \pm 0.02$ and $r_s(s \text{ chan}) = 1.00 \pm 0.02$. They are systematically higher than the WM prediction of Eq. (4.3) by an average factor of 1.09.

The experimental values of the intercept c, including systematic normalization uncertainties, are plotted in Fig. 13(c). At all energies these intercepts appear to be systematically lower by about 10% than the WM predictions, which are that $c(t \text{ chan}) = 3.60$ mb$^{1/2}$ and $c(s \text{ chan}) = 3.84$ mb$^{1/2}$. Combining these discrepancies in r_s and c, we conclude that the S-wave residue at the pion pole satisfies the WM prediction of Eq. (4.3b), namely $r_s c \approx 3.60$ mb$^{1/2}$. However, the P-wave residues at the pion pole appear to be low by 10% at all energies. A simple average of the K^* and $\overline{K}^*$ intercepts at 3, 4, and 6 GeV/c gives $c(K^*) = 3.71 \pm 0.22$ mb$^{1/2}$ in the s channel; this lies midway between the WM prediction $c(s \text{ chan}) = 3.84$ mb$^{1/2}$ and the average ρ intercept $c(\rho) = 3.53 \pm 0.05$ mb$^{1/2}$.

The Williams model assumes the equality $B_S = B_P$ [Eq. (4.3a)] to hold in both s and t channels. The P-wave slopes B_P are plotted versus p_{lab} in Fig. 13(a) and the S-wave slopes B_S in Fig. 13(b). Although the equality $B_P \approx B_S$ holds in the s channel, B_P is significantly smaller than B_S in the t channel. To search for Regge shrinkage we have fitted the slopes to the form $B = B_0 + \alpha' \ln p_{\text{lab}}$, which corresponds to the amplitude behavior $P_0 \propto (p_{\text{lab}})^{\alpha' t} e^{B_0 t}$. The resulting Regge slope, α', is the same within errors for the S wave and the s-channel P wave; the P-wave slope is $\alpha' = 0.30 \pm 0.04$ GeV^{-2}. As shown in Fig. 13(a), the P-wave

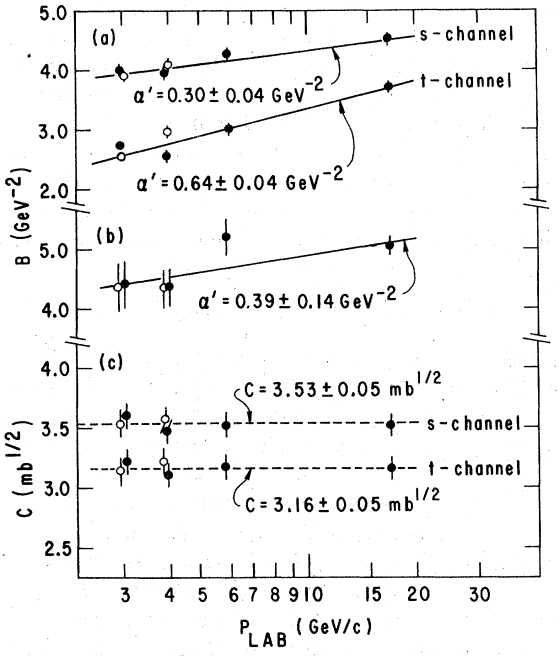

FIG. 13. Energy dependence of the parameters B_P, B_S, and c obtained from the t-dependent fits to the helicity-0 $\pi\pi$ data. The 17-GeV/c points are from fits to the data of Ref. 3. The solid points are from the $\pi^- p$ reaction and the open points are from $\pi^+ n$. The P-wave slope B_P is shown in (a) for both the s and t channels; B_S is shown in (b). The lines result from fits to the form $B = B_0 + \alpha' \ln p_{\rm lab}$, with the values of α' given on the graphs. Part (c) shows the P-wave intercept c in the s and t channels, and its average values.

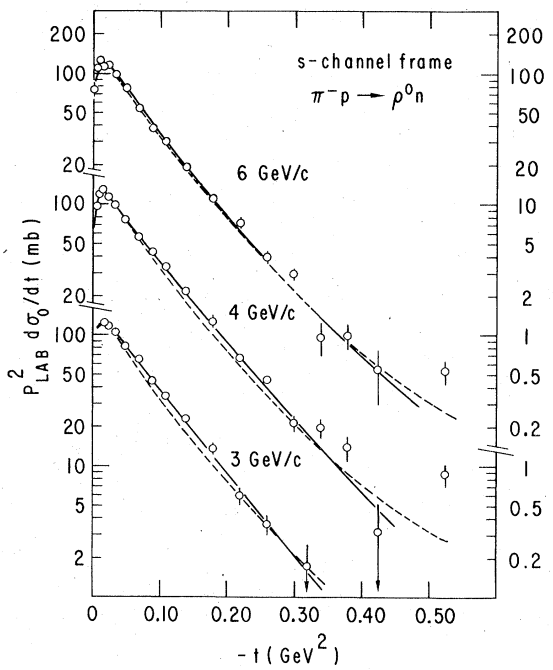

FIG. 14. The P-wave helicity-0 cross sections for ρ^0 production in the s channel at 3, 4, and 6 GeV/c. The solid curves result from the t-dependent fits described in the text and the dashed curves are a smooth interpolation of the 17-GeV/c data of Ref. 3.

shrinkage is considerably greater in the t channel, where $\alpha' = 0.64 \pm 0.04$ GeV^{-2}.

The P-wave helicity-0 cross sections are plotted in Fig. 14 (s channel) and Fig. 15 (t channel) at 3, 4, and 6 GeV/c. A smooth interpolation of the 17-GeV/c data is shown by the dashed curves. It is clear that the s-channel cross sections are highly peripheral and exhibit little $p_{\rm lab}$ dependence, in contrast with t-channel σ_0, which exhibits considerable shrinkage. We emphasize that the modest shrinkage found in the fits to s-channel σ_0 is established only in the region $-t < 0.28$ GeV^2. Because of the statistical uncertainties we can conclude little about energy dependence at larger $-t$ from the data of Fig. 14. The solid curves in Figs. 14 and 15 are obtained from fits over the range $-t < 0.45$ GeV^2 using a parametrization which is discussed in more detail below, in connection with the helicity-1 observables. The fits based on Eq. (4.2a) using $-t < 0.28$-GeV^2 data are consistent with the solid curves in Fig. 14 only out to $-t \approx 0.25$ GeV^2. In the t channel, where the shrinkage in σ_0 is more pronounced, the fits based on Eq.

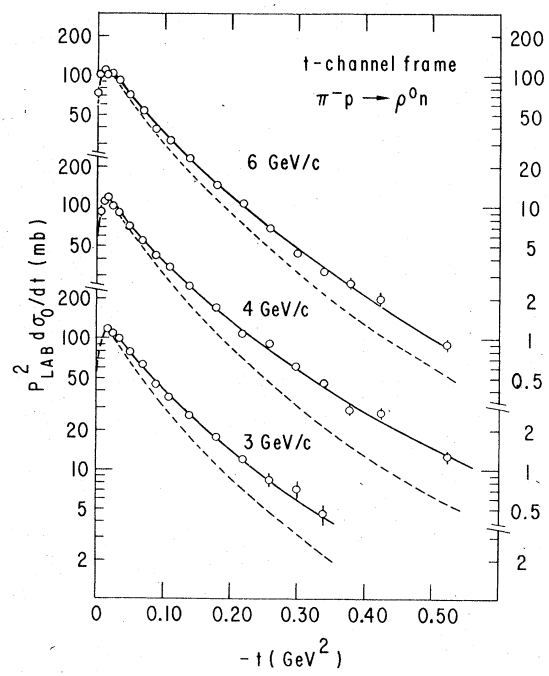

FIG. 15. The P-wave helicity-0 cross sections for ρ^0 production in the t channel. The meaning of the curves is the same as in the previous figure.

(4.2a) are equivalent to the solid curves shown in Fig. 15 over the whole t range.

In the framework of strong-absorption models, as discussed by Kane and Seidl[32] and Field and Sidhu,[49] the s-channel helicity-0 amplitudes should give the cleanest picture of Reggeized π exchange in the process $\pi^- p \to \pi^- \pi^+ n$. The t-channel P_0 amplitude can be affected by strong cuts which occur in s-channel P_- due to both π and A_2 exchanges; on the other hand, the only cuts which contribute to s-channel P_0 are those associated with π exchange. Thus the small shrinkage observed in s-channel P_0 and S may be interpreted in two ways: (1) the π trajectory is nearly flat in the region $-t<0.3$ GeV^2, or (2) the absorptive cuts in P_0 shrink faster with energy than the pole terms, thereby reducing the observed shrinkage of P_0. In either case, the fact that S and P_0 have the same energy and momentum-transfer dependence in the s channel is in agreement with the Kane and Seidl model, which predicts that amplitudes with common exchange and s-channel helicity structure should exhibit the same s and t dependence.

To summarize our observations on the helicity-0 production amplitudes, we have found that (1) the P-wave amplitude extrapolated to $t=\mu^2$ is systematically lower than the WM prediction by 10% at all energies, whereas the S-wave amplitude agrees with theoretical expectations; (2) P_0 and S have similar $p_{\rm lab}$ and t dependence in the s channel, consistent with a nearly flat ($\alpha' = 0.30 \pm 0.04$ GeV^{-2}) pion trajectory for $-t<0.28$ GeV^2; (3) P_0 has a more shallow slope and exhibits more shrinkage in the t channel than in the s channel, in disagreement with the WM assumptions.

C. ρ^0 production in helicity-1 states

The helicity-1 cross sections for ρ^0 production are shown in Figs. 16 to 18, together with the 17-GeV/c cross sections from Ref. 3 (dashed curves) and our parametrization which is discussed below (solid curves). The 17-GeV/c observables are plotted separately in Figs. 19 and 20.

The s-channel unnatural-parity-exchange cross section shown in Fig. 16, $p_{\rm lab}^2\, d\sigma_-/dt$, exhibits a pronounced dip around $-t \approx 0.02$ GeV^2; the cross section falls from $\sigma_- \approx 18$ mb at $t=t_{\rm min}$ (where $\sigma_+ = \sigma_-$) to $\sigma_- < 5$ mb at $t \approx -0.02$ GeV^2. This dip structure is presumably associated with the zero in P_{+-}^- at $t=-\mu^2$ predicted by the WM [Eq. (3.17c)]. However, the dip is more shallow at lower energies than at 17 GeV/c, in apparent contrast with the WM prediction that $|P_-|^2$ vanishes at $t=-\mu^2$ at all energies.

At larger $-t$, both s-channel σ_- and σ_+ exhibit strong energy dependence, whereas the WM am-

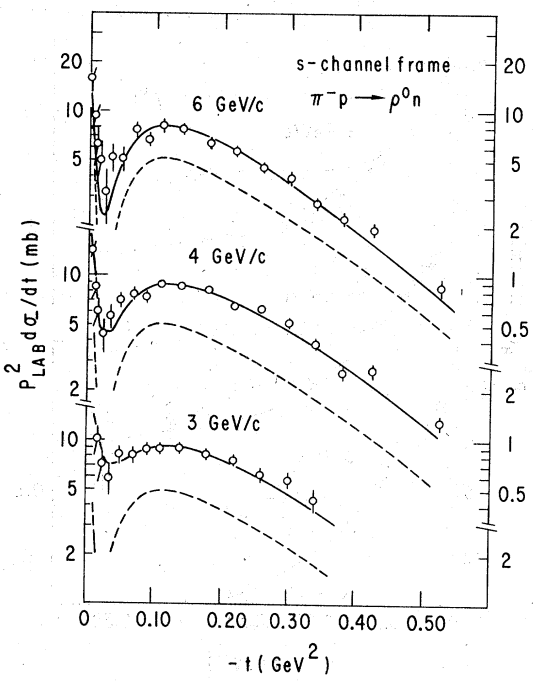

FIG. 16. The P-wave helicity-1 unnatural-parity-exchange cross section for ρ^0 production in the s channel at 3, 4, and 6 GeV/c. The solid curves show the results of the parametrization of the data which is given in Table VII; the dashed curves are a smooth interpolation of the 17-GeV/c ρ^0 production data from Ref. 3.

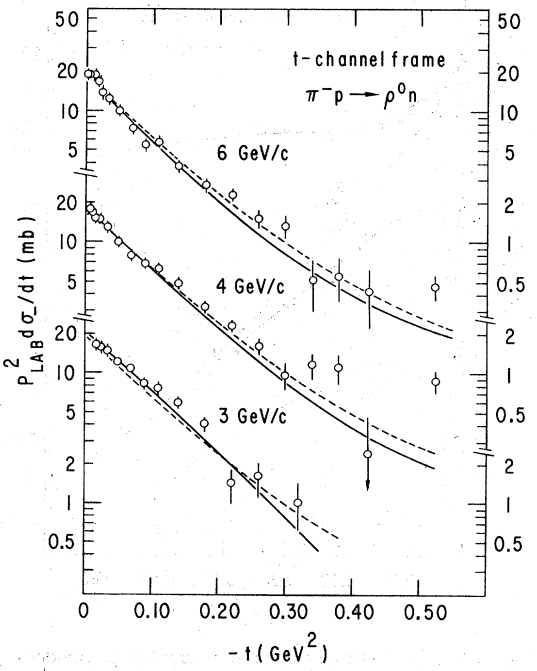

FIG. 17. The P-wave helicity-1 unnatural-parity-exchange cross section for ρ^0 production in the t channel at 3, 4, and 6 GeV/c. The meaning of the curves is the same as in the previous figure.

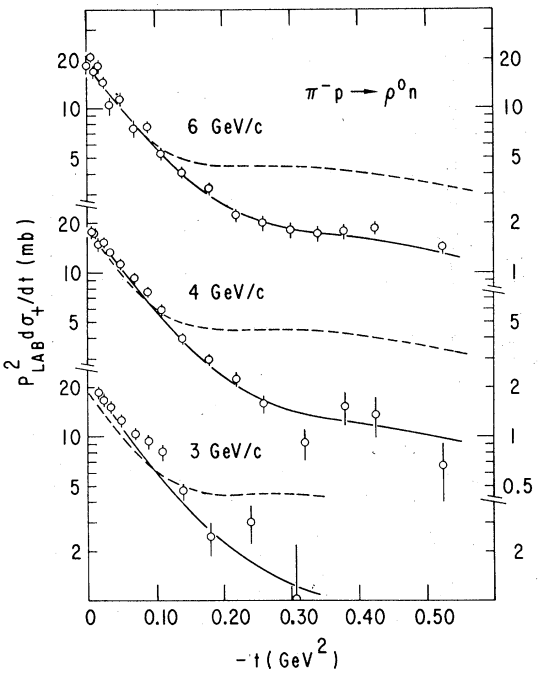

FIG. 18. The P-wave helicity-1 natural-parity-exchange cross section for ρ^0 production at 3, 4, and 6 GeV/c. The meaning of the curves is the same as in the previous two figures.

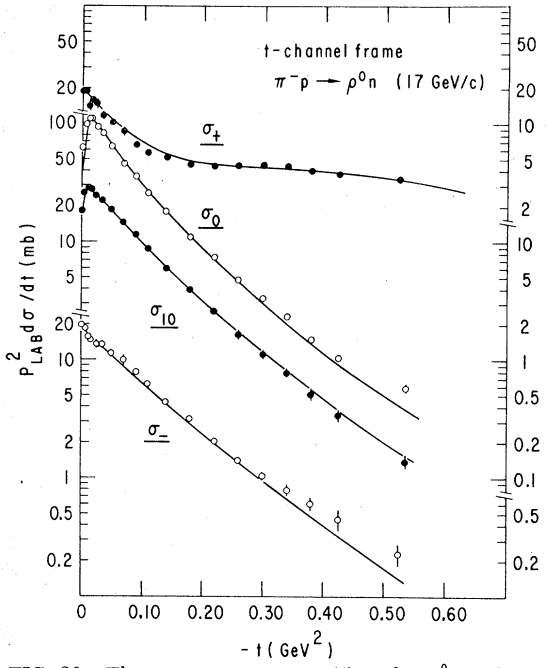

FIG. 20. The P-wave cross sections for ρ^0 production at 17 GeV/c in the t-channel frame. The data are from Ref. 3, and the curves are the result of our fits using the parametrization discussed in the text. The notation $\sigma_{ij} = p_{1ab}{}^2 \rho_{ij} d\sigma/dt$ is used.

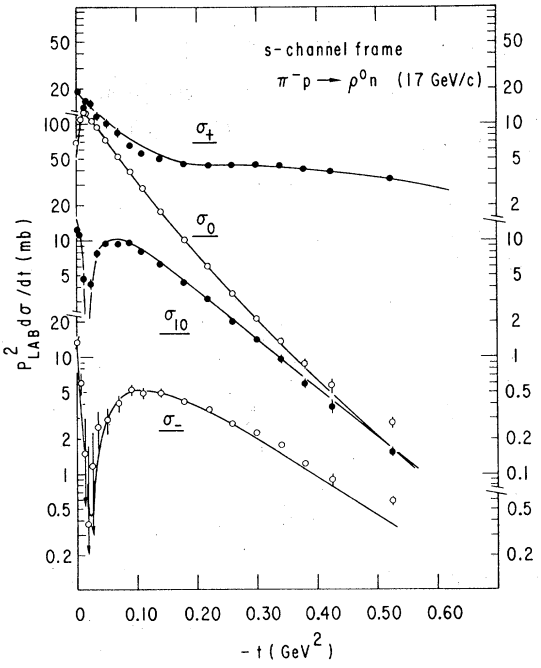

FIG. 19. The P-wave cross sections for ρ^0 production at 17 GeV/c in the s-channel frame. The data are from Ref. 3, and the curves are the result of our fits using the parametrization discussed in the text. The notation $\sigma_{ij} \equiv p_{1ab}{}^2 \rho_{ij} d\sigma/dt$ is used.

plitudes of Eq. (3.17) are independent of energy. For $-t > 0.1$ GeV^2, s-channel σ_- shrinks considerably with increasing energy (Fig. 16); this may be contrasted with the near absence of shrinkage found for s-channel σ_0. The total unnatural-parity cross section $(\sigma_- + \sigma_0)$ is of course frame invariant and shrinks with energy essentially like t-channel σ_0; in the t channel, σ_- (Fig. 17) is nearly independent of energy but is much smaller than σ_0 for all t. The natural-parity cross section, $p_{lab}{}^2\, d\sigma_+/dt$ in Fig. 18, shows dramatic antishrinkage with increasing energy for $-t > 0.1$ GeV^2. This is presumably a manifestation of A_2 exchange, since a pure A_2-exchange cross section with trajectory $\alpha_A(t) > 0$ would increase with energy like $\sigma_+ \propto (p_{lab})^{2\alpha_A(t)}$.

Since the strong energy dependence of $\sigma_\pm$ is inconsistent with the energy-independent WM amplitude structure, it is necessary to modify the WM description of Eq. (3.17). One shortcoming of the Williams model as expressed in Eq. (3.17) is that it is meant to apply only at infinite energies where $t_{min} = 0$. However, it is straightforward to extend the model to lower energies. To do this, we cross the t-channel Born amplitude, P^0_{++}, to the s channel, this time retaining nonleading t_{min}-dependent terms. We add the nonfactorizing $n = 0$ cut as in Eq. (3.18) and the WM collimating fac-

tors, $F_n(t)$, generalized to depend on n as in Ref. 30. Allowing for A_2-exchange flip (A_f) and nonflip (A_n) contributions to P_{+-}, the full set of s-channel amplitudes becomes

$$P^0_{+-}(t) = F_1(t)\frac{(-t')^{1/2}}{\mu^2 - t}\cos\chi(t=\mu^2)\,, \tag{4.7a}$$

$$P^0_{++}(t) = F_0(t)\frac{(-t_{\min})^{1/2}}{\mu^2 - t}\cos\chi(t=\mu^2)\,, \tag{4.7b}$$

$$P^-_{+-}(m,t) \approx \frac{-t'[F_0(t)+F_2(t)]}{m(\mu^2 - t)} - C(m,t)\,, \tag{4.7c}$$

$$P^-_{++}(m,t) \approx 2\frac{(t'\,t_{\min})^{1/2}F_1(t)}{m(\mu^2 - t)}\,, \tag{4.7d}$$

$$P^+_{+-}(m,t) \approx \frac{-t'[F_0(t)-F_2(t)]}{m(\mu^2 - t)} - C(m,t) + A_f(t)\,, \tag{4.7e}$$

$$P^+_{++}(m,t) = A_n(t)\,, \tag{4.7f}$$

where $t' = t - t_{\min}$ and m denotes the ρ^0 or K^* mass. These relations reduce to the WM description of Eq. (3.17) in the limit $t_{\min} = 0$, with the substitutions $F_n(t) = F(t)$, $C(m,t) = F(t)/m$, and $A_{n,f}(t) = 0$.

We now consider in turn (1) the s-channel dip structure σ_- and the associated zero in P^-_{+-}, (2) the energy dependence of σ_+, and (3) the energy dependence of σ_- at large $-t$.

1. Zero structure in P

The variation with energy of the dip structure in s-channel σ_- cannot be attributed to superficial effects such as the $\pi\pi$ S wave, background contamination, or acceptance errors. We argue that the dip in σ_- is filled in at lower energies by the $t_{\min}$-dependent amplitude, P^-_{++}, defined by Eq. (4.7d). To proceed further we make the small $-t$ approximation

$$F_n(t) \approx F(t) \text{ for } -t < 0.1 \text{ GeV}^2 \tag{4.8}$$

in Eq. (4.7). Equations (4.7a) and (4.7b) imply the following relation between P^-_{++} and P^0_{+-}:

$$P^-_{++}(m,t) = 2P^0_{+-}(t)(-t_{\min})^{1/2}/m\,. \tag{4.9}$$

With this relation and the analogous one for P^0_{++}, the contribution of P^-_{++} to the σ_- cross section is easily estimated in terms of the measured quantity σ_0:

$$|P^-_{++}|^2 = 4\,\frac{|t'\,t_{\min}|}{|tm^2|}\,\sigma_0(t)\,. \tag{4.10}$$

Thus the peak value of $|P^-_{++}|^2$ occurs close to that for σ_0 at $-t \approx 0.02$ GeV^2, near the expected WM zero in σ_-, and the magnitude of $|P^-_{++}|^2$ is proportional to $t_{\min}$, which varies like $p_{\text{lab}}{}^{-2}$. Figure 21(a) shows the contributions of $|P^-_{++}|^2$ and $|P^-_{+-}|^2$ to s-channel σ_- at 4 GeV/c; the nonflip contribution neatly fills in the dip in σ_- at 4 GeV/c but, falling like $p_{\text{lab}}{}^{-2}$, would be quite negligible at 17 GeV/c where the dip in the σ_- data is much more pronounced. The solid curves in Figs. 16 and 19 are fits which include $|P^-_{++}|^2$ explicitly, and they describe the data reasonably well in the dip region.

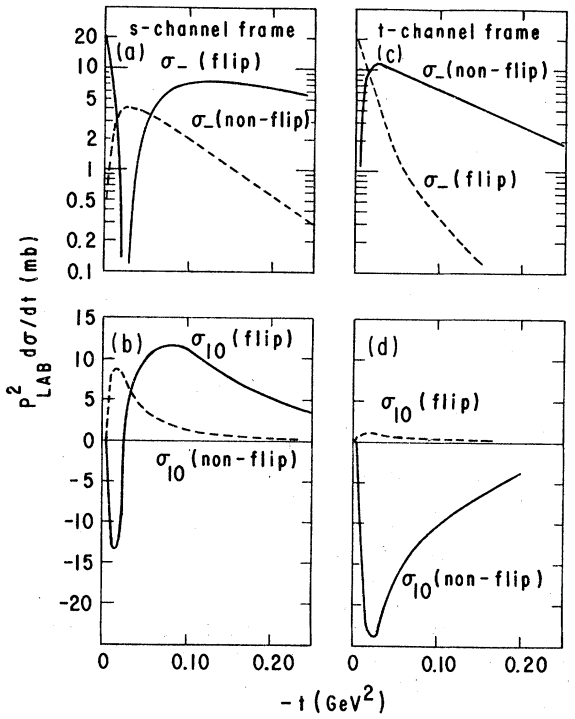

FIG. 21. P-wave cross-section decomposition for helicity-1 ρ^0 production at 4 GeV/c, showing the results of the fits described in the text. The notation $\sigma_{ij} = p_{1\text{ab}}{}^2\rho_{ij}d\sigma/dt$ is used.

The WM zero near $t \approx -\mu^2$ is presumably still present in s-channel P^-_{+-} [Eq. (4.7c)], but its exact location depends somewhat on the cut strength, $C(m,t)$. The most direct way to locate the zero in P^-_{+-} is by means of the interference cross section, $P_{\text{lab}}{}^2\,d\sigma_{10}/dt$. However, here again $t_{\min}$ dependence plays an important role at lower energies. We can expose the nucleon flip and nonflip contributions to σ_{10} as follows:

$$P_{\text{lab}}{}^2\,d\sigma_{10}/dt = \frac{1}{\sqrt{2}}\,\text{Re}(P^{0*}_{+-}P^-_{+-} + P^{0*}_{++}P^-_{++})\,. \tag{4.11}$$

This flip and nonflip σ_{10} cross sections, based on Eq. (4.7), are shown in Fig. 21(b) for 4 GeV/c. The flip part of σ_{10} (solid curve) is essentially independent of p_{lab} and exhibits the WM zero near $t \approx -\mu^2$; the nonflip part (dashed curve) is proportional in strength to $t_{\min}$ and tends to cancel the flip part, thereby moving the zero in σ_{10} to smaller $-t$ at lower energies.

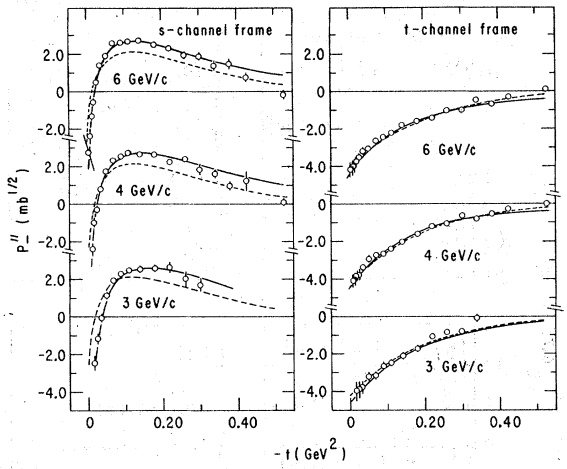

FIG. 22. The real component $P_-^{\parallel}$ of the unnatural-parity-exchange amplitude $P_- = P_-^{\parallel} + iP_-^{\perp}$ for ρ^0 production, derived from our amplitude analysis using the convention that P_0 is purely real. In the s channel, $P_-^{\parallel}$ refers to the dominant flip contribution P_{+-}^{-}; in the t channel, $P_-^{\parallel}$ refers to the quantity $(t/t')^{1/2}P_{++}^{-}$. The solid curves result from fits using the parametrization discussed in the text. The dashed curves are an interpolation of the results of a similar amplitude analysis using the 17-GeV/c data of Ref. 3.

Since both P_{++}^{0} and P_{++}^{-} can be estimated with adequate precision from fits to σ_0 using Eq. (4.7), it is convenient to subtract the nonflip contributions explicitly from s-channel σ_{10}, σ_0, and σ_-. This exposes the pure flip observables for an Estabrooks-Martin type of analysis. The corrected observables can be expressed as

$$p_{\rm lab}^{\,2}\frac{d\sigma_0}{dt}\ (\text{flip}) = (P_{+-}^{0})^2 , \tag{4.12a}$$

$$p_{\rm lab}^{\,2}\frac{d\sigma_-}{dt}\ (\text{flip}) = (P_-^{\parallel})^2 + (P_-^{\perp})^2 , \tag{4.12b}$$

$$p_{\rm lab}^{\,2}\frac{d\sigma_{10}}{dt}\ (\text{flip}) = \frac{1}{\sqrt{2}}\ P_-^{\parallel} P_{+-}^{0} . \tag{4.12c}$$

For convenience, P_{+-}^{0} is taken to be real and positive; P_{+-}^{-} is allowed to have a phase relative to P_{+-}^{0}, namely $P_{+-}^{-} = P_-^{\parallel} + iP_-^{\perp}$. The component $P_-^{\parallel}$ obtained from σ_{10} [Eq. (4.12c)] is plotted at each energy in Fig. 22, together with 17 GeV/c $P_-^{\parallel}$ (dashed curves) and our parametrization (solid curves). In the modified WM parametrization of Eq. (4.7) $P_-^{\perp} = 0$ is assumed, and indeed $|P_-^{\perp}|^2$ as determined from Eq. (4.12) is empirically smaller than $|P_-^{\parallel}|^2$ in the region $-t < 0.5$ GeV^2, shown in Fig. 23. However, $|P_-^{\perp}|^2$ appears to be systematically greater than zero, suggesting the existence of some small phase difference between P_{+-}^{-} and P_{+-}^{0}.[50]

Figure 22 shows considerable energy dependence in s-channel $P_-^{\parallel}$, both in the overall shrinkage of this amplitude in going from 3 to 17 GeV/c and in the movement of the crossover zero to smaller $-t$ as the energy is increased. This latter feature can be easily understood in the framework of the modified WM parametrization of Eq. (4.7c). With the approximation $F_n(t) \approx F(t)$, we can parametrize the $n=0$ cut strength by the definition

$$C(m,t) = C_0(t)F(t)/m , \tag{4.13}$$

where $C_0 = 1$ at all t is the WM prediction from Eq. (3.18). From Eq. (4.7c), the cut strength can be related to the P_{+-}^{-} crossover-zero location, t_c, by the equation

$$t_c = \frac{[2t_{\rm min} - \mu^2 C_0(t_c)]}{[2 - C_0(t_c)]} . \tag{4.14}$$

Thus, with $C_0(t_c) \approx 1$, the P_{+-}^{-} crossover zero is expected to move to smaller $-t_c$ with increasing $p_{\rm lab}$ (decreasing $-t_{\rm min}$); this is the behavior exhibited by the data of Fig. 22. We can solve for $C_0(t_c)$ in terms of the measured crossover-zero locations:

$$C_0(t_c) = 2\,\frac{(t_c - t_{\rm min})}{(t_c - \mu^2)} . \tag{4.15}$$

The experimental values of t_c together with the derived cut strengths, $C_0(t_c)$, are listed in Table VI; the cut strength is consistent with $C_0(t_c) = 0.94$

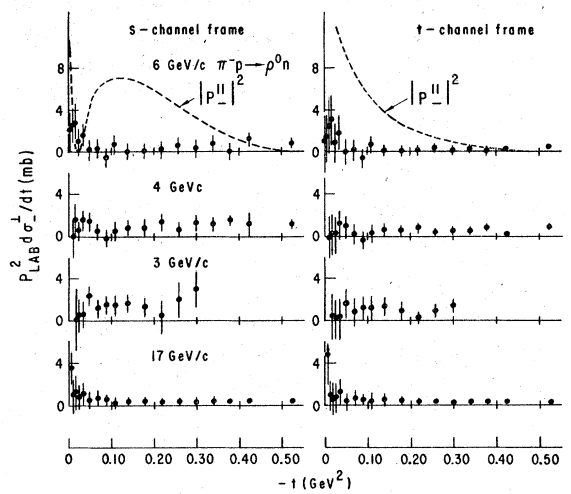

FIG. 23. The contribution to σ_- of $|P_-^{\perp}|^2$, the imaginary component of $P_- = P_-^{\parallel} + iP_-^{\perp}$, for ρ^0 production. In the s channel, $P_-^{\perp}$ refers to the flip amplitude P_{+-}^{-}; in the t channel, $P_-^{\perp}$ refers to the quantity $(t/t')^{1/2}P_{++}^{-}$. The dashed curves show the corresponding contribution from $|P_-^{\parallel}|^2$. The 17-GeV/c points are from our amplitude analysis of the data of Ref. 3.

TABLE VI. Measured values of the crossover-zero locations, t_c, in $P_-^{\parallel}$, together with $t_{\min}$ and cut strength, $C_0(t_c)$, derived from t_c by Eq. (4.15) for the reaction $\pi^- p \to \rho^0 n$.

p_{lab} (GeV/c)	$-t_c$ (GeV^2)	$-t_{\min}$ (GeV^2)	$C_0(t_c)$
3	0.035 ± 0.003	0.0092	0.95 ± 0.05
4	0.027 ± 0.003	0.0052	0.94 ± 0.06
6	0.021 ± 0.002	0.0023	0.92 ± 0.05
17	0.018 ± 0.002	0.0003	0.94 ± 0.05

± 0.05 at all energies, and just slightly weaker than the WM prediction, $C_0 = 1$.

The cut strength can also be derived from the natural-parity cross section, σ_+. Neglecting A_2 exchange and again assuming $F_n(t) = F(t)$, we can obtain $C_0(t_c)$ from σ_+ using the relation

$$\sigma_+(t = t_c) = [C_0(t_c) F(t_c)/m]^2 . \tag{4.16}$$

$C_0(t_c)$ obtained from Eq. (4.16) is found to be independent of energy within errors, and an average value $C_0(t_c) = 1.07 \pm 0.03$ is compatible with all the data. This estimate is somewhat higher than the WM prediction, $C_0 = 1$, or the value obtained from P_{+-}^-, $C_0(t_c) = 0.94 \pm 0.05$. However, we conclude that the cut strength at small $-t$ is very close to the WM prediction, since a value $C_0 \approx 1$ in Eq. (4.13) closely approximates both the P_{+-}^- crossover-zero location and the magnitude of the natural-parity amplitude, $|P_{+-}^+|$. Small deviations from the WM can be accommodated by allowing $C_0(t)$ to vary with t and by relaxing the constraint $F_n(t) = F(t)$. Our main conclusion is that the $t_{\min}$-dependent contributions from the nonflip amplitudes must be taken into account in order to see clearly the structure of the underlying flip amplitude, which has a very simple dependence on energy at small $-t$.

Although the physical absorption corrections are more easily computed in the s channel, the WM amplitudes are in fact simpler in the t channel where small $-t$ zeros are absent. Crossing Eq. (4.7) to the t channel and retaining the approximation $F_n(t) = F(t)$, the t-channel unnatural-parity amplitudes can be represented approximately as follows:

$$P_{++}^0(t) \approx F(t)\sqrt{-t}/(\mu^2 - t) , \tag{4.17a}$$

$$P_{+-}^0(m, t) \approx -\sin\chi \left(\frac{t_{\min}}{t}\right)^{1/2} C(m, t) , \tag{4.17b}$$

$$P_{++}^-(m, t) \approx -\left(\frac{t'}{t}\right)^{1/2} C(m, t) , \tag{4.17c}$$

$$P_{+-}^-(m, t) \approx -\left(\frac{t_{\min}}{t}\right)^{1/2} C(m, t) . \tag{4.17d}$$

Two immediate simplifications are the facts that (1) P_{+-}^0 is very small in the t channel and (2) P_{++}^- and P_{+-}^- stand approximately in the ratio

$$\frac{P_{++}^-(m, t)}{P_{+-}^-(m, t)} \approx \left(\frac{t'}{t_{\min}}\right)^{1/2} . \tag{4.18}$$

The contributions of the flip and nonflip amplitudes to t-channel σ_- and σ_{10} are shown in Fig. 21(c) and Fig. 21(d) for 4 GeV/c. P_{+-}^- is important in σ_- only near the forward direction, where it is required by angular momentum conservation; the flip part of σ_{10} is practically negligible owing to the smallness of P_{+-}^0.

Assuming the simple relation implied by Eq. (4.18), we can express t-channel P_{++}^- and P_{+-}^- in terms of a single amplitude P_-,

$$P_{++}^- = \left(\frac{t'}{t}\right)^{1/2} P_- , \tag{4.19a}$$

$$P_{+-}^- = \left(\frac{t_{\min}}{t}\right)^{1/2} P_- . \tag{4.19b}$$

This has the advantage that (1) P_- is just $C(m, t)$ in the WM and is expected to be independent of energy, and (2) in the forward direction P_- coincides with P_{+-}^- in the s channel. We perform an amplitude analysis in the t channel similar to that in the s channel to obtain the real and imaginary components of P_-, defined by $P_- = P_-^{\parallel} + i P_-^{\perp}$, taking P_{++}^0 to be real by convention. The quantity $P_-^{\parallel}$, shown in Fig. 22, is practically independent of energy in the t channel from 3 to 17 GeV/c. This is consistent with the observation that σ_- is independent of energy in the t channel (Fig. 17), since $\sigma_- = |P_-|^2$. As in the s channel, $|P_-^{\perp}|^2$ (Fig. 23) is small compared with $|P_-^{\parallel}|^2$.

The fits to the unnatural-parity observables shown in Figs. 14 through 20 and Fig. 22 are based on the t-channel parametrization of Eq. (4.17), with $F(t)$ and $C(m, t)$ varied freely; the s-channel amplitudes are obtained by crossing. We have used the constraint $P_-^{\perp} = 0$ in the fits and consequently the fitted curves tend to be slightly low for σ_0 and σ_- and high for σ_{10} and $P_-^{\parallel}$. The exact parametrization and fitted parameters are summarized in Table VII.

2. *Energy dependence of* σ_+

Extrapolated to $t' = 0$, the measured values of $p_{\text{lab}}^2 \, d\sigma_+/dt$ appear to be independent of energy, and the fitted curves shown in Figs. 18 and 19 are based on a constant forward intercept for P_+. This behavior is compatible with the WM, but has important implications for more sophisticated absorption models. For example, the model of Kane

TABLE VII. Parametrization of the ρ^0 production amplitudes together with parameters obtained from fits to the data. The s-channel $P_{-,0}$ amplitudes are obtained by crossing from the t channel using Eqs. (3.9) and (3.11). The fits used data in the range $-t<0.45$ GeV^2 for 4, 6, and 17 GeV/c, and $-t<0.36$ GeV^2 for 3 GeV/c. The quantities denoted by "(avg)" are averages of separate fits to 3-, 4-, 6-, and 17-GeV/c data with errors given by the rms spread. The other quantities are from a combined fit to σ_+ data at all energies. The notation $t' \equiv t - t_{\min}$, μ = the pion mass is used throughout.

$$P^0_{++}(t \text{ chan}) = \frac{\sqrt{-t}}{\mu^2 - t} g_0 e^{[B_0 + 0.7 \ln(p_{\text{lab}}/6)](t-\mu^2)}$$

$$P^-_{++}(t \text{ chan}) = \left(\frac{t'}{t}\right)^{1/2} C_+ e^{[B_- t' + H_-(t')^2]}$$

$$P^0_{+-}(t \text{ chan}) = \sin\chi \left(\frac{t_{\min}}{t'}\right)^{1/2} P^-_{++}(t \text{ chan})$$

$$P^-_{+-}(t \text{ chan}) = \left(\frac{t_{\min}}{t'}\right)^{1/2} P^-_{++}(t \text{ chan})$$

$$P^+_{+-}(s \text{ chan}) = -\{(C_+ e^{B_+ t'})^2 + [g_A t' e^{B_A t'} (p_{\text{lab}}/6)^{\alpha_A}]^2\}^{1/2}$$

$$P^+_{++}(s \text{ chan}) = r_A (-t')^{1/2} g_A e^{B_A t'} (p_{\text{lab}}/6)^{0.5 + t'} [(\tfrac{17}{6})^{\alpha_A}] e^{-i\pi/4}$$

g_0 (avg) $= 3.22 \pm 0.04$ mb$^{1/2}$ GeV	$g_A = 6.77 \pm 0.20$ mb$^{1/2}$ GeV^{-2}
B_0 (avg) $= 2.92 \pm 0.14$ GeV^{-2}	$B_A = 2.44 \pm 0.05$ GeV^{-2}
B_- (avg) $= 5.94 \pm 0.61$ GeV^{-2}	$\alpha_A = 0.56 \pm 0.02$
H_- (avg) $= 2.1 \pm 2.3$ GeV^{-4}	$r_A = 0.25$ GeV (fixed)
$B_+ = 6.78 \pm 0.19$ GeV^{-2}	
$C_+ = 4.39 \pm 0.05$ mb$^{1/2}$	

and Seidl[32] predicts the energy dependence $\sigma_+(t'=0) \propto p_{\text{lab}}^{-0.26}$ in the 4- to 17-GeV/c range.[51] To obtain a constant behavior in $\sigma_+(t'=0)$, the Kane-Seidl model would require important modifications, for example flat trajectories for both π and Pomeron exchange, or dominance of P_+ by the A_2-cut contribution.

For larger $-t$ values ($-t > 0.1$ GeV^2), the antishrinkage observed in $p_{\text{lab}}^2 d\sigma_+/dt$ suggests significant A_2-exchange contributions (see Fig. 18). Indeed, the t dependence of the natural-parity-exchange cross sections suggests the following picture: The region $-t < 0.1$ GeV^2 is dominated by an energy-independent π cut; the region $-t > 0.2$ GeV^2 is strongly influenced by A_2 exchange, especially at higher energies; the region $0.1 < -t < 0.2$ GeV^2 includes possible interference between these mechanisms. The A_2-exchange contribution is expected to be less peripheral than the π-cut contribution for two reasons: First the π-exchange amplitudes are inherently peripheral owing to the proximity of the pion pole, and second, the A_2 pole is expected to contribute most strongly to the double-flip amplitude P^+_{+-}, with the behavior characteristic of an $n=2$ Regge-pole term, $P^+_{+-} \propto t'$, and more weakly to the single-flip amplitude, $P^+_{++} \propto \sqrt{-t}$.[32, 49]

In an analysis which is consistent with this picture, Irving and Michael[37] have parametrized the A_2-exchange contributions to P_+ schematically as follows:

$$P^+_{+-}(m,t) = -C(m,t) - t' C_A(t) e^{-i\pi\alpha_A(t)/2} (p_{\text{lab}}/6)^{\alpha_A(t)}, \tag{4.20a}$$

$$P^+_{++}(m,t) = r_A(-t')^{1/2} C_A(t) e^{-i\pi\alpha_A(t)/2} (p_{\text{lab}}/6)^{\alpha_A(t)}, \tag{4.20b}$$

where $C_A(t) > 0$, $\alpha_A(t) \approx 0.5 + t$, and r_A denotes the A_2-exchange nonflip-to-flip ratio; $r_A \approx 0.25$ to 0.50 GeV.[32, 37, 49] The A_2 pole grows with energy in Regge fashion and is ~135° out of phase with the π-cut contribution, $-C(m,t)$. In the Irving-Michael fits $C(m,t)$ is obtained from small $-t$ σ_+ and falls exponentially with t.

The problem with this parametrization is evident in the Irving-Michael fits to the effective energy dependence and in the analysis by Field and Sidhu,[49] namely around $-t \approx 0.5$ GeV^2, where $\alpha_A(t) \approx 0$, the A_2 pole should be constant with energy, whereas experimentally σ_+ increases like p_{lab} in this region. Extrapolated exponentially from the

small $-t$ region, the π cut is simply too small to influence the energy dependence at $-t \approx 0.5$ GeV^2, even by destructive interference with the A_2 pole. One way to accommodate the energy dependence at large $-t$ is to allow the π-exchange contribution to be nonexponential in its t dependence, thus allowing significant π-A_2 interference at large $-t$; it is also necessary for the π contribution to shrink with energy so that this (destructive) π-A_2 interference is largest at lower energies. A nonexponential dependence of the π contribution to P^+_{+-} can be obtained by allowing weaker absorption in the $n=2$ amplitudes; choosing $F_0(t) < F_2(t)$ in Eq. (4.7e) would be consistent with realistic absorption models as discussed by Kimel and Reya,[30] and would extend the π contribution to larger $-t$ with the correct phase (180°) to interfere destructively with the A_2-exchange term. This picture is in fact consistent with the ρ-ω interference phases as discussed in Sec. VI. At large $-t$ these phases change considerably with energy, suggesting that P^+_{+-} changes from being π-cut dominated at 6 GeV/c to being A_2-pole dominated at 17 GeV/c.

As detailed in Table VII, we have employed a strictly heuristic fit to the σ_+ data in which P^+_{+-} is described by two components: first, an energy-independent π cut which falls exponentially with t to describe the small $-t$ region, and second, a large $-t$ component which contains both A_2-pole and π-cut contributions and which increases smoothly with energy. The two components are added in quadrature since by hypothesis they should interfere only over a limited t range around $-t \approx 0.15$ GeV^2. We have included a single-flip Regge-behaved A_2-exchange amplitude as in Eq. (4.20b), with r_A fixed at 0.25 GeV (r_A here is defined by the ratio of P^+_{++} to the large $-t$ component of P^+_{+-} at 17 GeV/c). The solid curves in Figs. 18 to 20 show the results of the fits; the fit parameters are listed in Table VII.

3. *Energy dependence of σ_- at large $-t$*

At very small $-t$ we have shown that the WM amplitude structure is consistent with $\sigma_\pm$, once $t_{\min}$-dependent effects have been taken into proper account. For $-t > 0.1$ GeV^2, s-channel σ_- (Fig. 16) and P^-_{+-} (Fig. 22) both shrink with energy, a behavior which is not anticipated in the WM. This shrinkage in s-channel P^-_{+-} may be associated with π-exchange Regge behavior, but this explanation seems inadequate in view of the lack of shrinkage seen in s-channel P_0 and S. The behavior of P^-_{+-} could also be explained in terms of an A_2-exchange cut contribution to the $n=0$ amplitude, analogous to the π cut, $C(m,t)$. Given the relative phases of π-cut and A_2-pole contributions in P^+_{+-} [Eq. (4.20)], it follows that an A_2 cut in P^-_{+-} would in fact reinforce the π cut and, by growing with energy, would explain the shrinkage observed in P^-_{+-}.

The parameters listed in Table VII indicate that the WM prediction for the $n=0$ cut strength, $C(m,t) = F(t)/m$ in Eq. (3.18), is valid only near $t=0$. With the WM approximation, $F_n(t) = F(t)$ in Eq. (4.7), the t dependence of $F(t)$ would be given by the slope parameter B_0, namely $B_0 \approx 3$ GeV^{-2} (t channel) and $B_0 \approx 4$ GeV^{-2} (s channel). On the other hand, the t dependence of $C(m,t)$ is given by the slope parameters $B_\pm$ [see Eq. (3.19)]; from Table VII, $B_+ \approx 6.8$ GeV^{-2} and $B_- \approx 5.9$ GeV^{-2}. Thus, the fits indicate that $C(m,t) < F(t)/m$ away from $t=0$.

Nevertheless, the 15- and 17-GeV/c dipion data appear to provide strong support for the WM over the range $-t < 0.2$ GeV^2.[2,3] In particular, the WM assumption, $C(m,t) = F(t)/m$, leads directly to the

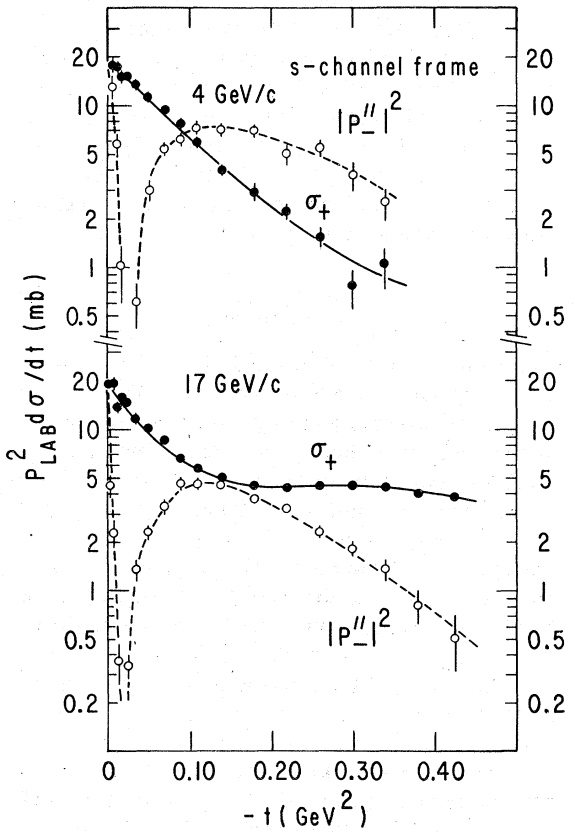

FIG. 24. Comparison of the helicity-1 ρ^0-production natural- and unnatural-parity-exchange cross sections in the s channel at 4 and 17 GeV/c. The unnatural-parity cross section has been determined from the amplitude analysis in order to test the WM prediction $|P^-_{+-}|^2 \leq |P^+_{+-}|^2$, where $\sigma_+ \approx |P^+_{+-}|^2$ is assumed. The curves shown are smooth interpolations.

prediction that

$$|P^-_{+-}|^2 \leq |P^+_{+-}|^2 \tag{4.21}$$

in the s channel, where the equality is meant to hold at large $-t$. Since $P^{\pm}_{+-}$ depend strongly on energy, it is valuable to examine the WM prediction at the lower energies, where the A_2-exchange contribution is smaller. Figure 24 compares the two relevant quantities σ_+ and $|P^{\parallel}_-|^2$ from the amplitude analysis ($|P^{\parallel}_-|^2 \approx |P^-_{+-}|^2$), at both 4 and 17 GeV/$c$. The 17-GeV/$c$ data indeed satisfy the WM prediction of Eq. (4.21) at all t, although for $-t > 0.2$ GeV^2 A_2 exchange enhances σ_+. On the other hand, the 4-GeV/c data do not satisfy the WM prediction; rather, for $-t > 0.1$ GeV^2, $|P^{\parallel}_-|^2 > \sigma_+$. We conclude that the apparent success of the WM at higher energies and large $-t$ is fortuitous: P^-_{+-} decreases with energy while P^+_{+-} increases with energy, so that these amplitudes happen to be equal in magnitude at 15 and 17 GeV/c over a limited t range near $-t \approx 0.15$ GeV^2. At 4 GeV/c, where the amplitudes should reflect more faithfully the π-exchange behavior, the observation that $|P^-_{+-}| > |P^+_{+-}|$ at large $-t$ implies a weaker absorption strength than predicted by the WM. Thus, the simplest explanation of the comparison made in Fig. 24 is that the $n=0$ cut strength falls faster with t than given by the WM resulting in $\sigma_- > \sigma_+$ at larger $-t$; at higher energies, A_2 exchange accidentally helps restore the WM inequality of Eq. (4.21).

D. Summary

In Table V we have presented the corrected ρ and K^* production cross sections. We find that the unnatural-parity-exchange ρ production cross section exhibits shrinkage, but the individual projections behave differently: σ_- accounts for most of the shrinkage in the s channel, while σ_0 accounts for the shrinkage in the t channel. The energy dependence of s-channel σ_- is explained partly by nonasymptotic $t_{\min}$-dependent contributions, and partly by genuine shrinkage in the double-flip amplitude, which may in turn be related to A_2-exchange cuts which grow with energy. The small shrinkage in s-channel σ_0 and in the S-wave cross section suggests that the π trajectory is fairly flat, or else that the Regge behavior of the pion is obscured by absorptive effects in the $n=1$ amplitudes. The large $-t$ behavior of s-channel σ_- and σ_+ precludes simple absorption prescriptions such as the Williams model or the Irving-Michael analysis. We have provided a heuristic parametrization for the ρ-production amplitudes in Table VII in order to provide a framework for the study of SU(3) phenomenology in Sec. VI.

V. ρ-ω INTERFERENCE EFFECTS

The fits to the $\pi^+\pi^-$ mass spectra described in Sec. III included only the ρ^0 in the $\pi\pi$ P wave, and were designed to describe the average of the spectra for $\pi^- p$ [reaction (1.1)] and $\pi^+ n$ [reaction (1.2)] initial states away from the ω region. In order to determine the ρ-ω interference parameters, we essentially fitted the difference of the cross sections for $\pi^+ n$ and $\pi^- p$ initial states, this time including the ω region and fixing the parameters obtained from the previous mass-spectrum fits. The spectra for π^+ and π^- incident were analyzed simultaneously in 16 sets of fits, each defined by incident energy, momentum-transfer cut, and s- or t-channel reference frame.

Analysis of ρ-ω interference in this experiment has been reported in a previous publication.[1] We have now extended this analysis to include t-channel as well as s-channel observables and also to describe the interference dme ρ_{10}. In addition we employ the S-wave parameterization of Sec. III instead of the polynomial fit to the ρ_{SS} background used in Ref. 1; the results of the two analyses are completely consistent. A somewhat different approach, the Estabrooks-Martin amplitude analysis of ρ-ω interference at 17 GeV/c, is described in Ref. 4. For a review of ρ-ω interference phenomenology, we refer the reader to Ref. 52. In this section we first describe the parameterization and fitting procedure and then discuss the physics results.

A. Parametrization of ρ-ω interference

First we review the assumptions used in the present analysis. Diagrams for dipion production are shown in Fig. 25. The amplitudes contain terms of order $0, 1, 2, \ldots$ in the $\langle\omega|\rho\rangle$ matrix element. We ignore any direct $\omega \to \pi^+\pi^-$ decay that does not proceed through the ρ intermediate state, and assume therefore that the $\omega \to \pi^+\pi^-$ decay phase is given by the phase of the ρ propagator at the ω mass. Thus, the $\langle\omega|\rho\rangle$ matrix element is taken to be purely real, consistent with the results of e^+e^-

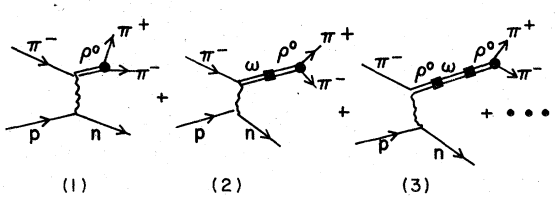

FIG. 25. Diagrams for dipion production containing terms of order 0, 1, and 2 in the $\langle\omega|\rho\rangle$ matrix element. Contributions from the direct decay $\omega \to \pi^+\pi^-$ are ignored.

annihilation and photoproduction experiments.[52] Experimental consequences of a possible direct $\omega \to \pi^+\pi^-$ decay amplitude have been discussed by Rabl and Reay.[53] We note that the parameterization which we obtain from the diagrams of Fig. 25 is identical with that derived by the mass-matrix approach described in Ref. 54.

By squaring the amplitude depicted in Fig. 25, we obtain the following expansion for the P-wave $\pi\pi$ cross section in a given helicity state:

$$p_{1ab}{}^2 \frac{d^2\sigma_M}{dtdm} = N_\rho{}^{-1} |B_\rho(m)|^2 |P_M(\rho)|^2 \left(1 \pm 2\epsilon \frac{\mathrm{Re}\,[P_M(\rho)^* P_M(\omega) B_\omega(m)]}{|P_M(\rho)|^2}\right)$$
$$+ N_\omega{}^{-1} |B_\omega(m)|^2 |P_M(\omega)|^2 R \left(1 - 2\frac{\Gamma_\omega}{\Gamma_\rho} \frac{|P_M(\rho)|^2}{|P_M(\omega)|^2}\right) + \cdots . \quad (5.1)$$

The + (−) sign refers to the $\pi^- p$ ($\pi^+ n$) initial state and is just the relative sign of diagram (2) in Fig. 25. The amplitudes $P_M(\rho)$ and $P_M(\omega)$ are the ρ^0 and ω production amplitudes for helicity-M states. These amplitudes were defined in Sec. III and normalized as in Eq. (3.8); as before, nucleon-helicity indices are suppressed except as needed. The other factors in Eq. (5.1) are defined as follows:

$$\epsilon = 2m_\omega \langle \omega | \rho \rangle , \quad (5.2)$$

$$R = \frac{\Gamma(\omega \to \pi^+\pi^-)}{\Gamma(\omega \to \mathrm{all})}$$
$$= \frac{\epsilon^2}{[(m_\omega m_\rho \Gamma_\omega(m_\omega)\Gamma_\rho(m_\omega)]} , \quad (5.3)$$

$$B_\rho(m) = [(m_\rho{}^2 - m^2 - i m_\rho \Gamma_\rho(m)]^{-1} , \quad (5.4)$$

$$B_\omega(m) = [(m_\omega{}^2 - m^2 - i m_\omega \Gamma_\omega(m)]^{-1} , \quad (5.5)$$

$$N_{\rho,\omega} = \int_0^\infty |B_{\rho,\omega}(m)|^2 dm . \quad (5.6)$$

The mass mixing term $\langle \omega | \rho \rangle$ is equal to the parameter δ defined by Goldhaber, Fox, and Quigg[54]; Coleman and Glashow[55] have predicted $\delta \approx 2.5$ MeV. Our ϵ is not the same as the dimensionless ϵ used in other analyses.[52] Numerically, a 1% $\omega \to \pi^+\pi^-$ branching ratio R corresponds to $\epsilon = 0.0030$ GeV^2 and $\delta = 1.92$ MeV.

We first remark on the term proportional to R in Eq. (5.1), since we will ignore it and higher-order terms in subsequent fits to the data. This term has the same sign for both $\pi^+ n$ and $\pi^- p$ initial states and would show up as an ω Breit-Wigner peak or dip in the sum of the two spectra. Figure 25 allows two contributions to this term, one coming from the square of diagram (2) and the other from the interference of diagrams (1) and (3). The former term is just the cross section for ω production followed by ω decay into $\pi^+\pi^-$. Averaged over the ω band this term gives a positive enhancement in the cross section of as much as 10% at large $-t$, where the ratio $|P_M(\omega)|^2/|P_M(\rho)|^2$ is maximum. Unfortunately this enhancement is large only where the cross section and the statistics are small. At best this term can be used to give an upper limit on R and we will ignore it in subsequent fits. The second term of order ϵ^2, caused by the interference of diagrams (1) and (3) in Fig. 25, is proportional to $|P_M(\rho)|^2$ and consequently produces a dip in all dipion cross sections at the ω mass; the magnitude of this dip is a fixed fraction of the dipion cross section given approximately by twice

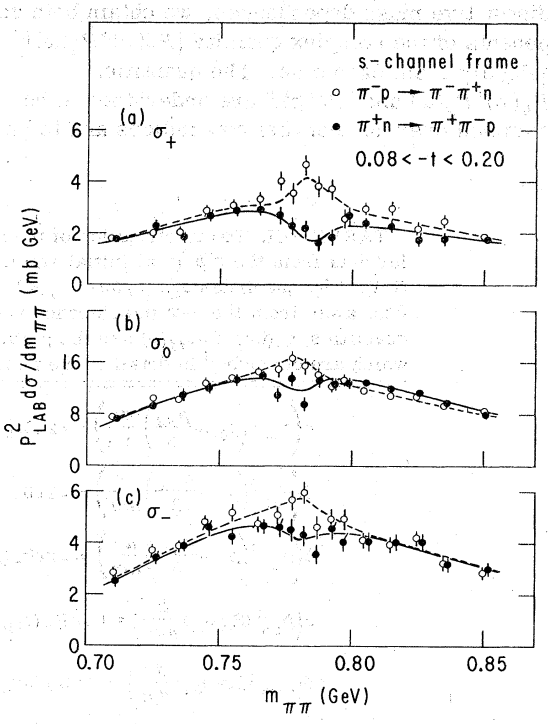

FIG. 26. Comparison of the dipion mass spectra in the ρ-ω interference region for the s-channel projections of σ_0, σ_+, and σ_-, where $\sigma_{ij} = p_{1ab}{}^2 \rho_{ij} d\sigma/dm$ is plotted. The data are from reactions (1.1) (open points and dashed curves) and (1.2) (solid points and solid curves) at 4 GeV/c and $0.08 < -t < 0.20$ GeV^2. The curves result from the fits described in the text, and are used to determine the relative phases and magnitudes of the ρ^0 and ω production amplitudes.

the ω branching ratio R. Since R is small empirically ($R \approx 0.01$), this term is undetectable in the present data.

The ρ-ω interference term which is linear in ϵ in Eq. (5.1) can be directly measured, since it produces a difference between the cross sections for $\pi^+ n$ and $\pi^- p$ initial states at the ω mass. Figure 26 shows a comparison of these mass spectra at 4 GeV/c, and $0.08 < -t < 0.20$ GeV^2, for the s-channel projections σ_0, σ_+, and σ_-. Clear interference effects can be seen, with the incident π^+ and π^- cross sections dramatically different in the vicinity of the ω. The fitted curves determine the relative phases and magnitudes of $P_M(\rho)$ and $P_M(\omega)$ in Eq. (5.1).

The interference term in Eq. (5.1) gives a mass-dependent contribution to each of the P-wave cross sections of the form

$$\delta\left(p_{\rm lab}{}^2\rho_M \frac{d^2\sigma}{dm\,dt}\right) = \pm 2\epsilon\tilde{\sigma}_M |f_P(m)|^2 \left(\frac{\mathrm{Re}[P_M(\rho)^* P_M(\omega)]}{|P_M(\rho)|^2}\,\mathrm{Re}B_\omega(m) - \frac{\mathrm{Im}[P_M(\rho)^* P_M(\omega)]}{|P_M(\rho)|^2}\,\mathrm{Im}B_\omega(m)\right), \tag{5.7}$$

where the signs + (−) refer to $\pi^- p$ ($\pi^+ n$) initial states and where the factor $\tilde{\sigma}_M |f_P(m)|^2$ from Table II gives the intensity for helicity-M ρ^0 production in the absence of ρ-ω interference. A similar expression was used for ρ-ω interference effects in ρ_{10}, which will be treated in detail below. The precise formulas used in the fits are given in Table VIII. Since the two components of the ω Breit-Wigner form, $\mathrm{Re}B_\omega(m)$ and $\mathrm{Im}B_\omega(m)$ in Eq. (5.7), have distinctive mass dependences, we obtain both components of the complex quantity $[P_M(\rho)^* P_M(\omega)]/|P_M(\rho)|^2$ from each dme. The quantities $P_M(\rho)^* P_M(\omega)$ and $|P_M(\rho)|^2$ are understood to be summed over nucleon-helicity indices and to be averaged over each (fairly coarse) t bin. Since the parameter ϵ in Eq. (5.7) is not *a priori* known, it is convenient to express these interference quantities in terms of a phase ϕ_M and a magnitude $|\sigma_M(\mathrm{int})|$:

$$\phi_M = \tan^{-1}\frac{\mathrm{Im}[P_M(\rho)^* P_M(\omega)]}{\mathrm{Re}[P_M(\rho)^* P_M(\omega)]}, \tag{5.8a}$$

$$\frac{|\sigma_M(\mathrm{int})|}{|\sigma_M(\rho)|} = \left(\frac{\epsilon}{0.0030}\right)\frac{|P_M(\rho)^* P_M(\omega)|}{|P_M(\rho)|^2}. \tag{5.8b}$$

The results of the fits, which are the quantities on the left-hand side of Eq. (5.8), are listed in Table IX. The ratios of cross-section magnitudes in Eq.

TABLE VIII. Parametrization of the ρ-ω interference observables. The + (−) sign is used for data from the $\pi^- p$ ($\pi^+ n$) initial state. The fits used data in the interval $0.64 < m_{\pi\pi} < 0.94$ GeV. The quantities $\tilde{\sigma}_{ij}$, $f_P(m)$, $f_S(m)$, and a_{ij} were taken from the Sec. III mass-spectrum fits, away from the ρ-ω interference region, and are defined in Tables I and II. The complex quantities $\sigma_{ij}(\mathrm{int})/\mathrm{Re}\sigma_{ij}(\rho)$ are the parameters to be determined by the ρ-ω interference fits, which are described in detail in the text.

$$\delta\left(p_{\rm lab}{}^2\left(\rho_{00} + \frac{\rho_{SS}}{3}\right)\frac{d\sigma}{dm}\right) = \pm 2\,\epsilon\tilde{\sigma}_0 |f_P(m)|^2 \Delta_0(m)$$

$$\delta\left(p_{\rm lab}{}^2\left(\rho_{+} + \frac{\rho_{SS}}{3}\right)\frac{d\sigma}{dm}\right) = \pm 2\,\epsilon\tilde{\sigma}_+ |f_P(m)|^2 \Delta_+(m)\left[1 + \tfrac{1}{2}a_+\frac{(m_R - m)}{m}\right]$$

$$\delta\left(p_{\rm lab}{}^2\left(\rho_{-} + \frac{\rho_{SS}}{3}\right)\frac{d\sigma}{dm}\right) = \pm 2\,\epsilon\tilde{\sigma}_- |f_P(m)|^2 \Delta_-(m)\left[1 + \tfrac{1}{2}a_-\frac{(m_R - m)}{m}\right]$$

$$\delta\left(p_{\rm lab}{}^2(\mathrm{Re}\,\rho_{10})\frac{d\sigma}{dm}\right) = \pm 2\,\epsilon\,\mathrm{Re}(\tilde{\sigma}_{10})\frac{|f_P(m)|^2}{\sqrt{2}}\Delta_{10}(m)\left[1 + a_{10}\frac{(m_R - m)}{m}\right]$$

$$\delta\left(p_{\rm lab}{}^2(\mathrm{Re}\,\rho_{0S})\frac{d\sigma}{dm}\right) = \pm\,\epsilon\tilde{\sigma}_{0S}\,\mathrm{Re}[f_S^*(m) f_P(m)]\Delta_{0S}(m)$$

$$\delta\left(p_{\rm lab}{}^2(\mathrm{Re}\,\rho_{1S})\frac{d\sigma}{dm}\right) = \pm\,\epsilon\,\mathrm{Re}(\tilde{\sigma}_{1S})\frac{\mathrm{Re}[f_S^*(m) f_P(m)]}{\sqrt{2}}\Delta_{1S}\left[1 + a_{10}\frac{(m_R - m)}{m}\right]$$

where $\Delta_{ij}(m) = \dfrac{\mathrm{Re}\sigma_{ij}(\mathrm{int})}{\mathrm{Re}\sigma_{ij}(\rho)}\mathrm{Re}B_\omega(m) - \dfrac{\mathrm{Im}\sigma_{ij}(\mathrm{int})}{\mathrm{Re}\sigma_{ij}(\rho)}\mathrm{Im}B_\omega(m)$

$B_\omega(m) = [m_\omega^2 - m^2 - i\,m_\omega\,\Gamma_\omega(q/q_\omega)^3]^{-1}$

q_ω = the center-of-mass momentum of the $\pi^+\pi^-$ system at $m_{\pi\pi} = m_\omega$

TABLE IX. Values of the ρ-ω interference parameters obtained from fits to each $\pi\pi$ density-matrix element projection using the representation given in Table VIII and Eq. (5.8). The values of $|\sigma_M(\text{int})|/|\sigma_M(\rho)|$ are normalized to be equal to the ratio of amplitudes $|P_M(\rho)^* P_M(\omega)|/|P_M(\rho)|^2$ for an $\omega \to \pi^+\pi^-$ branching ratio $R = 0.01$. The phases φ are given in degrees. The ±1.5-MeV absolute mass-scale uncertainty corresponds to an uncertainty in the phases of ±9°, which is not included in the table.

p_{lab} (GeV/c)	$-t$ (GeV^2)	t-channel frame							s-channel frame						
		$\frac{\lvert\sigma_+(\text{int})\rvert}{\lvert\sigma_+(\rho)\rvert}$	φ_+	$\frac{\lvert\sigma_0(\text{int})\rvert}{\lvert\sigma_0(\rho)\rvert}$	φ_0	$\frac{\lvert\sigma_-(\text{int})\rvert}{\lvert\sigma_-(\rho)\rvert}$	φ_-	$\frac{\lvert\sigma_{10}(\text{int})\rvert}{\lvert\sigma_{10}(\rho)\rvert}$	φ_{10}	$\frac{\lvert\sigma_0(\text{int})\rvert}{\lvert\sigma_0(\rho)\rvert}$	φ_0	$\frac{\lvert\sigma_-(\text{int})\rvert}{\lvert\sigma_-(\rho)\rvert}$	φ_-	$\frac{\lvert\sigma_{10}(\text{int})\rvert}{\lvert\sigma_{10}(\rho)\rvert}$	φ_{10}
3	0.0–0.08	0.45 ± 0.16	237 ± 20	0.26 ± 0.06	315 ± 15	0.18 ± 0.16	25 ± 47	0.29 ± 0.12	3 ± 22	0.24 ± 0.07	312 ± 17	0.25 ± 0.22	316 ± 53	0.35 ± 0.19	281 ± 33
3	0.08–0.20	0.83 ± 0.27	244 ± 19	0.20 ± 0.09	284 ± 27	0.57 ± 0.19	236 ± 19	0.29 ± 0.14	269 ± 29	0.20 ± 0.11	250 ± 30	0.34 ± 0.14	284 ± 27	0.25 ± 0.11	303 ± 28
4	0.0–0.08	0.34 ± 0.09	258 ± 16	0.15 ± 0.04	310 ± 16	0.20 ± 0.09	341 ± 26	0.17 ± 0.06	331 ± 21	0.14 ± 0.04	318 ± 18	0.14 ± 0.14	276 ± 63	0.10 ± 0.11	260 ± 67
4	0.08–0.20	0.90 ± 0.14	251 ± 9	0.32 ± 0.05	300 ± 9	0.21 ± 0.11	290 ± 32	0.39 ± 0.08	310 ± 11	0.38 ± 0.06	300 ± 9	0.28 ± 0.08	280 ± 18	0.37 ± 0.06	304 ± 10
4	0.20–0.40	1.67 ± 0.35	198 ± 11	0.50 ± 0.09	274 ± 11	0.65 ± 0.21	273 ± 20	0.80 ± 0.17	288 ± 13	0.78 ± 0.17	267 ± 12	0.37 ± 0.11	280 ± 17	0.68 ± 0.13	280 ± 11
6	0.0–0.08	0.40 ± 0.14	239 ± 19	0.11 ± 0.06	282 ± 31	0.24 ± 0.13	17 ± 27	0.30 ± 0.08	308 ± 16	0.19 ± 0.06	274 ± 21	0.42 ± 0.26	75 ± 38	0.26 ± 0.19	191 ± 37
6	0.08–0.20	0.94 ± 0.19	221 ± 10	0.34 ± 0.08	281 ± 15	0.22 ± 0.18	30 ± 44	0.41 ± 0.12	305 ± 18	0.26 ± 0.10	314 ± 23	0.36 ± 0.13	258 ± 22	0.36 ± 0.10	293 ± 16
6	0.20–0.40	1.16 ± 0.23	193 ± 10	0.37 ± 0.13	233 ± 20	0.63 ± 0.33	5 ± 29	0.48 ± 0.22	324 ± 28	0.44 ± 0.24	326 ± 32	0.56 ± 0.17	238 ± 16	0.40 ± 0.17	284 ± 25

(5.8b) are defined so as to coincide with the amplitude ratio, $|P_M(\rho)^* P_M(\omega)|/|P_M(\rho)|^2$, for an $\omega \to \pi^+\pi^-$ branching ratio $R = 0.01 (\epsilon = 0.0030$ GeV$^2)$. Equation (5.8) will be generalized below to treat the ρ_{10} data.

Before examining the fit results, we remark further on some details of the fitting procedure. (1) The factors $a_\pm$, which give the mass dependence of $P_\pm$, are taken to be half as large in the ρ-ω interference expressions of Table VIII as in the ρ^0-intensity formulas of Table II; this is because the ρ^0-production amplitudes enter only linearly in the ρ-ω interference corrections. (2) Appropriate S-ω interference terms have been added to ρ_{0S} and ρ_{1S} in Table VIII; we have dropped terms in the expansion proportional to $\sin(\delta_S - \delta_P)$, which is small at the ω mass. The resulting S-ω interference parameters are poorly determined but are consistent with the assumption of Eq. (4.2) that the production amplitudes S and P_0 are relatively real and spin coherent. We will not use these S-ω interference data for further analysis because, within their large errors, they contain no new information. (3) We have folded the experimental $\pi\pi$ mass resolution into the ρ-ω interference parametrization before fitting the data. (4) We have fixed the ω mass to $m_\omega = 0.7827$ GeV and have allowed Γ_ω to vary over a restricted range, resulting in $9.5 < \Gamma_\omega < 10.5$ MeV. (5) The systematic uncertainty in our mass calibration (±1.5 MeV) translates into a common systematic uncertainty of ±9° in the ρ-ω interference phases, which is not included in the uncertainties of Table IX. (6) To account for possible normalization differences between $\pi^- p$ and $\pi^+ n$ initial states, we have included in the fits to each dme a free normalization parameter; the fits indicated agreement in the relative normalization typically within 6%, and showed that the ρ-ω interference parameters are insensitive to these normalization corrections. Note that the curves shown in Fig. 26 include these corrections; consequently the interference contributions cannot be deduced directly by taking differences of the $\pi^- p$ and $\pi^+ n$ fitted curves shown.

The total χ^2/degree of freedom for the s-channel fits was 2147/1752; however, no systematic discrepancies could be discerned in the fits, and the errors in Table IX have not been enlarged over the statistical errors.

B. Results of the ρ-ω interference fits

The interpretation of the ρ-ω interference measurements is straightforward if the ρ^0-production amplitudes have the simple nucleon-helicity structure assumed in Sec. IV. Assuming that the ρ^0 amplitudes are dominated by s-channel helicity-flip

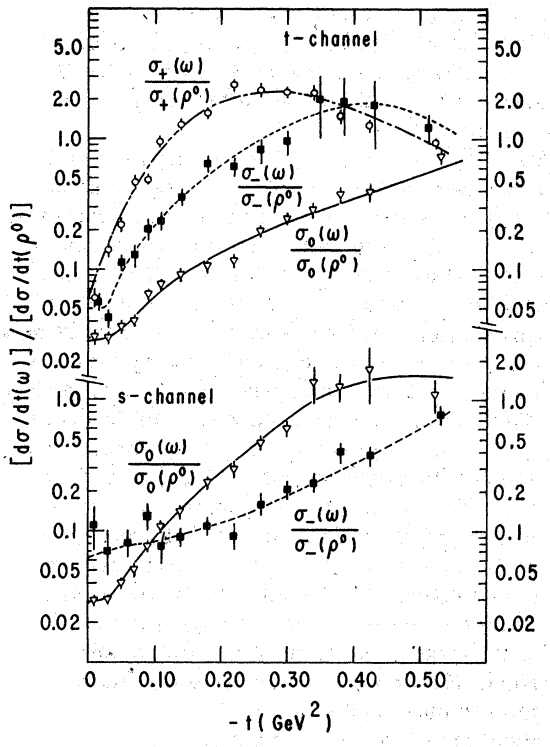

FIG. 27. Ratios of ω to ρ^0 production cross-section components σ_0 (open triangles and solid curves), σ_+ (open circles and dot-dashed curves), and σ_- (solid squares and dashed curves), where $\sigma_{ij}=p_{1ab}{}^2\rho_{ij}d\sigma/dt$. The curves are smooth interpolations of the data, which are all at 6 GeV/c. We have used the ω-production data from Ref. 9, corrected for ρ-ω interference, for these ratios.

π and A_2 exchanges, the ρ-ω interference parameters pick out those ω-production amplitudes that are coherent in spin with the ρ^0 amplitudes, for example s-channel helicity-flip B and ρ exchanges. The parameters of Table IX then measure directly the relative phases and magnitudes of the spin-coherent amplitudes in the two reactions; the magnitude ratios reduce to $|\sigma_M(\text{int})|/|\sigma_M(\rho)|=|P_M(\omega)|/|P_M(\rho)|$, and the phases become $\phi_M=\arg[P_M(\omega)]-\arg[P_M(\rho)]$, where $P_M(\omega)$ and $P_M(\rho)$ refer to the π^--induced reactions, and σ_M includes $\sigma_{+,-,0}$ (the interpretation of σ_{10} is more complicated). We emphasize that if the nucleon-helicity structure of ρ^0 production were very different (e.g., significant A_1 exchange), then the interference parameters would require a more complicated interpretation.

If ω production is itself dominated by the B- and ρ-exchange amplitudes that contribute to the interference, then we would expect the strength of the measured interference to be given by the square root of the ω-to-ρ^0 cross-section ratio,

$$|P_M(\omega)|/|P_M(\rho)|=[\sigma_M(\omega)/\sigma_M(\rho)]^{1/2}.$$

We note that Irving[56] has argued that this is not the case, and that nonflip "Z" exchange (the $J^{PC}=2^{--}$ analog of the A_1) dominates unnatural-parity ω production for $-t<0.4$ GeV^2; Z exchange would contribute to the ω cross section but not to the ρ-ω interference unless A_1 exchange were important in ρ^0 production. Cross-section ratios are shown in Fig. 27, where the ω-production data of Ref. 9 are used. These ratios span a considerable dynamic range, from $\sigma_0(\omega)/\sigma_0(\rho)\approx 0.03$ at small $-t$ to $\sigma_+(\omega)/\sigma_+(\rho)\approx 2.0$ at large $-t$. Thus, neglecting Z exchange, the cross-section ratios suggest that we should find larger ρ-ω interference effects in σ_+ than in $\sigma_{0,-}$, and that the interference should increase with $-t$. The smallest effects should be seen in s-channel σ_- and t-channel σ_0; helicity-0 ω's are enhanced in the s channel while helicity-0 ρ's are more prominent in the t channel. These features are qualitatively consistent with the parameters in Table IX, and the enhanced interference effect in σ_+ can be seen directly in Fig. 26.

Next we summarize some more detailed results, namely the interpretation of interference in σ_{10}, the ω branching ratio, and the effect of interference on the ω production cross sections.

ρ-ω interference in σ_{10}. The complex interference quantity obtained from the fits to σ_{10} can be expressed as

$$\frac{\sigma_{10}(\text{int})}{\text{Re}\sigma_{10}(\rho)}=\left(\frac{\epsilon}{0.0030}\right)\frac{[P_-(\rho)^*P_0(\omega)+P_0(\rho)^*P_-(\omega)]}{2\,\text{Re}[P_-(\rho)^*P_0(\rho)]}, \tag{5.9}$$

which is the generalization of Eq. (5.8) for the P-wave interference dme ρ_{10}. The measured phase and magnitude of the quantity on the left-hand side of Eq. (5.9) are given in Table IX. In the limit that $P_-(\rho)$ and $P_0(\rho)$ are spin coherent (away from $t\approx t_{\min}$) and have the same phase, Eq. (5.9) simplifies to the following relation, independent of the nature of $P_M(\omega)$:

$$\frac{\sigma_{10}(\text{int})}{\text{Re}\sigma_{10}(\rho)}=\frac{1}{2}\left[\frac{\sigma_0(\text{int})}{\sigma_0(\rho)}+\frac{\sigma_-(\text{int})}{\sigma_-(\rho)}\right]. \tag{5.10}$$

The quantities on the right-hand side of Eq. (5.10) are of course independently measured from σ_0 and σ_-, and within errors the data satisfy this relation. In principle, Eq. (5.10) could be regarded as a test of the spin- and phase-coherence assumption. In practice, it illustrates that with a reasonable model for ρ^0 production, σ_{10} gives an independent measure of the interference in σ_0 and σ_-; this is especially helpful where $\sigma_-(\rho)\ll\sigma_0(\rho)$, in which case σ_{10} gives a more sensitive measure than σ_- of the interference between $P_-(\rho)$ and $P_-(\omega)$.

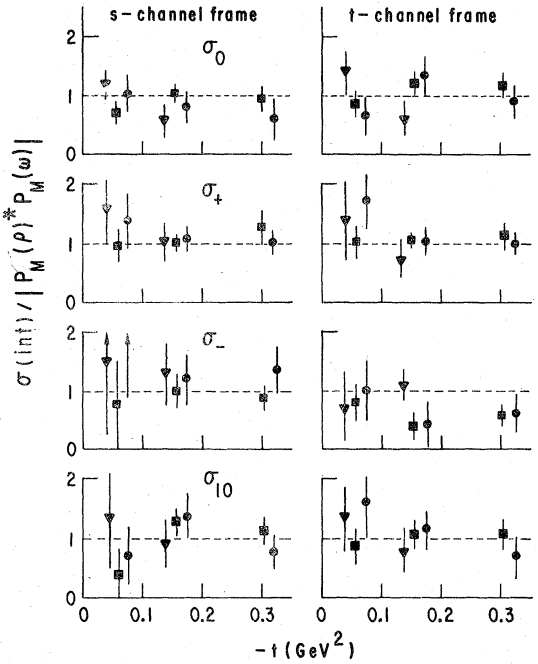

FIG. 28. Ratios of the ρ-ω interference magnitudes, $|\sigma_{ij}(\text{int})|/|\sigma_{ij}(\rho)|$, to the values of $|P_M(\rho)^*P_M(\omega)|/|P_M(\rho)|^2$, calculated from the model described in the text. Data at 3 GeV/c are plotted as triangles, 4 GeV/c as squares, and 6 GeV/c as circles. For an $\omega \to \pi^+\pi^-$ branching ratio $R = 0.01$, the expected value of the ratio is 1.0, which is shown by the dashed lines.

ω branching ratio. Given a model for ρ^0 and ω production amplitudes which specifies the ratios $|P_M(\rho)^*P_M(\omega)|/|P_M(\rho)|^2$ in Eq. (5.8b), we can use the measured interference magnitudes from Table IX to determine the parameter ϵ. We have constructed a parametrization of the ω production amplitudes based on measured ω cross sections. This parametrization is discussed in more detail in Sec. VI. It is sufficient to note here that it ignores possible Z exchange and assumes essentially the same nucleon-helicity structure for $P_M(\omega)$ as for the ρ production amplitudes of Sec. IV. The natural-parity-nonflip couplings for ρ and A_2 exchange [parameter r_A in Eq. (4.20b)] were varied over the range $0 < r_{A,\rho} < 0.5$ GeV without significantly affecting the results. Consistent values of the $\omega \to \pi^+\pi^-$ branching ratio were obtained at the three energies in the range

$$R = \frac{\Gamma(\omega \to \pi^+\pi^-)}{\Gamma(\omega \to \text{all})} = 0.010 \pm 0.001 . \tag{5.11}$$

We remind the reader that this value would increase if substantial spin incoherence between the ρ and ω production amplitudes were assumed.

Figure 28 shows the observed ρ-ω interference magnitudes, $|\sigma_{ij}(\text{int})|/|\sigma_{ij}(\rho)|$, divided by the expected values $|P_M(\rho)^*P_M(\omega)|/|P_M(\rho)|^2$ as calculated with the model. The resulting ratios should be consistent with unity for $R = 0.01$. The systematic discrepancies that can be seen are (1) $|\sigma_0(\text{int})|$ may be systematically low in the s channel for $-t > 0.08$ GeV^2, and (2) likewise $|\sigma_-(\text{int})|$ appears to be systematically low in the t channel for the same t range. Overall the ratios are in reasonable agreement with unity, especially considering the wide dynamic range expected for $|\sigma_{ij}(\text{int})|$.

Interference effects in ω production. In order to perform an amplitude analysis of the ω production data, it is necessary to take account of ρ-ω interference effects in the reactions

$$\pi^\mp N \to \pi^+\pi^-\pi^0 N . \tag{5.12}$$

The same arguments used to obtain Eq. (5.1) lead to the following expressions for the 3π production cross sections:

$$\sigma_{ij}(\pi^\mp N \to 3\pi N) = \sigma_{ij}(\pi^- p \to \omega n)\left(1 \pm 2\epsilon\,\text{Re}\left[\frac{P_M(\omega)^* P_M(\rho) B_\rho(m_\omega)}{|P_M(\omega)|^2}\right]\right), \tag{5.13}$$

where we have integrated over the ω width and have ignored terms of order ϵ^2 and higher. The desired ω production observables can be extracted from the 3π production data by the relation

$$\sigma_{ij}(\omega) = \sigma_{ij}(\pi^\mp N \to 3\pi N)\left(1 \mp \frac{|\sigma_{ij}(\text{int})|}{|\sigma_{ij}(\rho)|}\,\frac{\sigma_{ij}(\rho)}{\sigma_{ij}(\omega)}(0.050\sin\phi_{ij} - 0.009\cos\phi_{ij})\right) . \tag{5.14}$$

The quantities ϕ_{ij} and $|\sigma_{ij}(\text{int})|/|\sigma_{ij}(\rho)|$ on the right-hand side of Eq. (5.14) are just the measured parameters in Table IX. The quantities $\sigma_{ij}(\rho)/\sigma_{ij}(\omega)$ are the ratios of ρ and ω production intensities in each dme. Note that Eq. (5.14) does not depend on any assumptions about the structure of $P_M(\rho)$ and $P_M(\omega)$, or on the explicit value of ϵ. A first approximation for correcting the ω data is provided by the expression

$$\sigma_{ij}(\omega) = \sigma_{ij}(\pi^- p \to 3\pi n)\left[1 + \frac{0.20}{(1 + t/t_0)}\right], \tag{5.15}$$

where $t_0 = -0.22$ GeV^2 for σ_0, σ_-, and σ_{10}, and $t_0 = -0.025$ GeV^2 for σ_+. Equation (5.15) gives the ω production observables within ~10%, and we have used it to correct the ω data of Ref. 9 whenever

we have made use of it, e.g., in Fig. 27 and throughout Sec. VI. In fits to the ω data we have found that both Eqs. (5.14) and (5.15) yield similar results.

C. Summary

To summarize this section, we have presented ρ-ω interference parameters for observables σ_0, σ_+, σ_-, and $\mathrm{Re}\sigma_{10}$. Depending on assumptions about ρ production and about spin coherence between ρ and ω amplitudes, these interference parameters give direct information on the relative phases of ρ and ω helicity amplitudes. The magnitudes of the ρ-ω interference effects are consistent with measured ω and ρ cross-section ratios. Assuming spin coherence between the ρ and ω production amplitudes we obtain a branching ratio for $\omega \to \pi^+\pi^-$ of $(1.0 \pm 0.1)\%$, consistent with the Particle Data Group world average of $1.3 \pm 0.3\%$.[41]

VI. COMPARISON OF ρ, ω, K^*, and $\bar{K}^*$ PRODUCTION

So far we have examined the features of ρ^0 production and ρ-ω interference in the context of simple phenomenological models, but have delayed consideration of K^{*0} and $\bar{K}^{*0}$ production until the present section. While the P-wave observables for the K^{*0} and $\bar{K}^{*0}$ data were extracted in the same way as for ρ^0 production, as described in Secs. III and IV, the significance of the results is most conveniently understood within the phenomenological framework of SU(3) symmetry and strong exchange degeneracy. This comparison requires the use of the high-statistics ω-production data of Ref. 9 in addition to our own data on ρ^0 production and ρ-ω interference, and is the principal concern of this section.

SU(3) symmetry[11,49] relates the production amplitudes for the four vector-meson reactions (1.8), (1.9), (1.10), and (1.11) as follows:

$$P_M(K^*) = \frac{P_M(\rho) + P_M(\omega)}{\sqrt{2}}, \tag{6.1a}$$

$$P_M(\bar{K}^*) = \frac{P_M(\rho) - P_M(\omega)}{\sqrt{2}}. \tag{6.1b}$$

These relations are obtained by requiring SU(3) symmetry in the meson-vertex couplings in addition to the ideal ω-ϕ mixing pattern, which forces the amplitudes for $\pi^- p \to \phi n$ to vanish. The following predictions can be tested with experimental observables:

$$\sigma_M(K^*) + \sigma_M(\bar{K}^*) = \sigma_M(\rho) + \sigma_M(\omega), \tag{6.2a}$$

$$\sigma_M(K^*) - \sigma_M(\bar{K}^*) = 2\,\mathrm{Re}[P_M(\rho)^* P_M(\omega)]. \tag{6.2b}$$

The sum rule, Eq. (6.2a), has been tested by several authors.[7,10,57] The difference relation, Eq. (6.2b), is especially interesting because it relates line-reversal breaking in K^* and $\bar{K}^*$ production to the ρ-ω intereference observables.

In simple models, such as the Regge-pole model of Goldhaber, Fox, and Quigg (GFQ),[54] the requirements of SU(3) symmetry and strong exchange degeneracy (EXD) together dictate the form of the scattering amplitudes. In the GFQ model, the $G = \pm 1$ pairs of trajectories, $\pi + B$ and $\rho + A_2$, satisfy perfect EXD, so that $P_M(\rho)$ and $P_M(\omega)$ are 90° out of phase. With the requirement that the exotic K^*-production amplitudes for reaction (1.11) be real, the SU(3) relations predict the following constraints:

$$P_M(\bar{K}^*)/P_M(K^*) = e^{-i\pi\alpha(t)}, \tag{6.3a}$$

$$P_M(\omega)/P_M(\rho) = i\tan\left(\frac{\pi\alpha(t)}{2}\right), \tag{6.3b}$$

where $\alpha(t)$ denotes the EXD trajectories $\pi + B$ for unnatural-parity exchange and $\rho + A_2$ for natural-parity exchange.

A pure Regge-pole model such as GFQ is not likely to provide a good quantitative description of vector-meson production, since nonfactorizable absorptive cuts are manifestly important in ρ^0 production, as discussed in Sec. IV. The GFQ prediction from Eq. (6.3a) of line-reversal symmetry, $\sigma(K^*) = \sigma(\bar{K}^*)$, is not compatible with the data presented in Table V. Moreover, the cross-section ratio, $\sigma(\omega)/\sigma(\rho) = \tan^2[\pi\alpha(t)/2]$, predicted by Eq. (6.3b), does not agree with the ratios shown in Fig. 27; a single trajectory, $\alpha_{\pi,B}(t)$, would be insufficient to describe both the σ_0 and σ_- unnatural-parity cross sections, and no reasonable ρ-A_2 trajectory would describe the behavior of $\sigma_+(\omega)/\sigma_+(\rho)$.

The GFQ model also gives specific predictions for the ρ-ω interference phases: Equation (6.3b) implies $\phi_\omega - \phi_\rho = 90°$ for $\alpha(t) > 0$ ($\rho + A_2$ exchange for $-t < 0.50$ GeV^2), and $\phi_\omega - \phi_\rho = 270°$ for $\alpha(t) < 0$ ($\pi + B$ exchange). The experimental ρ-ω interference phase tend to support these predictions. First, the interference phase in σ_0, which isolates $\pi + B$ exchange, is $292° \pm 16°$ in the t channel and $291° \pm 27°$ in the s channel, averaged over energy and momentum transfer (the errors quoted are rms spreads). Second, in the limit of large $-t$ and high energies, the interference phase for σ_+ seems to approach the GFQ prediction of $+90°$; the large $-t (0.2 < -t < 0.4$ GeV^2) phase in σ_+ is $195° \pm 7°$ at 4 and 6 GeV/c, and $132° \pm 9°$ at 17 GeV/c.[4] Presumably at small $-t$ and lower energies the pion cut in σ_+ invalidates the GFQ prediction. Thus, the GFQ model seems to explain qualitatively the ρ-ω interference phases, although refinements in the model are needed to explain deviations from Eq. (6.3).

A number of physical mechanisms can be invoked

to explain departures from the simple GFQ model. For example, absorptive corrections provide a mechanism for violating SU(3) symmetry. The relations of Eq. (6.1) are derived for the t-channel Regge-pole terms; these relations should apply equally well to the s-channel pole terms, since the crossing relations are essentially the same for the four vector-meson reactions. Considering only Pomeron-Regge cuts, the absorptive corrections, which are proportional to the s-channel Regge-pole amplitudes, should themselves satisfy SU(3) to the extent that the Pomeron rescattering amplitude is independent of reaction. However, there is evidence, discussed below, that the absorptive corrections are systematically weaker for $K^{\pm}N$ than for $\pi^{\pm}N$ initial states.

Mechanisms for line-reversal breaking, $\sigma(K^*) \neq \sigma(\bar{K}^*)$, are numerous. For example, the trajectories $\pi+B$ and $\rho+A_2$ are not themselves likely to be exactly degenerate.[32] The energy dependence of $\pi^-p \to \pi^0 n$ and $\pi^-p \to \eta n$ suggests that $\alpha_A(t) < \alpha_\rho(t)$.[58] Similarly, the ρ-ω interference phases of Table IX disagree systematically with the GFQ prediction of Eq. (6.3b), suggesting that the π and B trajectories are also different. Absorption provides another important mechanism for the breaking of line-reversal symmetry in vector-meson production, as pointed out by Fox.[59] As an illustration, strong $\pi+B$ cut contributions to the $n=0$ amplitude can interfere with the $\rho+A_2$ pole terms in the natural-parity cross section. Even if the $\pi+B$ cut and the $\rho+A_2$ pole terms separately satisfied EXD, their combination in P_+ would break the line-reversal relation; schematically we can write

$$P_+(K^*) = g_{\pi,B} + g_{\rho,A}\,, \tag{6.4a}$$

$$P_+(\bar{K}^*) = g_{\pi,B}(e^{-i\pi\alpha_{\pi,B}}) + g_{\rho,A}(e^{-i\pi\alpha_{\rho,A}})\,. \tag{6.4b}$$

The individual $\pi+B$ and $\rho+A_2$ terms in Eq. (6.4) satisfy the line-reversal relation, Eq. (6.3a). However, the trajectories $\alpha_{\pi,B}$ and $\alpha_{\rho,A}$ are not simply related, and the interference of natural- and unnatural-parity contributions in Eq. (6.4) breaks the EXD equality of $\sigma_+(K^*)$ and $\sigma_+(\bar{K}^*)$. Although this mechanism is of singular importance for understanding the line-reversal breaking in K^* and $\bar{K}^*$ production, as discussed below, it nevertheless does not refute the basic GFQ picture but merely complicates the interpretation of the data.

We will use the vector-meson production data to examine the validity of SU(3) symmetry and the mechanisms by which exchange degeneracy in the amplitude structure is broken. We proceed by investigating (1) the properties of the ω-production amplitudes, (2) the features of K^* and $\bar{K}^*$ production data from this experiment, (3) tests of the SU(3) sum rules [Eq. (6.2a)], (4) the relationship between K^*-$\bar{K}^*$ line-reversal breaking and the ρ-ω interference phases, (5) comparison with higher-energy data on $\bar{K}^*$ production and ρ-ω interference, and (6) phenomenological descriptions of the vector-meson production mechanisms which aim to explain the deviations from the GFQ model. We call attention to a similar analysis by Estabrooks and Martin,[60] which used a subset of the present data, and also to the analysis by Emms *et al.*,[10] which used preliminary data from this experiment.

A. Features of ω production

We have relied on the high-statistics data of Shaevitz *et al.*[9] to determine in detail the t dependence of the ω production observables in the reaction $\pi^-p \to \omega n$ [reaction (1.9)]. The 6-GeV/c cross sections, σ_0 and $\sigma_\pm$, from Ref. 9 are plotted in Fig. 29; these data have been corrected for ρ-ω interference using Eq. (5.15), and the curves represent our parametrization of the ω-production amplitudes which is given explicitly in Table X, together with the fitted parameters.

The energy dependence given in Table X is designed to provide a smooth interpolation of lower-energy data. Unfortunately the energy dependence

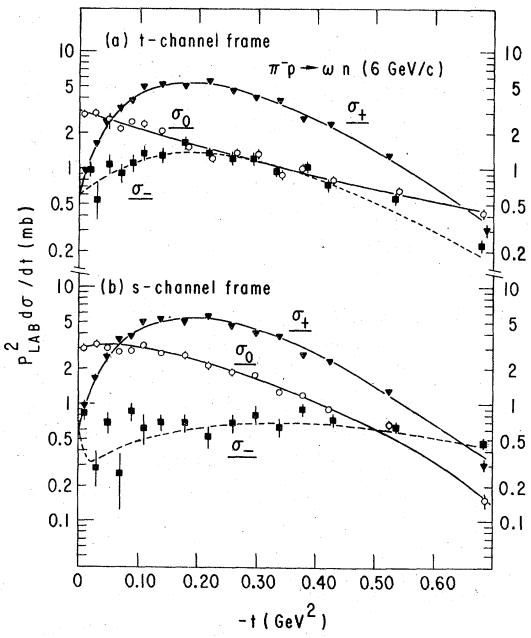

FIG. 29. Differential cross sections for $\pi^-p \to \omega n$ at 6 GeV/c from the data of Ref. 9, corrected for ρ-ω interference effects. The quantities plotted are $\sigma_M = p_{\rm lab}{}^2 \rho_M d\sigma/dt$; the curves are from our parametrization of the data which is given in Table X. Open circles are σ_0, triangles are σ_+, and squares (with dashed curves) are σ_-.

TABLE X. Parametrization of the ω production amplitudes together with parameters obtained from fits to the data: (1) The parameters ω_M, B_M, and H_M are from fits to the 6-GeV/c ω-production data of Ref. 9. (2) The parameters g_A, B_A, r_A, and α_A are fixed by the fits to ρ^0-production data and are given in Table VII. (3) The parameters ϕ_M and ϕ'_M are from fits to the K^* and $\bar{K}^*$ data at 3, 4, and 6 GeV/c from this experiment using Eq. (6.2b); the fits were over the ranges $-t < 0.45$ GeV^2 (4 and 6 GeV/c) and $-t < 0.28$ GeV^2 (3 GeV/c). The notation $t' = t - t_{\min}$ is used throughout.

$$P^0_{++}(t \text{ chan}) = \omega_0 (e^{(B_0 t' + H_0 t'^2 + i\phi_0 + i\phi'_0 t')}) (p_{\text{lab}}/6)^t$$

$$P^-_{++}(t \text{ chan}) = (t'/t)^{1/2} \omega_+ (1 + H_- t') (e^{(B_- t' + i\phi_- + i\phi'_- t')}) (p_{\text{lab}}/6)^t$$

$$P^0_{+-}(t \text{ chan}) = \sin\chi (t_{\min}/t')^{1/2} P^-_{++}(t \text{ chan})$$

$$P^-_{+-}(t \text{ chan}) = (t_{\min}/t')^{1/2} P^-_{++}(t \text{ chan})$$

$$P^+_{+-}(s \text{ chan}) = \omega_+ (1 + H_+ t') (e^{[B_+ t' + i\psi_+(t)]}) (p_{\text{lab}}/6)^{\alpha_+(t)}$$

$$P^+_{++}(s \text{ chan}) = (1 + 2t) r_A (-t')^{1/2} g_A e^{B_A t'} (p_{\text{lab}}/6)^{0.5 + t'} [(\tfrac{17}{6})^{\alpha_A}] e^{i\pi/4}$$

where $\psi_+(t) = [\phi_+ + \phi'_+ t' - 50° \ln(p_{\text{lab}}/6)] (1 - e^{40t'}) + \phi_- e^{40t'}$

$\alpha_+(t) = 0.3(1 - e^{15t'}) + t$

$\omega_0 = 1.75 \pm 0.05$ mb$^{1/2}$ $B_0 = 1.81 \pm 0.30$ GeV^{-2} $H_0 = 0.46 \pm 0.77$ GeV^{-4}

$\omega_+ = 0.74 \pm 0.19$ mb$^{1/2}$ $B_+ = 4.75 \pm 0.09$ GeV^{-2} $H_+ = -33.8 \pm 2.6$ GeV^{-2}

$B_- = 3.93 \pm 0.25$ GeV^{-2} $H_- = -12.4 \pm 1.7$ GeV^{-2}

	3 GeV/c	4 GeV/c	6 GeV/c
ϕ_0	$287 \pm 3°$	$276 \pm 2°$	$286 \pm 3°$
ϕ_+	$74 \pm 18°$	$68 \pm 7°$	$78 \pm 8°$
ϕ_-	$135 \pm 7°$	$133 \pm 4°$	$144 \pm 8°$
ϕ'_0	$119 \pm 25°$ GeV^{-2}	$31 \pm 12°$ GeV^{-2}	$65 \pm 19°$ GeV^{-2}
ϕ'_+	$350 \pm 180°$ GeV^{-2}	$138 \pm 44°$ GeV^{-2}	$119 \pm 38°$ GeV^{-2}
ϕ'_-	$29 \pm 45°$ GeV^{-2}	$69 \pm 19°$ GeV^{-2}	$70 \pm 34°$ GeV^{-2}

of reaction (1.9) is not well established in the 3- to 6-GeV/c range. The parametrization which we have used agrees with that of Dowell *et al.*,[61] who have determined empirical trajectories from separate fits to data on $\pi^- p \to \omega n$ (4 to 12 GeV/c) and $\pi^+ n \to \omega p$ (4 to 7 GeV/c). Within the errors, their trajectories can be represented by the forms

$$\alpha_+(t) = t + 0.3 - 0.3 e^{15t'} \quad (P_+), \tag{6.5a}$$

$$\alpha_{-,0}(t) = t \quad (P_-, P_0), \tag{6.5b}$$

where we have introduced the constraint $\sigma_+ = \sigma_-$ at $t' = 0$. At much higher energies ($20 < p_{\text{lab}} < 200$ GeV/c) the natural-parity trajectory has been better determined:

$$\alpha_+(t) = 1.2t + 0.55 - 0.55 e^{15t'} \quad (P_+) \tag{6.5c}$$

adequately represents the data of Dahl *et al.*[62]; both the low- and high-energy data suggest the turnover in $\alpha_+(t)$ near $t = 0$, but the forward intercept, $\alpha_\pm(0)$, is not well determined. To obtain 3- and 4-GeV/c observables for subsequent analysis, we have simply extrapolated the 6-GeV/c data of Ref. 9, using the energy dependence implied by Eqs. (6.5a) and (6.5b); to allow for uncertainties in the extrapolation, we have attached 15% systematic errors to the lower-energy points.

The main differences between ω and ρ^0 production observables, as illustrated by Fig. 29, are that (1) the ω cross sections are flatter in t, and (2) ω production is dominated by natural-parity exchange. The latter feature is anticipated by the GFQ model.[54] According to the GFQ prediction of Eq. (6.3b), the ρ-exchange contribution to $P_+(\omega)$ should be comparable in strength to the A_2-exchange contribution to $P_+(\rho)$; by contrast, the un-

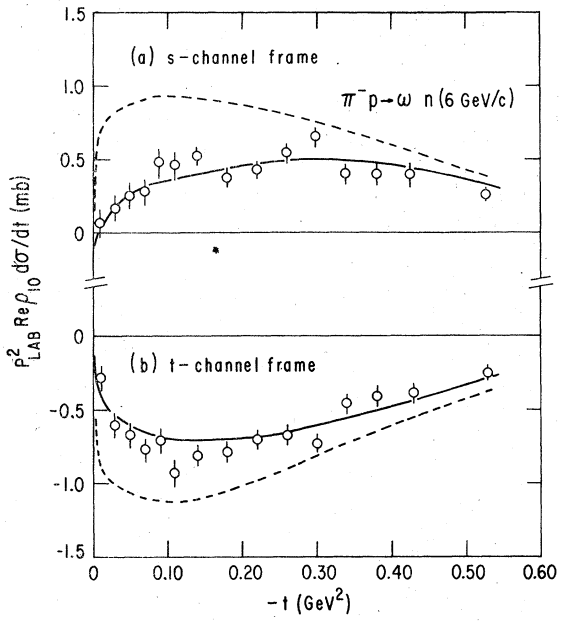

FIG. 30. The interference cross section $\mathrm{Re}\sigma_{10} = p_{1ab}{}^2 \mathrm{Re}\rho_{10} d\sigma/dt$, for $\pi^- p \to \omega n$ at 6 GeV/c from the data of Ref. 9, corrected for ρ-ω interference effects. The solid curves are from our parametrization of Table X, which allows for a phase difference between P_- and P_0; the dashed curves show the maximum values of $\mathrm{Re}\sigma_{10}$, assuming phase and spin coherence between P_- and P_0.

natural-parity amplitudes $P_-(\omega)$ and $P_0(\omega)$ should be suppressed compared to $P_-(\rho)$ and $P_0(\rho)$, assuming $\alpha_{\pi,B}(t) \approx 0$.

The forward peaking in $\sigma_+(\rho)$, as discussed in Sec. IV, is evidence that at small $-t$ $P_+(\rho)$ is dominated by the nonfactorizing π-exchange cut. By contrast, the sharp turnover of $\sigma_+(\omega)$ near $t=0$ (Fig. 29) suggests that $P_+(\omega)$ is dominated by a factorizable ρ-exchange Regge-pole contribution; similar behavior is expected for the A_2-exchange contribution to $P_+(\rho)$, as explained in Sec. IV C. In addition, the persistence of a small but finite forward intercept in $\sigma_\pm(\omega)$ suggests that $P_+(\omega)$ and $P_-(\omega)$ receive small $n=0$ cut contributions, which can arise from both ρ and B exchange.

In the case of ρ^0 production, the approximate phase coherence observed between $P_0(\rho)$ and $P_-(\rho)$ can be explained by the dominance of π exchange relative to possible small A_2-cut contributions in $P_-(\rho)$. Given the apparent dominance of ρ exchange in ω production, we might expect the $n=0$ ρ-exchange cut to be a relatively large component of $P_-(\omega)$, and to break the phase coherence between $P_-(\omega)$ and $P_0(\omega)$, since the ρ- and B-exchange terms have different Regge phases. Figure 30 shows the interference cross section, $\mathrm{Re}(\sigma_{10})$, for ω production. The solid curves are from the fit described in Table X, which imposes spin coherence but allows for a phase difference between $P_-(\omega)$ and $P_0(\omega)$; the dashed curves give the maximum allowed $\mathrm{Re}[\sigma_{10}(\omega)]$, assuming complete phase and spin coherence between $P_-(\omega)$ and $P_0(\omega)$. Phase differences of typically $\pm 50°$ are required by the data.

The parametrization of nucleon-spin dependence in ω production given by Table X is based on the discussion of Sec. IV. Theoretically, π- and B-exchange Regge poles should have the same nucleon-helicity structure, as explained in Sec. III C. If we assume similar absorption effects at small $-t$ for ρ and ω production, in particular strong $n=0$ nonfactorizing cuts, then the t-channel unnatural-parity spin structure implied by Eq. (4.18) should apply to both reactions, as indicated in Tables VII and X. Our parametrization also assumes that $P_+(\omega)$ is dominantly nucleon-helicity flip in the s channel. We have included a small ρ-exchange nonflip contribution, $P^+_{++}(\omega)$, which is related by EXD to the corresponding A_2-exchange term, $P^+_{++}(\rho)$, in Table VII.

The magnitudes of the ω production amplitudes, $|P_{0,\pm}(\omega)|$, are chosen to be simple functions of t and are determined by fits to the ω cross sections of Fig. 29. The phases of $P_0(\omega)$ and $P_-(\omega)$ are parametrized as linear functions of momentum transfer in the t channel. The phase of $P^+_{+-}(\omega)$ is also taken to be linear in t, except for a correction at small $-t$ which is added to satisfy the constraint $P^+_{+-}(\omega) = P^-_{+-}(\omega)$ at $t = t_{\min}$. Thus six parameters determine the ω-production phases at each energy. These parameters can be obtained in three ways: (1) by fitting the ρ-ω interference phases under the constraint that the ρ production amplitudes be real as in Table VII; (2) by fitting $\sigma_{10}(\omega)$ to obtain the relative phase of $P_-(\omega)$ and $P_0(\omega)$; (3) by fitting the difference cross sections, $\sigma(K^*) - \sigma(\bar{K}^*)$, using the SU(3) relation of Eq. (6.2b). The parameters of Table X and Fig. 30 were obtained from the last method, which is discussed in detail below; however, all three methods give consistent results.

In order to fit ω production data we have ignored the $\sqrt{-t}$ factor in $P_0(\omega)$, which is theoretically required for the B-exchange Born term.[27] The absence of a turnover in $\sigma_0(\omega)$ at small $-t$ is the basis for the Z-exchange mechanism hypothesized by Irving.[56] The Z and B exchanges are expected to add incoherently in $\sigma_0(\omega)$, the former varying like $\sigma_0 \propto t'/t$ at small $-t$, the latter like $\sigma_0 \propto t$.[27,63] Although the small $-t$ behavior of $\sigma_0(\omega)$ appears to be inconsistent with pure B exchange, the relative strength of B- and Z-type exchanges at larger $-t$ is not known experimentally. Our ρ-ω interference data do not require a large Z-exchange contribu-

tion, since the magnitude of the interference in σ_0 (Fig. 28) is compatible with perfect spin coherence over the entire t range. Of course, if we assume a larger $\omega \to \pi^+\pi^-$ branching ratio, these data are also compatible with the simultaneous presence of substantial spin incoherence in all the observables (σ_0, σ_-, and σ_+), over the entire t range.[64]

If $\sigma_0(\omega)$ were dominated by Z exchange, then the three methods of fitting the ω-production phases described above would in general give inconsistent results. For concreteness, assume that the ρ production parametrization of Table VII is correct (no A_1 exchange) but that Z exchange contributes strongly to s-channel $P^0_{++}(\omega)$. Then the three methods measure the following distinct quantities: (1) The ρ-ω interference phases are precisely the relative phases $\phi^M_{+-}(\rho) - \phi^M_{+-}(\omega)$. (2) The K^*-$\bar{K}^*$ cross-section difference, $\sigma_0(K^*) - \sigma_0(\bar{K}^*)$, measures the quantity $\xi_\omega \cos[\phi^0_{+-}(\rho) - \phi^0_{+-}(\omega)]$, where ξ_ω is the coherence factor defined by $\xi_\omega = |P^0_{+-}(\omega)|/[\sigma_0(\omega)]^{1/2}$. If ξ_ω were overestimated, owing to neglect of Z exchange, the phase difference $\phi^0_{+-}(\rho) - \phi^0_{+-}(\omega)$ would be overestimated. (3) $\sigma_{10}(\omega)$ measures the quantity $\xi_\omega \cos[\phi^0_{+-}(\omega) - \phi^-_{+-}(\omega)]$. If Z exchange were neglected ($\xi_\omega = 1$), then the relative phase $\phi^0_{+-}(\omega) - \phi^-_{+-}(\omega)$ would be overestimated. The phases $\phi^{0,-}_{+-}(\omega)$ so derived would be systematically different in each case. Empirically, the three phase determinations appear to be consistent, as discussed below. Therefore, in lieu of firm evidence on Z exchange from polarization measurements, and given the internal consistency of our results, we have chosen to parametrize the ω-production data using the simple spin structure of Table X, despite the theoretical inconsistency at small $-t$.

B. K^* and $\bar{K}^*$ production

The K^{*0} and $\bar{K}^{*0}$ production observables for reactions (1.10) and (1.11) from Table V are plotted in Figs. 31 through 36, together with the results of our fits. The fits provide a comparison with the SU(3) predictions and are based on the ρ and ω production amplitudes, as discussed below. According to the SU(3) relation, Eq. (6.2b), the differences between K^* and $\bar{K}^*$ observables can be expressed as

$$\sigma_M(K^*) - \sigma_M(\bar{K}^*) = 2P_M(\rho)\,\mathrm{Re}[P_M(\omega)], \qquad (6.6)$$

where the ρ production amplitudes, $P_M(\rho)$, are taken to be real by convention, as in Table VII. The difference cross sections given by Eq. (6.6) can be large to the extent that (1) $P_M(\rho)$ and $P_M(\omega)$ are not $\pm 90°$ out of phase, and (2) the ratio $|P_M(\omega)|/|P_M(\rho)|$ is not small. Using the SU(3) predictions as a framework for discussion, we can compare the

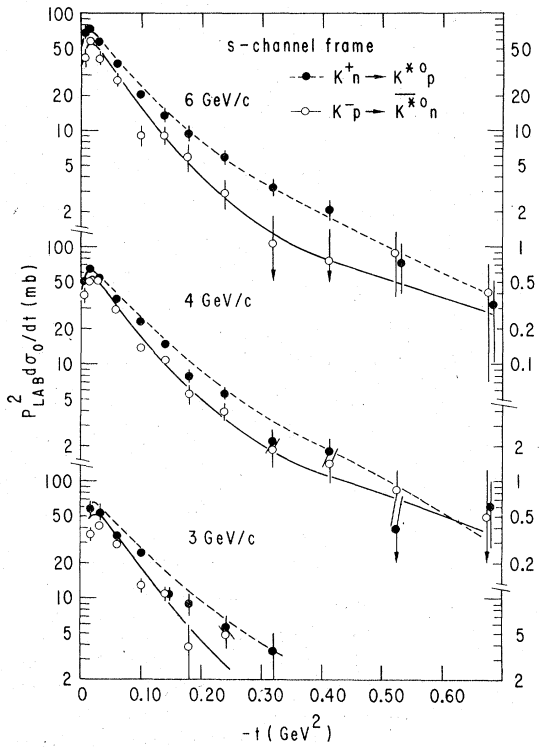

FIG. 31. The helicity-0 cross sections for K^{*0} and $\bar{K}^{*0}$ production in the s channel. The curves show the results of the SU(3)-constrained fits described in the text.

main features of K^*- and $\bar{K}^*$-production observables as follows:

σ_0. The σ_0 cross sections are systematically larger for K^* than for $\bar{K}^*$ in the s channel (Fig. 31), whereas in the t channel these cross sections are nearly equal (Fig. 32). Estabrooks and Martin[60] hypothesized that the t-channel P_0 amplitudes satisfy EXD especially well, resulting in the equality of $\sigma_0(K^*)$ and $\sigma_0(\bar{K}^*)$. From the standpoint of SU(3), the apparent success of EXD in the t channel could be viewed as accidental. As noted earlier, the $P_0(\omega)$ phases from ρ-ω interference are on average the same in both s and t channels (290°) and are close to the EXD value of 270°. The reason that the cross-section difference, $\sigma_0(K^*) - \sigma_0(\bar{K}^*)$, is smaller in the t channel is mainly that the ratio, $\sigma_0(\omega)/\sigma_0(\rho)$, happens to be much smaller in the t channel than in the s channel (Fig. 27).

σ_+. The natural-parity cross sections are markedly different for K^* and $\bar{K}^*$ (Fig. 33). In the forward direction, $\sigma_+(K^*)$ is about twice as large as $\sigma_+(\bar{K}^*)$; the cross-section difference vanishes around $-t = 0.05$ GeV^2, and at larger $-t$ $\sigma_+(K^*)$ is much smaller than $\sigma_+(\bar{K}^*)$. These differences are compatible with SU(3) in the sense that $\sigma_+(\omega)/\sigma_+(\rho)$ is large over most of the t range (Fig. 27). From

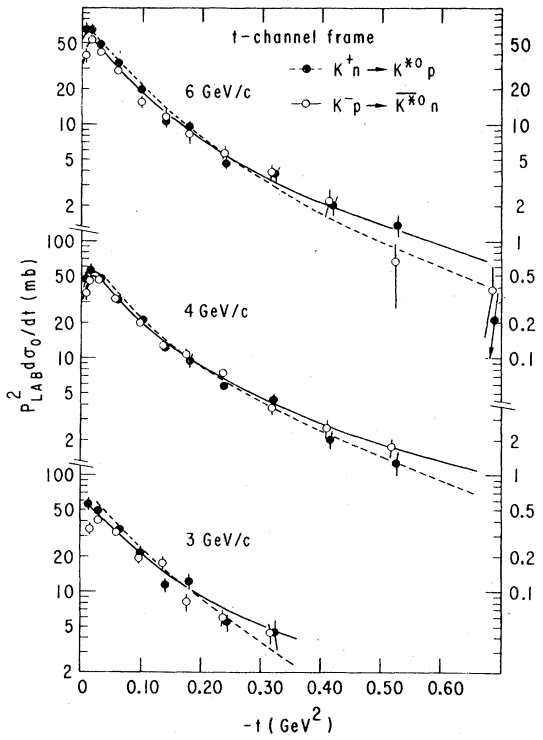

FIG. 32. The helicity-0 cross sections for K^{*0} and $\bar{K}^{*0}$ production in the t channel. The meaning of the curves is the same as in the previous figure.

Eq. (6.6), it follows that $\mathrm{Re}[P_+(\omega)]$ has a crossover zero around $-t = 0.05$ GeV^2, since $P_+(\rho)$ is presumably a smooth function of t. This crossover phenomenon could be attributed to an $n = 0$ absorptive cut in the ρ-exchange amplitude, analogous to the WM zero caused by the π cut in $P_-(\rho)$.

σ_-. In the s channel, $\sigma_-(K^*)$ tends to be somewhat smaller than $\sigma_-(\bar{K}^*)$ (Fig. 34), except near $t' = 0$, where $\sigma_- = \sigma_+$ is required; in the t channel, $\sigma_-(K^*)$ is significantly larger than $\sigma_-(\bar{K}^*)$ (Fig. 35). This behavior is again consistent with SU(3) in the respect that the ratio $\sigma_-(\omega)/\sigma_-(\rho)$ is generally much larger in the t channel than in the s channel (Fig. 27).

$P^{\parallel}_-$. The component $P^{\parallel}_-$ (Fig. 36) has been derived from $\mathrm{Re}[\sigma_{10}(K^*,\bar{K}^*)]$ using an amplitude analysis similar to that described in Sec. IV for ρ^0 production. The corrections to the K^* and $\bar{K}^*$ observables for s-channel-nonflip (t-channel-flip) contributions were obtained via SU(3) from the nonflip (flip) ρ and ω production amplitudes of Tables VII and X. Thus, s-channel $P^{\parallel}_-$ in Fig. 36 is defined as the component of $P^-_{+-}(K^*,\bar{K}^*)$ which is real relative to the amplitude $P^0_{+-}(K^*,\bar{K}^*)$; in the t channel, $P^{\parallel}_-$ is the component of $(t/t')^{1/2}P^-_{++}(K^*,\bar{K}^*)$ which is real relative to $P^0_{++}(K^*,\bar{K}^*)$. These definitions are such that the $P^{\parallel}_-$ components are the same in the s and t channels at $t' = 0$.

In the t channel, $P^{\parallel}_-$ is negative and is typically twice as large for K^* as for $\bar{K}^*$. In the s channel, $P^{\parallel}_-$ is somewhat smaller for K^* than for $\bar{K}^*$, away from $t' = 0$. Note also that the WM zero in s-channel $P^{\parallel}_-$ is displaced to larger $-t$ for K^* as compared with $\bar{K}^*$.

The behavior of the helicity-1 observables, $\sigma_\pm$ and $P^{\parallel}_-$, suggests a simple mechanism which strongly influences the relation between the K^* and $\bar{K}^*$ amplitudes, namely that the $n = 0$ cut contribution to $\mathrm{Re}[P_\pm(\omega)]$, associated with ρ and B exchange, has the same sign as the $n = 0$ π cut in $P_\pm(\rho)$. By SU(3) symmetry, these two contributions add constructively for K^* and destructively for $\bar{K}^*$ production. As a result, at $t' = 0$ the observables $\sigma_\pm$ and $P^{\parallel}_-$ are all larger for K^* than for $\bar{K}^*$. As in ρ^0 production, $P^{\parallel}_-$ and σ_- in the t channel are dominated by the $n = 0$ cut contribution and are therefore larger for K^* than for $\bar{K}^*$ over the entire t range. The EXD breaking in σ_+ at larger $-t$ is explained by the mechanism of Fox[59]; the destructive interference of the ρ pole with the $n = 0$ cut causes

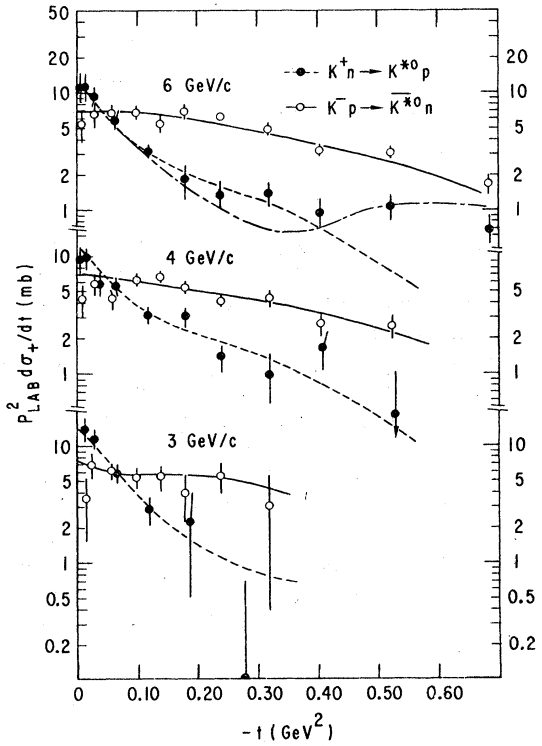

FIG. 33. The helicity-1 natural-parity-exchange cross sections for K^{*0} and $\bar{K}^{*0}$ production. The meaning of the curves is the same as in the previous two figures, except that the dot-dashed curve shows the effect on the 6-GeV/c K^* fit of using a nonflip-to-flip ratio $r_A = 0.50$ GeV, instead of the $r_A = 0.25$-GeV value used for the other curves. This change has a negligible effect on the $\bar{K}^*$ fits.

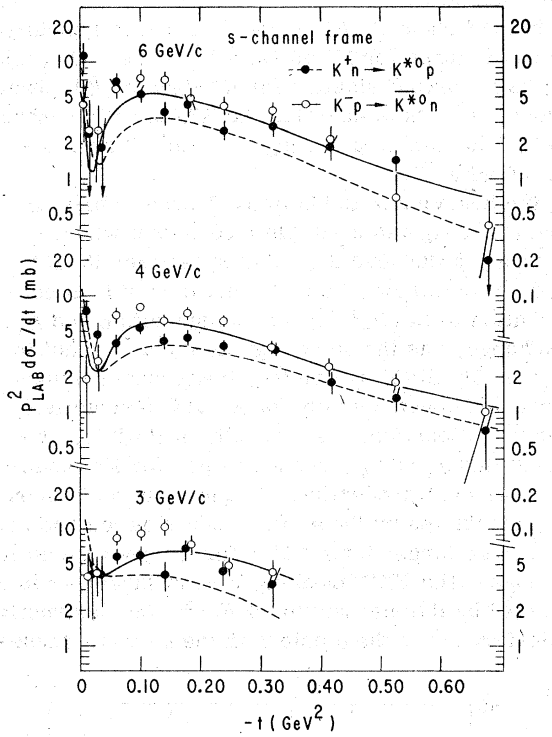

FIG. 34. The helicity-1 unnatural-parity-exchange cross sections for K^{*0} and $\bar{K}^{*0}$ production in the s channel. The meaning of the curves is the same as in Fig. 31.

$\sigma_+(K^*) < \sigma_+(\bar{K}^*)$.

The fitted curves in Figs. 31 through 36 are based on the SU(3) predictions. The fits to the K^* and $\bar{K}^*$ data were restricted to the range $-t < 0.45$ GeV^2 (4 and 6 GeV/c) and $-t < 0.28$ GeV^2 (3 GeV/c) because this is approximately the region covered by the ρ-ω interference measurements with which we wish to compare. The K^* and $\bar{K}^*$ amplitudes used in the fits were taken to be the linear combinations of ρ^0 and ω amplitudes prescribed by Eq. (6.1). The ρ^0 production amplitudes were parametrized as in Table VII, and the magnitudes of the ω amplitudes were fixed as in Table X, from the fits to the ω cross sections. The only quantities varied in the fits to the K^* and $\bar{K}^*$ data were the six parameters that specify the ω-production phases. The results of the fits at 3, 4, and 6 GeV/c are listed in Table X. The parameters ϕ_M, which give essentially the $t = 0$ intercepts of the phases of $P_M(\omega)$, appear to be independent of energy within errors. Note that the phase of $P_+(\omega)$ as given in Table X includes some explicit energy dependence; this was introduced to remove the energy dependence of the parameter ϕ_+. The slope parameters, ϕ'_M, are not well determined but show no systematic variation with energy. We emphasize that the ω-production phases given in Table X are not absolute but are measured relative to the ρ^0-production phases. As a matter of convention we chose $P_0(\rho)$ and $P_+(\rho)$ in Table VII to be purely real. Note that $P_-(\rho)$ was also constrained to be purely real, but small phase differences between $P_-(\rho)$ and $P_0(\rho)$ are not ruled out by the data, as discussed in Sec. IV.

As can be seen by inspection of Figs. 31 through 36, the fits are rather poor; averaged over all data points, χ^2/degree of freedom is 2. However, the systematic discrepancies appear to be due, not to our parametrization of the ω phases, which determines the difference between K^* and $\bar{K}^*$ observables, but rather to the fact that the SU(3) sum rules of Eq. (6.2a) are violated. To the extent that these sum rules fail, no choice of ω phases can simultaneously fit the K^* and $\bar{K}^*$ cross sections. In order to improve the fits somewhat, we have modified the SU(3) predictions with empirical correction factors to increase the t-channel unnatural-parity amplitudes:

$$P_M(K^*) = \frac{1}{\sqrt{2}}[P_M(\rho) + P_M(\omega)]\, e^{\beta_M t'}, \qquad (6.7a)$$

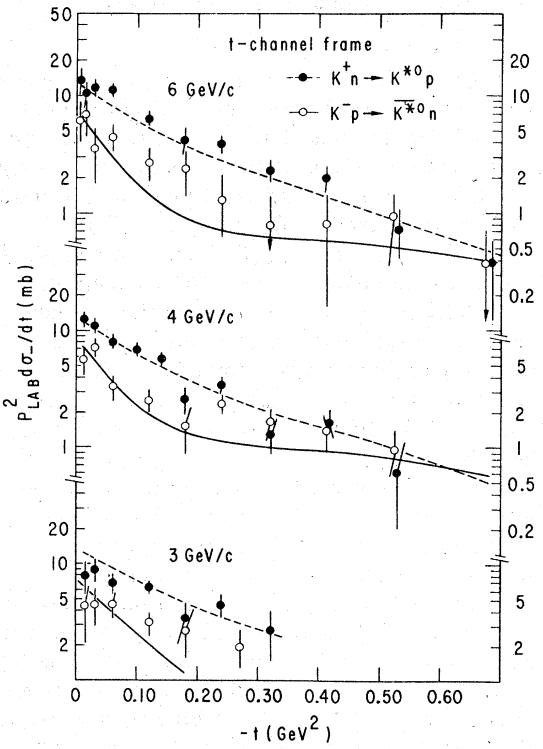

FIG. 35. The helicity-1 unnatural-parity-exchange cross sections for K^{*0} and $\bar{K}^{*0}$ production in the t channel. The meaning of the curves is the same as in Fig. 31.

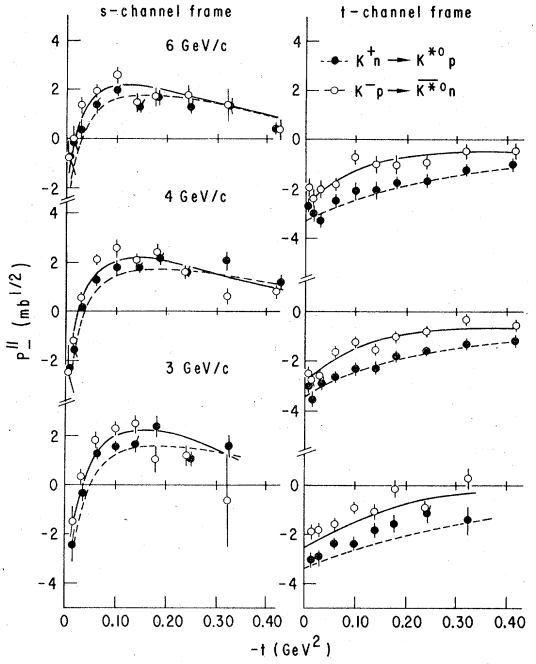

FIG. 36. The quantity P_-^{II} for K^{*0} and $\overline{K}^{*0}$ production, derived from our amplitude analysis. P_-^{II} is the component of P_- which is parallel to P_0 in the complex plane. In the s channel, P_-^{II} refers to the dominant flip contribution P_{+-}^{-}; in the t channel, P_-^{II} refers to the quantity $(t/t')^{1/2}P_{++}^{-}$. The curves show the results of the SU(3)-constrained fits described in the text.

$$P_M(\overline{K}^*) = \frac{1}{\sqrt{2}}[P_M(\rho) - P_M(\omega)]\, e^{\beta_M t'}, \qquad (6.7b)$$

where $\beta_0 = -0.25$ GeV^{-2} and $\beta_- = -0.60$ GeV^2; no correction was needed for P_+. These factors are inadequate to correct P_- over the entire t range, and consequently the fits tend to be low compared with measured σ_- (Fig. 35). In general, the fits give satisfactory χ^2's where the SU(3) sum rules work, and the ω-phase parametrization provides an adequate description of the essential differences between K^* and $\overline{K}^*$ observables.

We remark that the K^* and $\overline{K}^*$ data determine, via Eq. (6.6), not the actual ω-production phase but the cosine of the phase. We have resolved the quadrant ambiguity by appeal to the ρ-ω interference phases. Also, the fits to σ_+ are sensitive to the nonflip-to-flip ratio, r_A, assumed for the ρ- and A_2-exchange amplitudes $P_+(\omega)$ and $P_+(\rho)$. The parameter values in Table X and the fits in Fig. 33 are based on $r_A = 0.25$ GeV. A similar fit, with $r_A = 0.5$ GeV, is shown for the 6-GeV/c data in Fig. 33. Only the behavior of $\sigma(K^*)$, not $\sigma(\overline{K}^*)$, is affected by this choice; this is because $\sigma(K^*)$ is small to begin with at large $-t$, owing to the destructive cancellation of the $P_+(\omega)$ and $P_+(\rho)$ contributions to $P_+(K^*)$. Because of the EXD parametrization used in Tables VII and X, the nonflip amplitudes $P_{++}^{+}(K^*)$ and $P_{++}^{+}(\overline{K}^*)$ are equal in magnitude, and the nonflip cross section is relatively most important in $\sigma_+(K^*)$.

C. SU(3) sum rules

The sum rules from Eq. (6.2a) are illustrated for the 4- and 6-GeV/c data in Figs. 37 through 40. Agreement with SU(3) is generally rather good except for σ_-, which is systematically larger for $K^* + \overline{K}^*$ than for $\rho + \omega$. To assess the significance of the agreement, we remark that in regions where $\sigma(\omega)$ is very small compared with $\sigma(\rho)$, the sum rules cannot be sensitive to SU(3) violations in the ω amplitudes. The cross-section ratios of Fig. 27 show that $\sigma(\rho)$ completely dominates $\sigma(\omega)$ in the unnatural-parity-exchange cross sections for $-t < 0.3$ GeV^2. Consequently the sum rules for σ_0, σ_-, and σ_{10} at small $-t$ mainly test whether the π-exchange contribution to ρ, K^*, and $\overline{K}^*$ production satisfies SU(3). On the other hand, $\sigma(\omega)$ does affect the sum rules significantly at large $-t$, and actually dominates the σ_+ sum rule for $-t > 0.15$ GeV^2. Since SU(3) works remarkably well for σ_+ at large $-t$ (Figs. 37 and 38), we conclude that SU(3) is as

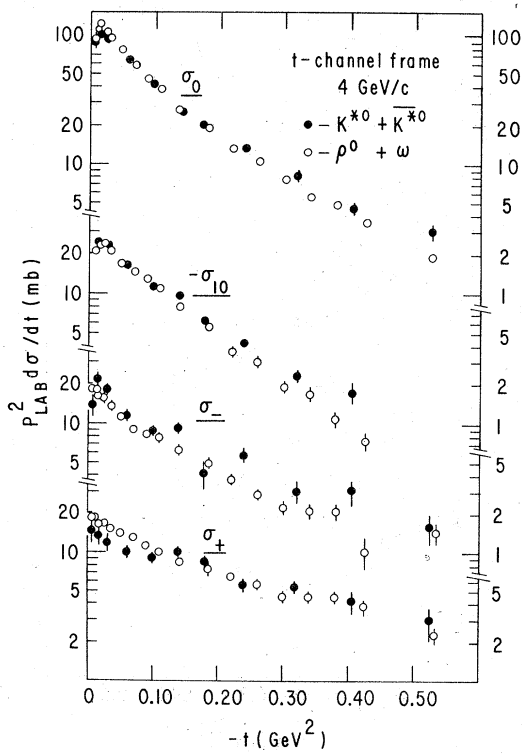

FIG. 37. SU(3) sum-rule comparison at 4 GeV/c in the t-channel frame.

reliable for the non-π-exchange contributions as it is for the π-exchange terms.

Indeed, the fact that the SU(3) sum rule is most prominently violated by σ_- over the entire t range suggests that SU(3) breaking may be most important for the π-exchange contribution; $\sigma_-(\omega)/\sigma_-(\rho)$ is very small in the s channel, and yet σ_- in the s channel is larger by 20 to 40% for $K^*+\bar{K}^*$ than for $\rho+\omega$ (Figs. 39 and 40). A plausible explanation for this SU(3) breaking in σ_- would be that absorptive cuts may be systematically weaker in K^* and $\bar{K}^*$ than in ρ or ω production; if the absorptive cuts scale roughly like the average of the $K^{\pm}N$ or $\pi^{\pm}N$ total cross sections, then absorptive cuts in K^* production would be weaker by about 25% in this energy range. Given that the WM description of absorptive cuts in P_{+-}^{-} is approximately valid [see Eq. (3.17)], a 25% reduction in the WM cut strength would produce a ~40% increase in s-channel σ_- for K^* and $\bar{K}^*$ production, consistent with observation. This mechanism for SU(3) breaking is discussed by Irving and Michael.[37]

SU(3) violation in the π-exchange contributions is expected to show up at some level in the sum rules for s-channel σ_0, since this quantity should

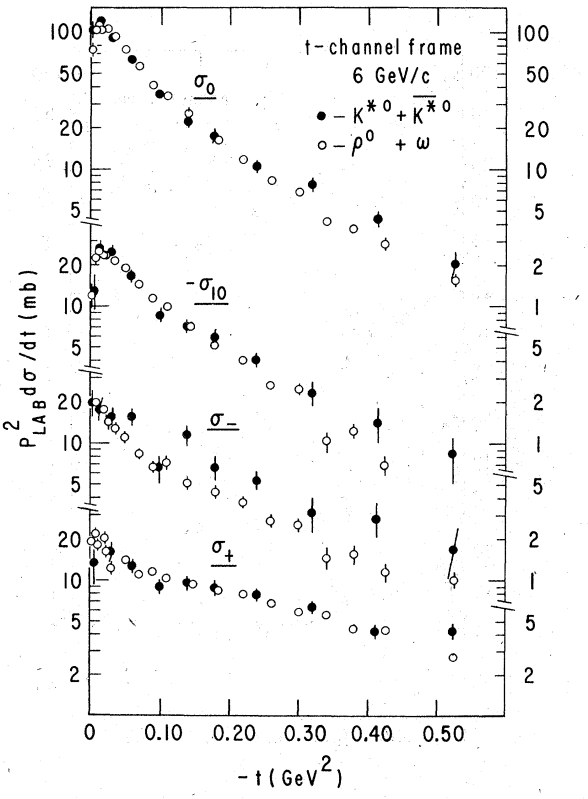

FIG. 38. SU(3) sum-rule comparison at 6 GeV/c in the t-channel frame.

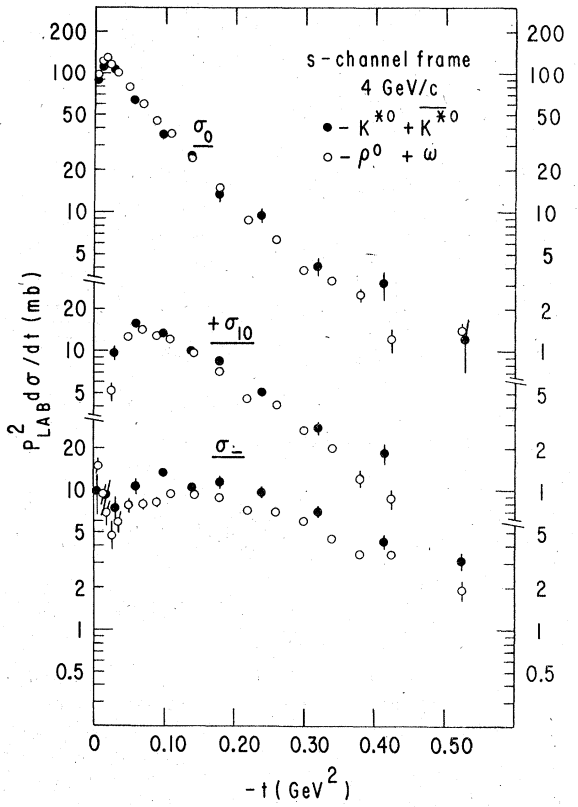

FIG. 39. SU(3) sum-rule comparison at 4 GeV/c in the s-channel frame.

isolate π and B exchanges cleanly. The observable

$$\bar{\sigma}_0(K^*) = \sigma_0(K^*) + \sigma_0(\bar{K}^*) - \sigma_0(\omega) \tag{6.8}$$

eliminates the B-exchange contributions to K^* and $\bar{K}^*$ production, including π-B interference effects, and is predicted to be equal to $\sigma_0(\rho)$ by the SU(3) sum rules. Given the t dependence expected for $\sigma_0(\rho)$ and $\bar{\sigma}_0(K^*)$, SU(3) violation could show up in two ways: (1) The residues of $\sigma_0(\rho)$ and $\bar{\sigma}_0(K^*)$, extrapolated to the pion pole, could be unequal, and (2) the collimation in t, which depends on the absorption strength in the WM model, could be different in the two observables. The intercepts at the pion pole are, of course, constrained by the π-exchange couplings independent of SU(3). Although the pion-nucleon coupling is common to both $\sigma_0(\rho)$ and $\bar{\sigma}_0(K^*)$, the meson-vertex couplings are given by Γ_ρ and Γ_{K^*} and in fact should not satisfy SU(3) exactly.[65] Extrapolated to the pion pole, the π-exchange WM amplitudes given by Eq. (4.2a) stand in the ratio

$$\frac{P_0(K^*)}{P_0(\rho)} = \frac{N(K^*)}{N(\rho)}\,, \tag{6.9}$$

where $N(K^*)$ and $N(\rho)$ are defined by Eq. (3.7).

The π-exchange components of $P_0(K^*)$ and $P_0(\bar{K}^*)$ are of course equal and contribute equally to $\bar{\sigma}_0(K^*)$. To show the approximate dependence on resonance parameters, we can write

$$\frac{N(K^*)}{N(\rho)} \approx \left(\frac{2}{3}\frac{m_{K^*}{}^2\Gamma_{K^*}q(\rho)}{m_\rho{}^2\Gamma_\rho q(K^*)}\right)^{1/2}. \tag{6.10}$$

From the numerical calculations of Sec. IV, the ratio predicted by the WM is $N(K^*)/N(\rho)=0.611$. The SU(3) prediction from Eq. (6.1) is simply $P_0(K^*)/P_0(\rho)=1/\sqrt{2}$, which is larger than the WM prediction by 15%. Thus, a simple WM extrapolation, which should be fairly reliable, predicts unequal intercepts for $\sigma_0(\rho)$ and $\bar{\sigma}_0(K^*)$ at the pion pole.[66]

We have fitted the observables $\sigma_0(\rho)$ and $\bar{\sigma}_0(K^*)$ with the WM parametrization of Eq. (4.2a), namely

$$\frac{\sigma_0(\rho)}{N(\rho)^2}=\left(c(\rho)\frac{\sqrt{-t}}{\mu^2-t}e^{B(\rho)(t-\mu^2)}\right)^2, \tag{6.11a}$$

$$\frac{\bar{\sigma}_0(K^*)}{N(K^*)^2}=\left(c(K^*)\frac{\sqrt{-t}}{\mu^2-t}e^{B(K^*)(t-\mu^2)}\right)^2. \tag{6.11b}$$

The explicit dependence on the meson-vertex couplings has been removed from the observables on the left-hand side of Eq. (6.11). Thus the WM predicts $c(\rho)=c(K^*)=3.84$ mb$^{1/2}$ [Eq. (4.3)]; in addition, SU(3) would predict the collimating factors, $B(K^*)$ and $B(\rho)$, to be equal. The corrected observables, σ_0/N^2, are plotted in Fig. 41 together with results of the fits. A simple average of the 3-, 4-, and 6-GeV/c fitted parameters gives $c(\rho)=3.53\pm0.06$ mb$^{1/2}$, and $c(K^*)=3.66\pm0.11$ mb$^{1/2}$; as noted in Sec. IV, $c(\rho)$ is significantly lower than the WM prediction. The slope parameters indicate that $\bar{\sigma}_0(K^*)$ is somewhat less peripheral in t than $\sigma_0(\rho)$, as can be seen in Fig. 41; a simple average gives $B(\rho)=4.12\pm0.14$ GeV^{-2} and $B(K^*)=3.45\pm0.23$ GeV^{-2}. Although these slope differences are small, they suggest weaker absorption in K^{*0} and $\bar{K}^{*0}$ than in ρ^0 production. Furthermore, the apparent success of the SU(3) sum rules for σ_0 in Figs. 39 and 40 is seen to be partly fortuitous; the K^* and $\bar{K}^*$ cross sections have a smaller intercept than the ρ cross section at $t=\mu^2$, as required by the WM, but this is compensated by a flatter t dependence.

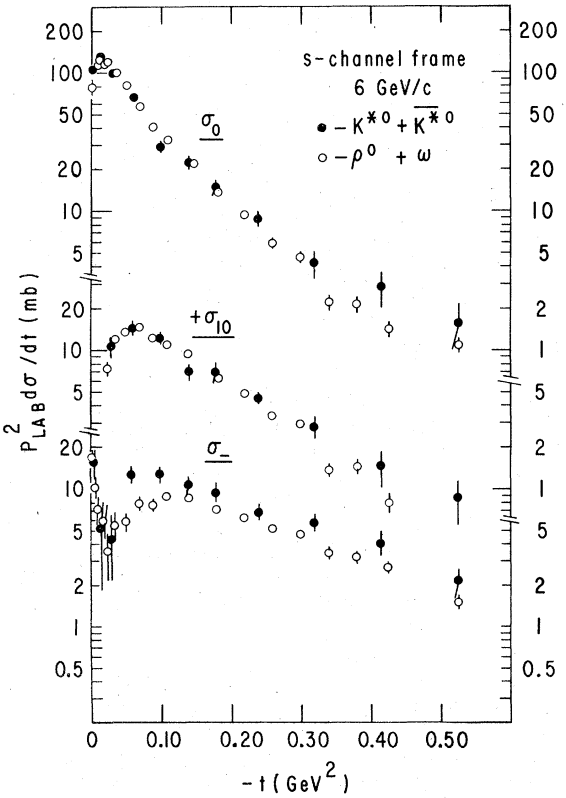

FIG. 40. SU(3)-sum-rule comparison at 6 GeV/c in the s-channel frame.

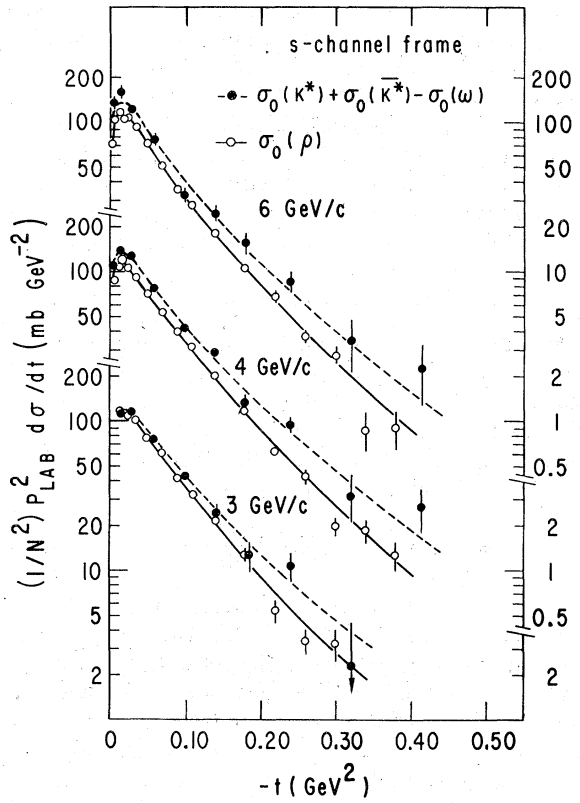

FIG. 41. Comparison of the s-channel helicity-0 cross sections for the observables $\sigma_0(\rho)/N(\rho)^2$ and $[\sigma_0(K^*)+\sigma_0(\bar{K}^*)-\sigma_0(\omega)]/N(K^*)^2$, where $N(\rho)$ and $N(K^*)$ are defined by Eq. (3.7). The curves show the results of our fits to the WM parametrization of Eq. (6.11) over the ranges $-t<0.45$ GeV^2 for 4 and 6 GeV/c and $-t<0.36$ GeV^2 for 3 GeV/c.

We conclude that the SU(3) sum rules are violated in σ_-, and to a much lesser extent in σ_0. These violations can be plausibly explained by hypothesizing weaker absorption in $K^{\pm}N$ than in $\pi^{\pm}N$ reactions. Despite these difficulties, which are responsible for the poor fits to the K^{*0} and $\bar{K}^{*0}$ data obtained in the preceding section, the sum rules work well enough to justify optimism in using SU(3) to explain the $K^*-\bar{K}^*$ difference cross sections.

D. SU(3) comparison of ω-production phases

In addition to fitting the K^* and $\bar{K}^*$ data to obtain a smooth parametrization of the ω-production phases, we have also determined these phases individually in each t bin. From Eq. (6.2b) the ω phases can be deduced from the diagonal dme's, σ_0 and $\sigma_{\pm}$, by means of the relation

$$\cos[\phi_M(\omega)] = \frac{[\sigma_M(K^*)-\sigma_M(\bar{K}^*)]}{2P_M(\rho)|P_M(\omega)|}, \qquad (6.12)$$

where $|P_M(\omega)|$ is given by Table X, and $P_M(\rho)$ (chosen to be real) by Table VII. The phases $\phi_+(\omega)$ and s-channel $\phi_-(\omega)$ and $\phi_0(\omega)$ refer to the flip amplitudes $P^M_{+-}(\omega)$; in the t channel, $\phi_-(\omega)$ and $\phi_0(\omega)$ refer to $P^M_{++}(\omega)$. For consistency, the observables $\sigma_M(K^*)$ and $\sigma_M(\bar{K}^*)$ in Eq. (6.12) were corrected for small s-channel nonflip and t-channel flip contributions, which were parametrized with the model amplitudes of Tables VII and X. The interference cross section, $\mathrm{Re}[\sigma_{10}(K^*,\bar{K}^*)]$, measures $\phi_-(\omega)$ independently via the relation

$$\cos[\phi_-(\omega)-\phi_-(\rho)] = \frac{\sqrt{2}\,[\sigma_{10}(K^*)-\sigma_{10}(\bar{K}^*)]-\mathrm{Re}[P_-(\rho)^*P_0(\omega)]}{|P_0(\rho)||P_-(\omega)|}, \qquad (6.13)$$

where $P_M(\rho)$ and $P_M(\omega)$ are taken from the model, and $\phi_-(\rho)$ is 0° or 180° as in Table VII. Again the K^* and $\bar{K}^*$ observables were corrected for small s-channel nonflip and t-channel flip contributions. As discussed earlier, the quadrant ambiguities in the determinations of $\phi_M(\omega)$ were resolved by appeal to the ρ-ω interference measurements.

Figures 42(a) to 42(c) and 43(a) to 43(c) show the phases determined from the K^* and $\bar{K}^*$ data at 3, 4, and 6 GeV/c, together with smooth curves which represent the fits to the data described in Sec. VIB. The main difference between the t-channel phases in Fig. 42 and the s-channel phases in Fig. 43 occur in $\phi_-(\omega)$, which is essentially reflected about the 180° axis in going from s- to t-channel frames.

For comparison, we have plotted the corresponding phases from the ρ-ω interference data of Table IX in Figs. 42(d) to 42(f) and 43(d) to 43(f). The appropriate ρ^0-production phases (0° or 180°) have been subtracted from the interference measurements in order to expose the ω phases. It was necessary to make small corrections to these measured phases to remove the s-channel nonflip and t-channel flip contributions to the ρ-ω interference observables, again using the model amplitudes. In addition, because the t bins used for the ρ-ω interference data are quite broad, small corrections were made to account for the differences between the (desired) phases at the center of each t bin, and the measured phases, which are averaged over each bin. This correction was substantial only for s-channel σ_- in the bin $-t<0.08$ GeV^2, owing to the

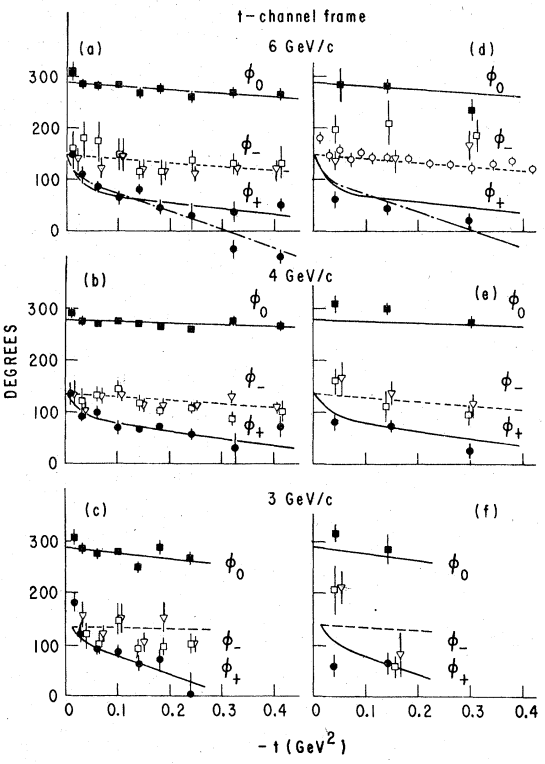

FIG. 42. Comparison of ω-production phases in the t-channel frame. Parts (a), (b), and (c) show the phases resulting from our K^* and $\bar{K}^*$ data at 3, 4, and 6 GeV/c, respectively. Parts (d), (e), and (f) show the corresponding results derived from our ρ-ω interference fits. The solid squares, open points, and solid circles represent φ_0, φ_-, and φ_+, respectively; for φ_-, phases have been determined independently from σ_- (open squares) and $\mathrm{Re}\sigma_{10}$ (open triangles) for both K^*-$\bar{K}^*$ and ρ-ω interference data. For φ_+ at 6 GeV/c and $-t>0.3$ GeV^2, the results of two ambiguous solutions are shown; the open circles in part (d) show φ_- as determined from the $\mathrm{Re}\sigma_{10}(\omega)$ data of Ref. 9. The solid and dashed curves represent the fits to the K^* and $\bar{K}^*$ data with the natural-parity nonflip-to-flip ratio $r_A=0.25$ GeV: the dot-dashed curve for 6-GeV/c φ_+ shows the fit result with $r_A=0.50$ GeV.

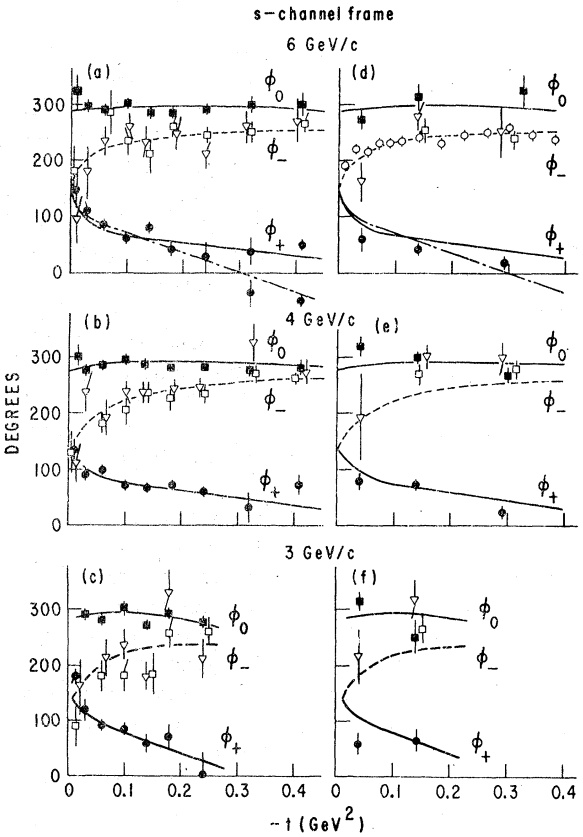

FIG. 43. Comparison of ω-production phases in the s-channel frame. The meanings of the symbols and curves for the various parts are the same as in Fig. 42.

WM crossover zero in $P_-(\rho)$, and consequently these points were omitted from Fig. 43. We have also used Eq. (5.10) to obtain an independent measure of $\phi_-(\omega)$ using the observable $\sigma_{10}(\text{int})$. Specifically, we can define

$$[\phi_-(\omega) - \phi_-(\rho)] = \arg\left[\frac{\sigma_{10}(\text{int})}{\text{Re}\,\sigma_{10}(\rho)} - \frac{\sigma_0(\text{int})}{2\sigma_0(\rho)}\right], \tag{6.14}$$

where the observables on the right-hand side of the equation are the ρ-ω interference quantities from Table IX, corrected for nucleon-spin incoherence and finite t-bin effects.

A third measure of the ω-production phases is provided by the interference dme, $\text{Re}\,\sigma_{10}(\omega)$ shown in Fig. 30, using the relation

$$\cos[\phi_-(\omega) - \phi_0(\omega)] = \frac{\sqrt{2}\,\text{Re}\,\sigma_{10}(\omega)}{|P_-(\omega)||P_0(\omega)|}. \tag{6.15}$$

The observable $\sigma_{10}(\omega)$ on the right-hand side of Eq. (6.15) was corrected for nucleon-spin incoherence; $|P_-(\omega)|$ and $|P_0(\omega)|$ were taken from Table X, and $\phi_0(\omega)$ was specified by the smooth parametrization of Table X provided by the fits to K^* and $\bar{K}^*$ data. The quadrant ambiguity was again resolved by appeal to the ρ-ω interference data; the phase $\phi_-(\omega)$ from Eq. (6.15) is essentially determined up to a reflection about the imaginary axis [$\phi_0(\omega) \approx 270°$], and only one solution to the quadrant ambiguity is consistent with the interference phases. From Figs. 42(d) and 43(d) it can be seen that the phase $\phi_-(\omega)$ determined from Eq. (6.15) agrees remarkably well with the prediction from the fits to the K^* and $\bar{K}^*$ data.

In Fig. 42(a) we show fits to the $\phi_+(\omega)$ phase at 6 GeV/c using two values of the natural-parity nonflip-to-flip ratio, r_A. With $r_A = 0.25$ GeV as in Table X, the fit requires $\phi_+(\omega) > 0$ for all $-t < 0.5$ GeV^2; this is because a zero in $\phi_+(\omega)$ at smaller $-t$ would maximize the cancellation between $P_+(\rho)$ and $P_+(\omega)$ in $P_+(K^*)$ and cause a severe dip in $\sigma_+(K^*)$, contrary to observation (see Fig. 33). With a larger nonflip cross section given by $r_A = 0.5$ GeV, the fitted phase crosses zero at $-t = 0.3$ GeV^2, causing only a shallow minimum in $\sigma_+(K^*)$. The phases determined from the K^* and $\bar{K}^*$ data in individual t bins are ambiguous with respect to a reflection about the real axis, and are therefore consistent with either fit. The ρ-ω interference phases do not appear to resolve the choice of r_A.

The parametrization of Table X allows a rapid variation in $\phi_+(\omega)$ at small $-t$ in order to satisfy the kinematic constraint, $\phi_+(\omega) = \phi_-(\omega)$ at $t' = 0$. The phases determined from $\sigma_+(K^*, \bar{K}^*)$ in Figs. 42(a) to 42(c) indicate that some rapid variation is required in $\phi_+(\omega)$, since this is needed to give $\sigma_+(K^*) > \sigma_+(\bar{K}^*)$ at $t' = 0$ in Fig. 33. However, some of the rapid variation could occur in $\phi_-(\omega)$ as well, although the $\phi_-(\omega)$ phases from $\text{Re}\,\sigma_{10}(\omega)$ in Fig. 42(d) seem to show a linear t dependence down to very small $-t$. The ρ-ω interference data do not resolve the small $-t$ behavior of $\phi_\pm(\omega)$. However, they do demonstrate that the phase difference $[\phi_+(\omega) - \phi_-(\omega)]$ must vary rapidly at small $-t$ to satisfy the kinematic constraint.

We conclude that the three methods of determining the ω-production phases are reasonably consistent with one another, despite some systematic discrepancies, and lend support to the SU(3) relations between the vector-meson production processes. The phase patterns are quite similar at 3, 4, and 6 GeV/c, although the measurements are relatively poor at the lowest energy. The EXD requirement that $\phi_M(\omega)$ be 90° or 270° is broken for ϕ_+ and ϕ_-, but it is broken in the same way for K^* and $\bar{K}^*$ as for ρ and ω production. The following detailed features of $P_M(\omega)$ can be deduced from the fitted curves in Figs. 42 and 43:

(1) $P_0(\omega)$ has similar phase behavior in both s and t channels, and $\phi_0(\omega)$ is close to the EXD value

of 270°.

(2) For $-t<0.5$ GeV^2, Re$[P_-(\omega)]$ is negative in both s and t channels. Im$[P_-(\omega)]$ is everywhere negative in the t channel but has a zero in the s channel around $-t=0.02$ GeV^2, suggesting an $n=0$ absorptive cut analogous to the WM π cut. (Recall that $|P_\pm(\omega)|$ does not vanish at $t'=0$, from the discussion of Sec. VI A.)

(3) $P_+(\omega)$ has a zero in its real part around $-t=0.05$ GeV^2, again suggesting an absorptive-cut effect as discussed in Sec. VI B. At larger $-t$, $P_+(\omega)$ becomes essentially positive real, that is, antiparallel to $P_+(\rho)$. Note that if A_2 exchange is important at larger $-t$, the phase convention $\phi_+(\rho)=180°$, used for $P_+(\rho)$, probably does not agree with the physical ρ-production phase. However, with our phase convention, the GFQ model[54] prediction would be $\phi_+(\omega)=-90°$, considerably lower than the experimental phases.

E. Comparison with higher-energy data

Figure 44 shows the 17-GeV/c ω-production phases which we have derived from the ρ-ω interference data of Ref. 4, taking the ρ-production phases (0° or 180°) from Table VII. For comparison we display our model phases at 4 GeV/c. We emphasize that the 17-GeV/c data come from the single channel $\pi^-p\to\pi^-\pi^+n$, whereas our ρ-ω interference phases at 3, 4, and 6 GeV/c are obtained by comparison of this reaction with $\pi^+n\to\pi^+\pi^-p$. Where ρ-ω interference effects are small, as in small $-t$ σ_0 and σ_-, reliance on the single-channel mass spectrum could result in systematic errors in the phase determinations. On the other hand, for large $-t$ σ_+ where the effects are much larger, both methods should give equivalent results.

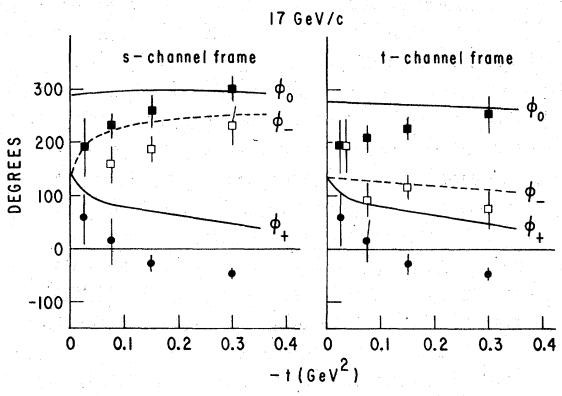

FIG. 44. Comparison of ω-production phases at 17 and 4 GeV/c. The data points for φ_0 (solid squares), φ_- (open squares), and φ_+ (solid circles) were determined from the 17-GeV/c data of Ref. 4. The curves show the results from our model fits at 4 GeV/c.

At small $-t$, $\phi_0(\omega)$ appears to be considerably lower at 17 GeV/c than at 4 GeV/c, and extrapolates to a forward value of about $200°\pm50°$ instead of $290°\pm15°$ as at 4 GeV/c. For $-t>0.2$ GeV^2, where the ρ-ω interference effects are larger, the two energies are quite compatible for both $\phi_0(\omega)$ and $\phi_-(\omega)$. In the forward direction, the $\phi_\pm(\omega)$ intercept is not well determined at 17 GeV/c, but it could be systematically lower than at 4 GeV/c by ~30°. The most significant change from 4 to 17 GeV/c is in the natural-parity phase at large $-t$. At 17 GeV/c, $\phi_+(\omega)$ has a zero around $-t=0.1$ GeV^2 and for larger $-t$ is ~100° lower than at 4 GeV/c. This energy dependence tends to confirm the GFQ-model prediction, namely that $\phi_+(\omega)=-90°$ asymptotically, based on our phase convention in which $\phi_+(\rho)=180°$.

To extrapolate the amplitudes given by our model parametrization to higher energies, we have given $\phi_+(\omega)$ a logarithmic variation with $p_{\rm lab}$ as in Table X, resulting in rough agreement with 17-GeV/c $\phi_+(\omega)$. We have ignored the energy dependence in $\phi_0(\omega)$ and $\phi_-(\omega)$ suggested by the 17-GeV/c data; this may be an oversimplification, but the small $-t$ unnatural-parity ω amplitudes are small enough that this does not affect the predictions of the model significantly. The remaining energy dependences which are incorporated by the parametrization of Tables VII and X are Regge-shrinkage assumed for the ω-production amplitudes and the empirical energy dependence found for the ρ-production amplitudes. The parametrization can be tested against higher-energy $\overline{K}^*$ data.

Figure 45 shows a comparison of s-channel $\overline{K}^*$ production cross sections at 4 and 13 GeV/c,[5] together with our model predictions. The unnatural-parity-exchange cross sections exhibit considerable shrinkage with energy. According to our model, the mechanism for shrinkage in σ_0 is mainly the shrinkage in the ω-production contribution; the shrinkage in σ_-, on the other hand, is caused primarily by the energy dependence of the dominant ρ-production amplitude. The natural-parity cross section exhibits considerable antishrinkage over the entire t range, except for the very forward direction. This behavior is quite different from that observed in ρ production, where antishrinkage in σ_+ is evident only for $-t>0.15$ GeV^2. According to our model, around $-t=0.1$ GeV^2, 75% of the antishrinkage in $\sigma_+(\overline{K}^*)$ is accounted for by the variation of $\phi_+(\omega)-\phi_+(\rho)$ with energy.[67] At larger $-t$ the energy variation is damped because the effective trajectory that describes $P_+(\omega)$ falls with $-t$. Although the descriptions are not satisfactory in the sense of χ^2, the model seems to explain the systematics of the

energy dependence for $\overline{K}^*$ production quite well. Another prediction, which cannot be tested for lack of data, is that $\sigma_+(K^*)$ should fall practically to zero around $-t = 0.1$ GeV^2 at 13 GeV/c, owing to the zero in $\phi_+(\omega)$.

The 13-GeV/c $\overline{K}^*$ data exhibit a feature which we have already observed in the lower-energy data in Sec. VI B, namely that the $n=0$ absorptive cuts, which contribute to ρ and ω production, add constructively in K^* and destructively in $\overline{K}^*$ production. One manifestation of this effect is that, in the forward direction, $\sigma_\pm(K^*) > \sigma_\pm(\overline{K}^*)$. Experimentally, $\sigma_+(K^*) \approx 12$ mb while $\sigma_+(\overline{K}^*) \approx 6$ mb; for comparison, the π-exchange cut contribution alone should result in $\sigma_+(K^*) = \sigma_+(\overline{K}^*) \approx \frac{1}{2}\sigma_+(\rho)$ or $\sigma_+(K^*, \overline{K}^*) \approx 9$ mb. Figure 45 shows that this relative suppression of forward $\sigma_\pm(\overline{K}^*)$ remains true at 13 GeV/c, where $\sigma_+(\overline{K}^*)$ remains around 6 mb in the forward direction.

This mechanism also displaces the WM zeros in s-channel $P^-_{+-}(K^*, \overline{K}^*)$. As noted in Sec. VI B, the zero moves to smaller $-t$ for $\overline{K}^*$ and larger $-t$ for K^* production. Figure 46 shows $\mathrm{Re}\sigma_{10}$ for $\overline{K}^*$ production at 4 and 13 GeV/c,[5] together with our model predictions. For comparison we have also plotted $\mathrm{Re}\sigma_{10}$ for $\pi^- p \to \rho^0 n$ at 17 GeV/c. As noted by the authors of Ref. 5, the zero in $\sigma_{10}(\overline{K}^*)$ is displaced toward smaller $-t$ as compared with the WM prediction, $-t_c = \mu^2$, which is indicated by the arrows in Fig. 46; the WM prediction is, of course, satisfied by $\sigma_{10}(\rho)$. Figure 46 also displays our model prediction for $\sigma_{10}(K^*)$ at 13 GeV/c, in which the WM zero is displaced to larger $-t$.

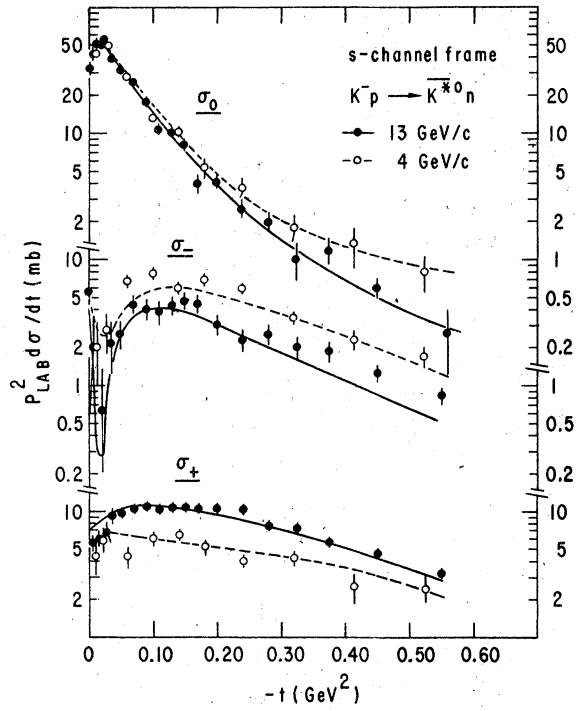

FIG. 45. Comparison of $\overline{K}^*$ production cross sections at 4 and 13 GeV/c in the s-channel frame. The 13-GeV/c data (solid points) are from Ref. 5 and the 4-GeV/c data (open circles) are from this experiment. The curves show our model predictions at 4 GeV/c (dashed curves) and 13 GeV/c (solid curves). The quantities plotted are $\sigma_M = p_{1ab}{}^2 \rho_M d\sigma/dt$.

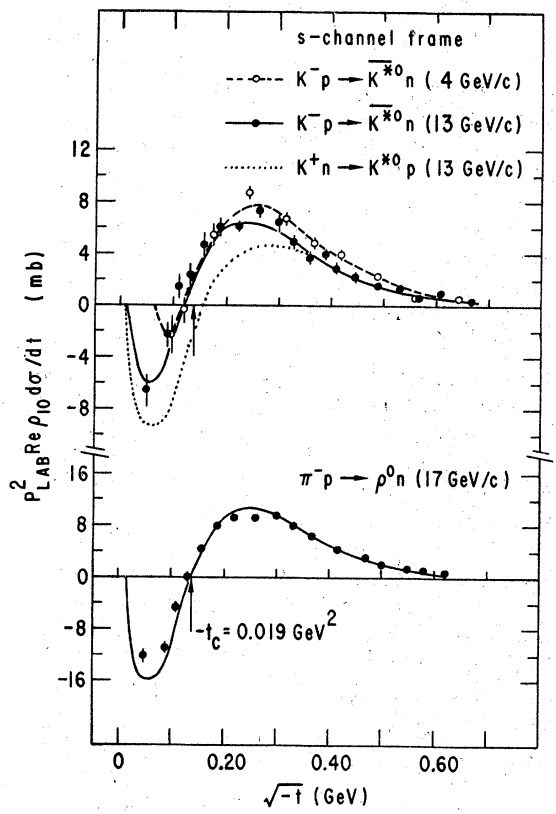

FIG. 46. Comparison of the interference cross sections, $p_{1ab}{}^2 \mathrm{Re}\rho_{10} d\sigma/dt$, for K^* and $\overline{K}^*$ production at 4 and 13 GeV/c in the s-channel frame. The solid points show the 13-GeV/c $\overline{K}^*$ data of Ref. 5; our model prediction for this cross section is shown by the solid curve. The 4/GeV/c data of this experiment and our model fit are shown by the open points and dashed curve. Our model prediction for 13-GeV/c K^* production is shown by the dotted curve. The lower part of the figure shows the 17-GeV/c ρ^0-production data of Ref. 4 together with our model prediction. The crossover-zero location predicted by the WM, $-t_c = \mu^2$, is indicated by the arrows.

We conclude that our amplitude parametrization adequately correlates the energy dependence observed in ρ production, ρ-ω interference, and $\overline{K}^*$ production. In addition, the 13-GeV/c $\overline{K}^*$ data confirm an important systematic feature of the

lower-energy data, namely that the small $-t$ $n=0$ cut amplitude is larger for K^* than for $\overline{K}^*$ production, reflecting the constructive (destructive) interference between the ρ and ω amplitudes in the K^* ($\overline{K}^*$) channel.

F. Interpretation of the vector-meson amplitudes

The vector-meson production amplitudes can be understood most economically within the framework of Regge poles and absorptive cuts. In this section we will concentrate on the qualitative interpretation of the production phases in terms of a simple pole and cut structure (π, B, ρ, and A_2 exchanges). A similar approach was taken by Estabrooks and Martin[60]; although their analysis was based on a more limited set of data, their model amplitudes and their conclusions are consistent with our own. A more ambitious task, the comparison of a spectrum of theoretical models with vector-meson production data, has already been carried out by Field and Sidhu.[49] None of the models which they considered could successfully fit the data available at the time (including the 4-GeV/c ρ-ω interference data from this experiment). However, the model of Hartley and Kane[68] (model 1b in Ref. 49, hereafter denoted as HK) appeared to be the most promising of the alternatives, and where possible we will compare the features of our empirical amplitudes with the HK-model predictions, as given in Ref. 49.

For our qualitative analysis of vector-meson production, we will assume that the pole amplitudes have Regge phases, and that the cut amplitudes are 180° out of phase with the poles. In "realistic" absorption models, the absorptive cuts are generally taken to be more than 180° out of phase with the pole amplitudes, measured counterclockwise in the complex plane. For example, for the $n=0$ π cut at small $-t$, the HK model predicts a phase difference $[\phi_{\text{cut}} - \phi_{\text{pole}}] \approx 215°$. As a consequence, the phase difference between $P_-(\rho)$ and $P_0(\rho)$ in the s channel is predicted by the HK model to be $[\phi_-(\rho) - \phi_0(\rho)] \approx -30°$ at $-t = 0.1$ GeV^2. Such a large phase difference is inconsistent with the amplitude analysis of Sec. IV; a 30° phase difference would result in a large $P_-^\perp$ component, namely $|P_-^\perp|^2/|P_-^\parallel|^2 \approx \frac{1}{3}$, which does not agree with the data shown in Fig. 23. The HK model phase difference would be reduced if a flatter π trajectory were used in the Field and Sidhu calculation (they used $\alpha_\pi' = 0.5$ GeV^2), and such a choice would be more consistent with the energy dependence of s-channel $\sigma_0(\rho)$. In this connection, it is noteworthy that none of the models considered by Field and Sidhu explain the energy dependence of $\sigma_+(\rho)$. In particular, the shrinkage predicted by the HK model for the cut amplitude $P_\pm(\rho)$ at $t'=0$ is not observed in the data, as noted in Sec. IV.

We now summarize the main features of the ρ- and ω-production amplitudes derived from our fits, using our simplified Regge description as a guide, and comparing with the HK-model predictions. We will consider only the s-channel-flip amplitudes $P_\pm$ and P_0 and the t-channel-nonflip amplitudes P_- and P_0.

π- and B-exchange pole amplitudes. The s-channel $P_0(\rho, \omega)$ amplitudes are presumably dominated by π and B exchanges at small $-t$ [Fig. 47(a)], and the orientations of $P_0(\rho, \omega)$ in the complex plane [Fig. 47(b)] agree qualitatively with

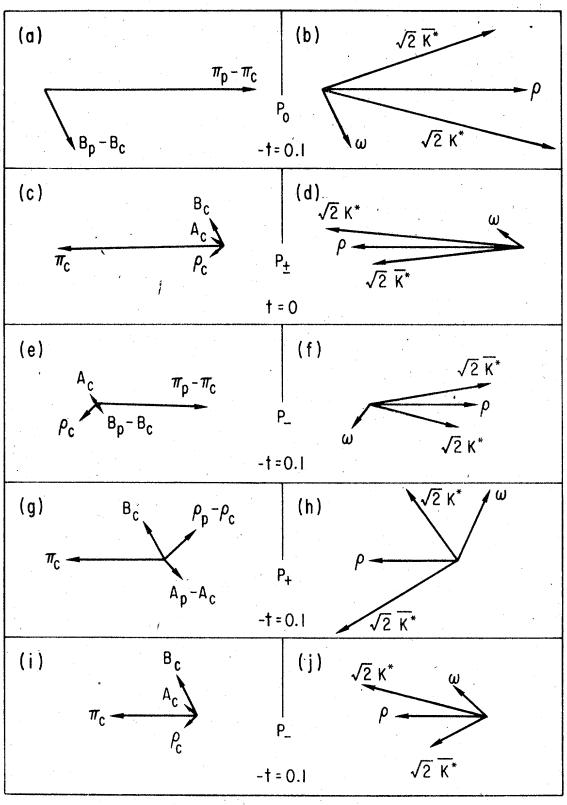

FIG. 47. Schematic representation of the results of our amplitude analysis, showing the relative orientations and magnitudes of the amplitudes in the complex plane. Parts (a) through (h) are in the s-channel frame; parts (i) and (j) are in the t-channel frame. The amplitude component and t value (in GeV^2) for each part is labeled in the figure. The left-hand diagrams show the pole (p) and cut (c) contributions to the ρ- and ω-production amplitudes from π, B, ρ, and $A_2(A)$ exchange; the right-hand diagrams show the resultant ρ-, ω-, K^{*0}-, and $\overline{K}^{*0}$-production amplitudes. The vectors in the right-hand diagrams have been rotated, relative to those on the left, to conform to our phase convention that the ρ-production amplitudes be real.

EXD requirements as in the GFQ model.[54] Note that $P_0(\omega)$ and $P_0(\rho)$ are not precisely 90° out of phase, but rather $\phi_0(\omega) \approx -70°$ on the average in the s channel. The HK model, with our phase convention for $P_0(\rho)$, predicts $\phi_0(\omega) \approx -120°$ at small $-t$; this phase is associated mainly with the rotation of the B-exchange pole induced by absorption. Thus the HK model predicts $\sigma_0(K^*) < \sigma_0(\overline{K}^*)$ in the s channel, in contradiction with the data of Fig. 31. The empirical value of the $\phi_0(\omega)$ phase could be explained by postulating that the B trajectory is lower than the π trajectory, namely $\alpha_B(0) \approx -0.2$. Kane and Seidl[32] have recommended the choice $\alpha_B(0) = +0.21$; inserted into the HK-model calculation, this value would result in relatively worse agreement with the experimental $\phi_0(\omega)$ phase and the K^*-$\overline{K}^*$ cross-section difference.

π- and B-exchange cut amplitudes. The approximate orientations of the strong $n=0$ π and B cuts at $t=0$ are shown in Fig. 47(c). Their phases are chosen to provide destructive interference with the s-channel $P_-(\rho,\omega)$ pole amplitudes, and as noted above, would be rotated by about 35° counterclockwise in the HK model.

ρ- and A_2-exchange phases. The Regge phases of the ρ and A_2 poles are prescribed by the signature factors. At small $-t$, the ρ-pole phase can be ≈45° and ≈225° depending on the signs of the coupling constants. The 45° choice is the only one consistent with measured $\phi_+(\omega)$, assuming that the phase of $P_+(\rho)$ is close to 180°.

The A_2 Regge-pole phase can lie in the second or fourth quadrants at small $-t$. Two facts resolve the ambiguity in favor of the fourth quadrant. First, the 17-GeV/c ρ-ω interference phase at large $-t$ requires $\phi_+(\rho) \approx \phi_+(\omega) - 90°$. Second, as argued in Sec. IV, the energy dependence of $\sigma_+(\rho)$ requires destructive interference between the π cut and the A_2 pole in $P_+(\rho)$; taking the $n=0$ π-cut phase to be near 180°, the A_2 pole must have a positive real part. With these phase assignments, the ρ- and A_2-pole phases are consistent with duality as in the GFQ model. Added constructively, they contribute mainly to the real part of $P_+(K^*)$.

$n=0$ forward cuts. Knowing the ρ- and A_2-pole phases, we can introduce ρ- and A_2-exchange $n=0$ cuts as in Fig. 47(c); again, these would be rotated by about 35° counterclockwise in the HK model. The resulting $n=0$ forward amplitudes for ρ, ω, K^*, and $\overline{K}^*$ production, shown in Fig. 47(d), exhibit the systematics which we emphasized earlier, namely that the $n=0$ cut is larger for K^* than for $\overline{K}^*$, and the forward $P_\pm(\omega)$ phase is around 135°.

Zero structure. Zeros in s-channel P_- occur in our empirical amplitudes for both ρ and ω production. Figure 47(e) shows the exchange contributions to $P_-(\rho,\omega)$ at $-t=0.1$ GeV^2, where the π and B poles dominate over the $n=0$ π and B cuts. The resulting orientations of $P_-(\rho,\omega,K^*,\overline{K}^*)$ at $-t=0.1$ GeV^2 are depicted in Fig. 47(f). By comparison of the $t=0$ amplitudes [Fig. 47(d)] with the $-t=0.1$-GeV^2 amplitudes [Fig. 47(f)], we see that $\mathrm{Re}[P_-(\rho)]$ and $\mathrm{Im}[P_-(\omega)]$ both have zeros between $t=0$ and $-t=0.1$ GeV^2. By contrast, $\mathrm{Re}[P_-(\omega)]$ has no zero because of the ρ-cut contribution; similarly $\mathrm{Im}[P_-(\rho)]$, while very small, is also expected to have no zero. We have previously pointed out that $\mathrm{Re}[P_+(\omega)]$ must have a zero at $-t \approx 0.05$ GeV^2 in order to explain the zero in the difference $[\sigma_+(K^*) - \sigma_+(\overline{K}^*)]$. The mechanism for this crossover zero lies in the behavior of the ρ-exchange amplitude. Figure 47(g) shows the exchange contributions to $P_+(\rho,\omega)$ at $-t=0.1$ GeV^2, where ρ- and A_2-pole terms dominate over the $n=0$ ρ and A_2 cuts. Figure 47(h) shows the resulting orientations of $P_+(\rho,\omega,K^*,\overline{K}^*)$ at $-t=0.1$ GeV^2. Again, by comparison with the $t=0$ amplitudes of Fig. 47(d), we see that $\mathrm{Re}[P_+(\omega)]$ must have a zero at small $-t$; however, the B-cut contribution keeps $\mathrm{Im}[P_+(\omega)]$ positive for all t.

t-channel phases. The phases of $P_0(\rho,\omega)$ in the t channel are similar to the s-channel phases shown in Fig. 47(b). The t-channel amplitudes $P_-(\rho,\omega)$ are given by the cut contributions depicted in Fig. 47(i). The resulting vector-meson production amplitudes are oriented as in Fig. 47(j); the line-reversal breaking, $\sigma_-(K^*) > \sigma_-(\overline{K}^*)$, is due to the constructive interference between the π cut and the $\rho+B$ cut in the t channel. $P_-(\omega)$ maintains a nearly constant phase in the t channel, $\phi_-(\omega) \approx 130°$.

$P_\pm$ phases at large $-t$. The relative orientations of the different vector-meson production amplitudes change slowly with t, and so the essential features of the $-t=0.1$-GeV^2 s-channel amplitudes, shown in Figs. 47(f) and 47(h), persist to larger $-t$. At $-t=0.1$ GeV^2, the HK model predicts the s-channel phase $\phi_-(\omega)$ to be −70°, whereas experimentally $\phi_-(\omega) \approx -130°$. The origin of the HK prediction lies in the counterclockwise rotation predicted for the $n=0$ cuts; because of the HK cut phases, $P_-(\rho)$ is rotated clockwise and $P_-(\omega)$ counterclockwise as compared with Fig. 47(f). As a result, the HK model predicts $\sigma_-(K^*) > \sigma_-(\overline{K}^*)$, in the s channel; in particular, at $-t=0.4$ GeV^2, the HK prediction gives $\sigma_-(K^*) \approx 3\sigma_-(\overline{K}^*)$, which is in serious disagreement with the data of Fig. 34.

The HK model predicts $\phi_+(\omega) = -45°$ at $-t=0.1$ GeV^2, with our $P_+(\rho)$ phase convention, whereas experimentally $\phi_+(\omega) = +70°$. Again, part of the discrepancy can be attributed to the absorptive-cut phases; the HK $n=0$ cuts are rotated counter-

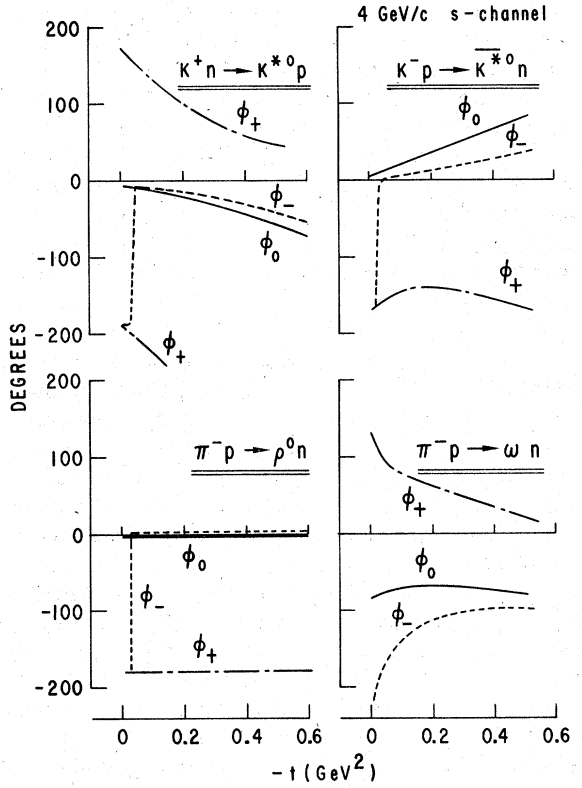

FIG. 48. Momentum-transfer dependence of the vector-meson production amplitude phases, as determined from our amplitude analysis at 4 GeV/c in the s-channel frame. φ_0 is shown by the solid curves, φ_+ by the dot-dashed curves, and φ_- by the dashed curves. The ρ-production amplitudes are taken to be real, as shown in the figure.

clockwise compared with Fig. 47(c), resulting in a counterclockwise rotation of $P_+(\rho)$ and a clockwise rotation of $P_+(\omega)$ relative to the orientation shown in Fig. 47(h). In addition, part of the discrepancy apparently lies in an overestimate of the importance of the A_2-exchange contribution in the HK-model fits. As can be seen from Fig. 47(g), in the limit that the ρ- and A_2-exchange components become dominant (large s and large $-t$), the relative phase $\phi_+(\omega) - \phi_+(\rho)$ should approach $+90°$, instead of $-110°$ as in Fig. 47(h).

K^*-production phases and exchange degeneracy. If the absorbed Regge-pole amplitudes satisfied duality, then the amplitudes for $K^+n \to K^{*0}p$ would be purely real. We cannot test for such behavior directly, since the overall phases of the natural- and unnatural-parity amplitudes are not determined experimentally, and we have simply chosen the ρ-production amplitudes to be real. The model phases of the four vector-meson production amplitudes at 4 GeV/c in the s channel are shown in Fig. 48. The unnatural-parity K^*-production phases ϕ_- and ϕ_0 differ from one another by less than 10° over the t range, whereas in $\overline{K}^*$ production these phases differ by ≈40° at $-t = 0.5$ GeV^2. If P_0 for ρ production were assigned a Regge phase consistent with $\alpha_\pi(t) = t - \mu^2$, then both the ϕ_- and ϕ_0 phases for K^* production would remain close to 0° over the t range. However, the lack of shrinkage in s-channel $P_0(\rho)$ casts doubt on this interpretation. We emphasize that the phase difference, $\phi_-(K^*) - \phi_0(K^*)$, is not well determined experimentally; it depends on the constraint which was imposed in our fits that $P_-(\rho)$ and $P_0(\rho)$ be relatively real. If we allowed a modest clockwise rotation of $P_-(\rho)$ with respect to $P_0(\rho)$ [i.e., in the sense prescribed by the HK model, but consistent with measured $P_-^\perp(\rho)$], then $\phi_-(K^*)$ and $\phi_-(\overline{K}^*)$ would both decrease in Fig. 48. The HK model predicts substantial phase differences between $P_-(K^*)$ and $P_0(K^*)$ over the entire t range.

The natural-parity K^* phase falls rapidly with increasing $-t$. We could arrange for $P_+(K^*)$ to be purely real only if $\phi_+(\rho)$ increased by about 140° between $t = 0$ and $-t = 0.5$ GeV^2. This increase is rather large in magnitude, but is in the same sense as expected [see Fig. 47(g)]; $P_+(\rho)$ should rotate counterclockwise as $-t$ increases. Again, in the HK model the $P_+(K^*)$ amplitude is far from being purely real.

Thus it appears that the K^* production amplitudes could be made to be approximately real provided that the π-exchange pole is assigned a Regge phase and that $P_+(\rho)$ rotates rapidly. Although the vector-meson production phases may satisfy duality in this sense, the EXD prediction fails for the magnitudes of the K^* and $\overline{K}^*$ observables. The spectacular difference between $\sigma_+(K^*)$ and $\sigma_+(\overline{K}^*)$ is explained by the Fox mechanism,[59] which is evident in Figs. 47(g) and 47(h); the interference between the ρ pole and the π cut is destructive for $P_+(K^*)$ and constructive for $P_+(\overline{K}^*)$.

We conclude that, with a simplified description using π, B, ρ, and A_2 poles and cuts, we can account for the essential features of the vector-meson production amplitudes, namely the systematics of the $n = 0$ cut amplitudes at $t = 0$, where $P_\pm(K^*) > P_\pm(\overline{K}^*)$, the zeros in s-channel $\mathrm{Re}[P_+(\omega)]$, $\mathrm{Im}[P_-(\omega)]$, and $\mathrm{Re}[P_-(\rho)]$ at very small $-t$, and the systematics of line-reversal breaking associated with the relative ρ- and ω-production phases at larger $-t$, where $\sigma_0(K^*) > \sigma_0(\overline{K}^*)$, and $\sigma_\pm(K^*) < \sigma_\pm(\overline{K}^*)$ in the s channel. The Hartley-Kane model, as calculated by Field and Sidhu, does not correctly predict the relative ρ and ω phases in any of the amplitudes, and consequently fails to describe the line-reversal breaking in $\sigma_0(K^*, \overline{K}^*)$ and $\sigma_-(K^*, \overline{K}^*)$; it also fails to explain the energy dependence of the ρ-production amplitudes, in par-

ticular, the $n=0$ amplitude at $t'=0$, and $P_+(\rho)$ at larger $-t$. We point out, however, that some of the detailed predictions of the HK model could be altered by changing the coupling constants and trajectories used by Field and Sidhu.

VII. CONCLUSIONS

We have presented new data on forward vector-meson production in the reactions $\pi^- p \to \rho^0 n$, $\pi^+ n \to \rho^0 p$, $K^+ n \to K^{*0} p$, and $K^- p \to \bar{K}^{*0} n$ at 3, 4, and 6 GeV/c. The properties of the P-wave Breit-Wigner and S-wave background amplitudes have been investigated for the $\pi^+\pi^-$, $K^+\pi^-$, and $K^-\pi^+$ systems, and these are summarized in Tables III and IV. The P-wave dipion-production amplitudes are observed to vary more rapidly with mass than would be expected on the basis of simple absorption models, suggesting that the absorption strength decreases systematically with increasing mass. The vector-meson production observables, averaged over mass, are given in Table V as functions of momentum transfer. We call attention to the fact that the cross sections in Table V, to which we refer in the following paragraphs, are scaled by the factor $p_{\rm lab}{}^2$ to show better the energy dependence of the production amplitudes.

In the same experiment we have detected ρ-ω interference by comparing the reactions $\pi^- p \to \pi^-\pi^+ n$ and $\pi^+ n \to \pi^+\pi^- p$. The magnitudes and relative phases of the ρ-ω interference contributions are given for each P-wave observable in Table IX. Using a model to parametrize the nucleon-spin dependence, we find a branching ratio for $(\omega \to \pi^+\pi^-)/(\omega \to \text{all})$ of $(1.0 \pm 0.1)\%$.

We have examined the energy dependence of the reaction $\pi^- p \to \rho^0 n$ from 3 to 17 GeV/c in order to better understand the dominant π-exchange contribution to this process. We find the following systematics:

(1) The differential cross sections for both the $\pi\pi$ S wave and for the helicity-0 P wave in the s channel exhibit little shrinkage with energy; a consistent slope for the π Regge trajectory would be $\alpha_\pi' = 0.30 \pm 0.04$ GeV^{-2}.

(2) For helicity-1 ρ^0 production, the unnatural-parity-exchange cross section, scaled by $p_{\rm lab}{}^2$, falls rapidly with energy in the s channel. Part of this energy dependence is caused by the nucleon-nonflip cross section at small $-t$, which gives a contribution proportional to $t_{\rm min}$, and which drastically affects the interpretation of the unnatural-parity observables at the lower energies. The dominant nucleon-flip amplitude also falls with energy at larger $-t$, and it is possible that this effect can be explained by cuts associated with A_2 exchange.

(3) Absorption strength in the net-helicity-flip $n=0$ amplitude agrees fairly well with the Williams model[28] near the forward direction. In particular, the locations of the zero near $-t \approx \mu^2$ in the unnatural-parity amplitude, caused by cancellation of the π pole and its absorptive cut, agrees with the WM prediction fairly well at all energies. However, for $-t > 0.05$ GeV^2 the absorption prediction by the WM is too large to agree with the 3- to 6-GeV/c data on $\sigma_+(\rho)$ and $\sigma_-(\rho)$. The fact that this model appears to describe 15- and 17-GeV/c ρ^0-production data[2,3] for $-t < 0.2$ GeV^2 is presumably an accident resulting from A_2-exchange effects.

(4) At $t'=0$, $\sigma_\pm(\rho)$ is consistent with being energy independent. This behavior agrees with the WM but disagrees with the Kane-Seidl model,[32] which predicts a falloff, $\sigma_\pm(\rho) \propto p_{\rm lab}{}^{-0.26}$, at $t'=0$.

(5) For $-t > 0.15$ GeV^2, the natural-parity ρ^0 production cross section exhibits strong antishrinkage with energy. To explain this energy dependence requires not only the conventional A_2 Regge-pole contribution, but also destructive interference between A_2 exchange and a shrinking π-exchange absorptive cut.

The K^{*0} and $\bar{K}^{*0}$ production cross sections are presumably also dominated by π exchange at small $-t$. However, the K^{*0} and $\bar{K}^{*0}$ observables show large systematic differences, especially in the helicity-1 cross sections, which demonstrates interference between even- and odd-G-parity-exchange amplitudes. We have examined in detail the relation between $G=\pm 1$ exchange amplitudes in K^* and $\bar{K}^*$ production and the SU(3)-related amplitudes that describe ρ and ω production. By testing sum rules for the vector-meson production observables, and by comparing the K^*-$\bar{K}^*$ cross-section differences with corresponding ρ-ω interference cross sections we conclude that SU(3) is reasonably successful in relating K^*, $\bar{K}^*$, ρ, and ω production amplitudes. The systematic SU(3) breaking which is observed in the sum rules can be plausibly ascribed to weaker absorptive rescattering in K^* and $\bar{K}^*$ than in ρ and ω production.

In order to test the SU(3) predictions, we have derived the relative phases of the even- and odd-G-parity-exchange amplitudes from three sources: the K^* and $\bar{K}^*$ observables, the ρ-ω interference data, and the $\pi^- p \to \omega n$ observables. The phases so determined are mutually consistent and can be summarized in an SU(3)-symmetric parametrization of the $G=\pm 1$ exchange amplitudes. This parametrization is also reasonably successful in describing the main features of 13-GeV/c $\bar{K}^*$ production[5] and 17-GeV/c ρ-ω interference data.[4]

The systematic features of the even- and odd-G-parity exchange amplitudes can be understood qual-

itatively in the framework of strongly absorbed π, A_2, B, and ρ exchange Regge poles. The phases of the pole contributions agree qualitatively with EXD predictions; π and B poles are about 70° out of phase in the s channel, and the contribution of their imaginary components would tend to cancel in K^* production, if the π were assigned a Regge phase. The ρ- and A_2-exchange components also appear to contribute mainly to the real parts of the K^* amplitudes.

The importance of absorptive cuts in the $n=0$ amplitudes is evidenced by the nonvanishing forward cross sections in the helicity-1 states for ρ, ω, K^*, and $\overline{K}^*$ production. Related evidence for pole-cut cancellations is given by the zeros in the s-channel helicity-1 amplitudes at small $-t$. Our parametrization of the vector-meson production phases indicates the existence of these zeros in the following amplitudes: (1) $P_-(\rho)$, due to the $n=0$ π cut, (2) $\mathrm{Im}[P_-(\omega)]$, due to cancellation between the B pole and the B cut, and (3) $\mathrm{Re}[P_+(\omega)]$, due to ρ-pole–ρ-cut cancellation. The zeros in $P_-(\rho)$ and $\mathrm{Re}[P_+(\omega)]$ can be detected directly in the observables, specifically in $\mathrm{Re}[\sigma_{10}(\rho)]$, and in the difference cross section $\sigma_+(K^*)-\sigma_+(\overline{K}^*)$.

The EXD-breaking effects which are observed in both the K^* and $\overline{K}^*$ observables and in the ρ-ω interference phases apparently arise both from the non-EXD phases of the π- and B-pole amplitudes, and from the interference of opposite-naturality contributions induced by absorption. For example, the line-reversal breaking in the s-channel helicity-0 amplitudes, $\sigma_0(K^*)>\sigma_0(\overline{K}^*)$, is correlated with the non-EXD relative phase $\phi_0(\omega)-\phi_0(\rho)\approx -70°$. At $t'=0$, the $n=0$ cuts can receive contributions from π, B, ρ, and A_2 exchange, and the Regge-pole phases are such that the resultant $n=0$ amplitude is stronger in K^* than in $\overline{K}^*$ production. This results in the following features: (1) $\sigma_\pm(K^*)>\sigma_\pm(\overline{K}^*)$ at $t'=0$, (2) $\sigma_-(K^*)>\sigma_-(\overline{K}^*)$ in the t channel, and (3) the s-channel WM zero in $P_-(K^*)$ is displaced to larger $-t$ as compared with $P_-(\overline{K}^*)$. At larger $-t$, line-reversal breaking is caused by the interference of pole and cut contributions from opposite naturality exchanges. The most dramatic manifestation of this mechanism is the large difference observed between $\sigma_+(K^*)$ and $\sigma_+(\overline{K}^*)$; for $-t>0.1$ GeV^2, $\sigma_+(K^*)\ll\sigma_+(\overline{K}^*)$, presumably because of the interference between ρ-pole and π-cut contributions. At much higher energies, the equality of $\sigma_+(K^*)$ and $\sigma_+(\overline{K}^*)$ is expected to be restored, at least at large $-t$, owing to the dominance of ρ and A_2 exchanges. The approach to this domain is signaled by the rapid energy dependence of both $\sigma_+(\overline{K}^*)$ and the natural-parity ρ-ω interference phase between 4 and 17 GeV/c.

ACKNOWLEDGMENTS

We thank R. Diaz, J. Falout, L. Filips, and E. Walschon for help in the design, construction, and operation of the effective-mass spectrometer, and R. Ely and C. Klindworth for assistance with the on-line computer system. We are indebted to R. Klem, R. Guigler, A. Passi, W. Siljander, and other members of the Accelerator Research Facilities Division for their help in the construction and operation of the beam line and the target facility. We thank the ZGS operating staff for providing the stable and reliable proton beam. We are particularly grateful to I. Ambats, A. Lesnik, D. R. Rust, C. E. W. Ward, and D. D. Yovanovitch, who collaborated in the design and construction of the apparatus and in the early stages of data taking. We have benefited especially from discussions with R. D. Field, P. Estabrooks, A. D. Martin, and A. Irving. We thank G. Farmelo for valuable discussions and an initial reading of the manuscript, W. Männer for providing us with the data reported in Ref. 3, and M. Shaevitz for supplying the data of Ref. 9. Finally we acknowledge the encouragement and support provided by B. Cork, T. Fields, and M. Derrick throughout this work. This work was performed under the auspices of the U. S. Energy Research and Development Administration.

---

*Present address: Fermi National Accelerator Laboratory, Batavia, Illinois 60510.

[1]S. L. Kramer *et al.*, Phys. Rev. Lett. 33, 505 (1974).

[2]P. Baillon *et al.*, Phys. Lett. 35B, 453 (1971) [for data, see also F. Bulos *et al.*, Phys. Rev. Lett. 26, 1453 (1971)].

[3]G. Grayer *et al.*, Nucl. Phys. B75, 189 (1974).

[4]P. Estabrooks *et al.*, Nucl. Phys. B81, 70 (1974).

[5]G. W. Brandenburg *et al.*, Phys. Lett. 59B, 405 (1975).

[6]$K^+n\to K^{*0}p$: R. Poster, Ph.D. thesis, UCLA Report No. UCLA-1095, 1973 (unpublished) (1.94 GeV/c); S. Goldhaber *et al.*, Phys. Rev. Lett. 15, 737 (1965) (2.3 GeV/c); G. Bassompierre *et al.*, Nucl. Phys. B16, 125 (1970) (3 GeV/c); K. Buchner *et al.*, *ibid.* B45, 333 (1972) (4.6 GeV/c); D. Cords *et al.*, Phys. Rev. D 4, 1974 (1971) (9 GeV/c), A. Firestone *et al.*, *ibid.* 5, 2188 (1972) (12 GeV/c). $K^-p\to\overline{K}^{*0}n$: M. Dickerson *et al.*, Phys. Lett. 23, 505 (1966) (2 GeV/c); D. Chu, Ph.D. thesis, Cal. Inst. of Tech., 1972 (unpublished) (2 GeV/c); J. Goldberg *et al.*, Phys. Lett. 30B, 434 (1969) (3 GeV/c); A. Verglas *et al.*, Nuovo Cimento 41, 629 (1966) (3 GeV/c); N. A. McCubbin and L. Lyons, Nucl. Phys. B86, 13 (1975) (3.6 GeV/c); M. Anguilar-Benitez *et al.*, Phys. Rev. D 4, 2583 (1971) (3.9, 4.6 GeV/c); F.L. Schweingruber *et al.*, Phys. Rev. 166, 1317 (1968) (4.1 GeV/c); Y. W. Kang, *ibid.* 176, 1587 (1968) (4.57 GeV/c); R. Engelmann *et al.*, Phys. Rev. D 5, 2162 (1972) (5.5 GeV/c);

M. Aderholz *et al.*, Nucl. Phys. B7, 111 (1968) (10.1 GeV/c); M. Deutschmann *et al.*, *ibid.* B36, 373 (1972) (10 GeV/c); M. Deutschmann *et al.*, *ibid.* B81, 1 (1974) (16 GeV/c).

[7]See G. C. Fox *et al.*, Phys. Rev. D 4, 2647 (1971); in fits to K^* and $\overline{K}^*$ production, normalization correction factors ranging from 0.63 to 1.88 were needed to obtain smooth fits from the experimental cross sections.

[8]D. S. Ayres *et al.*, Phys. Rev. Lett. 32, 1463 (1974); D. Cohen *et al.*, *ibid.* 38, 269 (1977).

[9]M. H. Shaevitz *et al.*, Phys. Rev. Lett. 36, 8 (1976).

[10]M. J. Emms *et al.*, Nucl. Phys. B98, 1 (1975).

[11]H. J. Lipkin, Nucl. Phys. B7, 321 (1968).

[12]I. Ambats *et al.*, Phys. Rev. D 9, 1179 (1974).

[13]D. S. Ayres, in *Proceedings of the International Conference on Instrumentation for High Energy Physics, Frascati, Italy, 1973,* edited by S. Stipcich (Laboratori Nazionali del Comitato Nazionale per l'Energia Nucleare, Frascati, Italy, 1973), p. 665.

[14]A. B. Wicklund *et al.*, Argonne Technical Note, 1971 (unpublished).

[15]A. J. Pawlicki *et al.*, Phys. Rev. D 12, 631 (1975).

[16]The angles θ and ϕ are, respectively, the polar and azimuthal angles that characterize the directions of the final state π^- in reaction (1.1), the π^+ in reaction (1.2), the K^- in reaction (1.3), and the K^+ in reaction (1.4), as seen in the $\pi\pi$ or $K\pi$ center-of-mass frame. The y axis is defined to be parallel to the overall production normal specified by the vector product $\vec{p}_{\rm beam} \times \vec{p}_{\pi\pi,\,K\pi}$ ($\vec{p}_{\rm beam}$ denotes the beam momentum and $\vec{p}_{\pi\pi}$, $\vec{p}_{K\pi}$ denote the three-momentum vectors of the final state $\pi\pi$ or $K\pi$ systems). The z axis is defined as opposite to the recoil-nucleon direction in the s-channel frame, and along the incident-beam direction in the t-channel frame, as seen in the $\pi\pi$ or $K\pi$ rest systems. Thus, θ measures the angle between the the z axis and the outgoing π^- in reaction (1.1); the azimuth takes the values $\phi = 0$ (π^- along the x axis), $\varphi = 90°$ (π^- along the y axis), etc.

[17]F. T. Solmitz, Annu. Rev. Nucl. Sci. 14, 375 (1964).

[18]For reviews on deuterium corrections see P. Fleury, in *Methods in Subnuclear Physics*, edited by M. Mikolic (Gordon and Breach, New York, 1968), Vol. II, p. 541; B. Musgrave, in *Phenomenology in Particle Physics*, edited by C. B. Chiu, G. C. Fox, and A. J. G. Hey (Caltech, Pasadena, California, 1971), p. 467; A. Dar and A. Gal, Phys. Rev. Lett. 21, 444 (1968).

[19]J. E. Elias *et al.*, Phys. Rev. 177, 2075 (1969), and references quoted therein.

[20]For definitions of definite-naturality-exchange amplitudes, see J. P. Ader *et al.*, Nuovo Cimento 51A, 952 (1968). Unnatural-parity-exchange amplitudes have the general form $a\vec{\sigma}\cdot\vec{q} + b\vec{\sigma}\cdot\vec{q}\times\vec{n}$ where $\vec{q}$ is along the recoil-nucleon direction and $\vec{n}$ is along the production normal; they are spin flip with respect to the normal direction, although they conserve helicity in the scattering plane along an axis that depends on the coefficients a and b. Natural-parity-exchange amplitudes have the form $a + b\vec{\sigma}\cdot\vec{n}$, and flip the spin only with respect to directions in the production plane; if b vanishes, the natural parity amplitudes are spin nonflip.

[21]Radiative corrections can result in a loss of events, depending on $M_X{}^2$ cuts, due to energy loss caused by photon emission. These effects may be on the order of 5%. For estimates in similar reactions, see W. Wetzel *et al.*, Nucl. Phys. B115, 208 (1976).

[22]The scaled vector-meson production cross sections, integrated over mass, are related to dimensionless invariant helicity amplitudes by

$$p_{\rm lab}{}^2 d\sigma/dt = (0.389/128\pi M_N{}^2) \sum_{M,\,\lambda,\,\lambda'} |\langle M\lambda'|H|\lambda\rangle|^2,$$

where M, λ' denote the helicities of the vector meson, and the target and recoil nucleons respectively. The units are GeV for $p_{\rm lab}$ and M_N, and mb/GeV^2 for $d\sigma/dt$ (hence the factor 0.389).

[23]P. E. Schlein, Phys. Rev. Lett. 19, 1052 (1967).

[24]From unitarity considerations, the on-shell phase associated with $\pi\pi$ scattering is expected to be unchanged in going off-shell to larger $-t$. Naturally, the overall production-amplitude phases can vary with t. For a discussion, see G. Fox, in *Experimental Meson Spectroscopy—1972,* proceedings of the third International Conference, Philadelphia, edited by A. H. Rosenfeld and K.-W. Lai (AIP, New York, 1972), p. 271.

[25]S. Gasiorowicz, *Elementary Particle Physics* (Wiley, New York, 1966). We have used approximate expressions for the crossing factors, which are given exactly in Chap. 27 of this reference.

[26]For a discussion of the importance of s-channel helicity structure in absorptive effects, see F. Henyey *et al.*, Phys. Rev. 182, 1579 (1969).

[27]F. Arbab and J. D. Jackson, Phys. Rev. 176, 1796 (1968).

[28]P. K. Williams, Phys. Rev. D 1, 1312 (1970).

[29]G. C. Fox, in *Phenomenology in Particle Physics* (Ref. 18), p. 703.

[30]J. D. Kimel and E. Reya, Nucl. Phys. B47, 589 (1972).

[31]W. Ochs and F. Wagner, Phys. Lett. 44B, 271 (1973).

[32]G. L. Kane and A. Seidl, Rev. Mod. Phys. 48, 309 (1976).

[33]P. Estabrooks *et al.*, in π-π *Scattering—1973,* proceedings of the International Conference on π-π Scattering and Associated Topics, Tallahassee, edited by P. K. Williams and V. Hagopian (AIP, New York, 1973), p. 37.

[34]One solution to the 17-GeV/c $\pi\pi$ amplitude analysis of Estabrooks and Martin has relatively large phase differences between P_- and P_0; this is shown in P. Estabrooks and A. D. Martin, Phys. Lett. 41B, 350 (1972). The favored solution, which has a more slowly varying S-wave phase, has smaller phase differences between P_- and P_0. The two solutions are compared in P. Estabrooks and A. D. Martin, Ref. 33.

[35]H. Becker *et al.*, in *High Energy Physics with Polarized Beams and Targets*, proceedings of the Argonne Conference, 1976, edited by M. L. Marshak (AIP, New York, 1976), p. 243.

[36]C. D. Froggatt and D. Morgan, Phys. Lett. 40B, 655 (1972).

[37]A. C. Irving and C. Michael, Nucl. Phys. B82, 282 (1974).

[38]S. D. Protopopescu *et al.*, Phys. Rev. D 7, 1279 (1973).

[39]B. Hyams *et al.*, Nucl. Phys. B64, 134 (1973); W. Männer, in *Experimental Meson Spectroscopy—1974,* proceedings of the Fourth International Conference, Boston, edited by D. A. Garelick (AIP, New York, 1974), p. 22.

[40]$\delta_S{}^2$: W. Hoogland *et al.*, Nucl. Phys. B69, 266 (1974); $\delta_S{}^{3/2}$: see the discussion in H. Bingham *et al.*, *ibid.* B41, 1 (1972) and references therein.
[41]Particle Data Group, Rev. Mod. Phys. 48, S1 (1976).
[42]J. P. Baton *et al.*, Phys. Lett. 33B, 528 (1970).
[43]G. C. Fox and M. L. Griss, Nucl. Phys. B80, 403 (1974).
[44]M. J. Matison *et al.*, Phys. Rev. D 9, 1872 (1974).
[45]P. Hoyer, P. Estabrooks, and A. D. Martin, Phys. Rev. D 10, 80 (1974); P. Hoyer, R. G. Roberts, and D. P. Roy, Nucl. Phys. B56, 173 (1973).
[46]With the band $0.775 < m_{\pi\pi} < 0.795$ GeV excluded, residual ρ-ω interference effects in the ρ band ($0.70 < m_{\pi\pi} < 0.85$ GeV) are less than 4% in any of the cross sections $\sigma_{ij}(t)$ obtained for reactions (1.1) and (1.2). Since the data for reaction (1.2) have larger statistical and systematic uncertainties for $-t > 0.2$ GeV^2, we have relied on the data from reaction (1.1) to obtain the differential cross sections presented in this section. We have not corrected these data for the small residual ρ-ω interference effects outside of our ω cut.
[47]We have used $G_{\pi NN}{}^2/4\pi = 14.6$. For a recent review on the determination of the pion-nucleon coupling constant, see G. E. Hite, R. J. Jacob, and D. C. Moir, Phys. Rev. D 12, 2677 (1975).
[48]The mass bin used for the 13-GeV/c $K^-\pi^+$ data was $0.87 < m_{K\pi} < 0.92$ GeV; the mass bin for the 17-GeV/c $\pi^-\pi^+$ data was $0.71 < m_{\pi\pi} < 0.83$ GeV.
[49]R. D. Field and D. P. Sidhu, Phys. Rev. D 10, 89 (1974).
[50]Spin incoherence due to A_1 exchange can also affect the determination of $P_-^\perp$. However, the A_1-exchange contribution is orthogonal in nucleon-helicity structure to the π-exchange terms, even in the presence of s-channel nonflip π-exchange amplitudes associated with $t_{\min}$ effects. Thus A_1 exchange can only contribute quadratically to the observables, and $P_-^\perp$ is expected to reflect mainly the phase differences between P_- and P_0.
[51]The Kane-Seidl model predicts an energy dependence for each cut contribution to the $P_\pm$ forward amplitude of the form

$$P_\pm(t=0) \propto s^{\alpha(0)}/[3.33 + (\alpha'_P + \alpha')\ln 10s]^2,$$

where $\alpha'_P = 0.3$ GeV^{-2}, and $\alpha(0)$ and α' are the appropriate Regge-pole intercept and slope. According to the Field-Sidhu fit, the ratio of the A_2 cut to the π cut is 0.5 at 6 GeV/c, with a $\sim 30°$ relative phase. Using the Kane-Seidl parameters $\alpha_\pi(0) = -0.015$, $\alpha_A(0) = 0.3$, $\alpha'_\pi = 0.85$ GeV^{-2}, and $\alpha'_A = 0.8$ GeV^{-2} results in the effective energy dependence $\sigma_\pm(t=0) \propto s^{-0.26}$ from 6 to 17 GeV/c. Alternately, using a pion slope consistent with this experiment, $\alpha'_\pi = 0.3$ GeV^{-2}, gives $\sigma_\pm(t'=0) \propto s^{-0.18}$. These energy dependences imply a 30 to 50% increase in $\sigma_\pm(t'=0)$ going from 17 to 4 GeV/c. On the other hand, using $\alpha_A(0) = 0.5$ and the same ratio of A_2 to π exchange gives a nearly constant $\sigma_\pm(t'=0)$.
[52]For a review of ρ-ω interference effects, see G. Goldhaber, in *Experimental Meson Spectroscopy*, edited by C. Baltay and A. Rosenfeld (Columbia Univ. Press, New York, 1970), p. 59. For more recent photoproduction and e^+e^- annihilation data, see H. Alvensleben *et al.*, Nucl. Phys. B25, 333 (1971); H. Alvensleben *et al.*, Phys. Rev. Lett. 27, 888 (1971); D. Benaksas *et al.*, Phys. Lett. 39B, 289 (1972).
[53]A. Rabl and N. W. Reay, Phys. Lett. 47B, 29 (1973).
[54]A. S. Goldhaber, G. C. Fox, and C. Quigg, Phys. Lett. 30B, 249 (1969).
[55]S. Coleman and S. Glashow, Phys. Rev. Lett. 6, 423 (1961); Phys. Rev. 134, 671 (1964).
[56]A. C. Irving, Nucl. Phys. B105, 491 (1976).
[57]R. D. Field, in *Proceedings of the XVII International Conference on High Energy Physics, London, 1974,* edited by J. R. Smith (Rutherford Laboratory, Chilton, Didcot, England, 1974), p. I-185.
[58]A. V. Barnes *et al.*, Phys. Rev. Lett. 37, 76 (1976); O. I. Dahl *et al.*, *ibid.* 37, 80 (1976).
[59]G. C. Fox *et al.*, Ref. 7.
[60]P. Estabrooks and A. D. Martin, Nucl. Phys. B102, 537 (1976).
[61]J. D. Dowell *et al.*, Nucl. Phys. B108, 30 (1976); see also references therein on earlier ω-production data.
[62]O. I. Dahl *et al.*, Phys. Rev. Lett. 38, 54 (1977).
[63]For a discussion of the minimal t dependence of the unnatural-parity-exchange amplitudes in vector-meson production, see R. D. Field *et al.*, Phys. Rev. D 6, 1863 (1972).
[64]The coherence factors deduced by Irving (Ref. 56) for helicity-0 ρ-ω interference are inconsistent with the data presented in Table IX, even though they are based on preliminary results from this experiment [using a branching ratio $R(\omega \to \pi^+\pi^-) = 1.7\%$]. However, Irving's theoretical predictions for the coherence factors, which lie in the range 60 and 90% for $-t < 0.4$ GeV^2, are compatible with the present data provided the 1.7% branching ratio is used.
[65]With coupling constants defined by $g^2 = \Gamma m^2/q^{2l+1}$, SU(3) correctly relates the ρ and K^* couplings, as shown in the review article by N. P. Samios, M. Goldberg, and B. T. Meadows, Rev. Mod. Phys. 46, 49 (1974). However, the factors of q enter the π-exchange production amplitudes only in ratios, q/q_0, which reduce to unity at the pion pole. Consequently, even though the g's defined as above may satisfy SU(3), the production amplitudes due to π exchange need not obey SU(3).
[66]The factors N_ρ and N_{K^*} are not precisely known, since they are given by integrals of the ρ and K^* Breit-Wigner forms over all masses [Eq. (3.7)]. However, the quantities needed for testing SU(3) and WM are the ratios $P_0(\rho, K^*)/N_{\rho,K^*}$; uncertainties in the integrals over Breit-Wigner tails cancel in these ratios, since the σ_0 observables have been "corrected" for Breit-Wigner tails using the same parameters as were used to calculate N_ρ and N_{K^*}.
[67]Uncertainties in the effective trajectory $\alpha_+(\omega)$ have a small effect in extrapolating from 4 to 13 GeV/c. The cross section $\sigma_+(\bar{K}^*)$ changes by 5.4 mb at $-t = 0.1$ GeV^2 over this energy range. According to our model the contribution to $\sigma_+(\bar{K}^*)$ from the $P_+(\rho)$-$P_+(\omega)$ interference term increases from 1.0 mb at 4 GeV/c to 5.1 mb at 13 GeV/c, while with our choice of $\alpha_+(\omega)$ the contribution from $|P_+(\omega)|^2$ increases by 0.8 mb over this range. If we were to increase $\alpha_+(\omega)$ by as much 0.2, the $|P_+(\omega)|^2$ contribution would instead increase by 2.2 mb and the bulk of the 5.1 mb increase would still be attributed to $P_+(\rho)$-$P_+(\omega)$ interference.
[68]B. J. Hartley and G. L. Kane, Nucl. Phys. B57, 157 (1973).